2016

Feedback Control Theory in Stochastic Dynamical Systems

Ashkan Balouchi
Louisiana State University and Agricultural and Mechanical College, balouchi.ashkan@gmail.com

FEEDBACK CONTROL THEORY IN STOCHASTIC DYNAMICAL SYSTEMS

A Dissertation

Submitted to the Graduate Faculty of the
Louisiana State University and
Agricultural and Mechanical College
in partial fulfillment of the
requirements for the degree of
Doctor of Philosophy

in

The Department of Physics and Astronomy

by
Ashkan Balouchi
B.S., Sharif University of Technology, 2007
M.S., Sharif University of Technology, 2010
May 2016

To my family, for their endless love and support.
To my love, for all the wonderful moments we have together.

Acknowledgements

I would like to thank my advisor, Dr. Dana Browne, for his excellent ideas, great support and unlimited encouragement. He is truly a wonderful teacher, not just in physics, but also in every other aspect. Thanks for always being so understanding during my graduate school days.

I would also like to thank my co-advisor, Dr. Jonathan Dowling, for his support in every step of my graduate study. He is an inspiration in my life. Thanks for all the energy you spread out.

I would especially like to thank my collaborator, Dr. Kurt Jacobs, for his brilliant ideas, encouragement, and time for all the Skype meetings and helpful discussions. Second part of this work was also performed with the use of the supercomputing facilities managed by the Research Computing Department at the University of Massachusetts Boston, under Dr. Jacobs supervision.

I would also like to thank my committee member, Dr. Georgios Veronis, for his time and support. I am also thankful to Dr. Martin Tzanov for being on my general exam committee.

I am so grateful that I have had so many great teachers and advisors in my life. I would especially like to thank my M.S. advisor, Dr. Shahin Rouhani, for introducing me to the world of statistical physics and providing me with research opportunities and for his unlimited encouragement.

I am grateful to my high school physics teacher, Dr. Nader Noori, for opening the door of the world of physics to me. Thank you for all the help and encouragement you provided during my high school years.

There are too many friends who had great influences in my life to name them all individually, but I would like to thank Arash Vesaghi for always being there; Navid Dianati for all the great moments we had together; Navid Khosravi for always being a true friend; Mohammad Soltanieh-ha who has always been my physics fellow and a close friend, Houman Bedayat, Nima Chitsazan, and Misagh Naderi for being supportive and irreplaceable during

my years at LSU and my many classmates both at Sharif and LSU.

I would like to give special acknowledgements to my parents, Reza Balouchi and Fariba Mirza Aghasi, who always encouraged me to learn science and provided me the best educational opportunities. I would also like to thank my brother, Andisheh Balouchi, who always encouraged me to achieve my goals. My family's support and encouragement indeed made it possible to travel this road.

There is one person in my life that non of these would have been possible without her. She has been always the best support I could have. She has made my life full of joyful moments and memories. She has been patient with all the difficulties we faced including two plus one years of long distance relationship. I can not express my appreciation to her by any words rather than saying I love you Azadeh Keivani.

Table of Contents

List of Tables

List of Figures

Abstract

A stochastic dynamical system is a system composed of many interacting components which includes stochastic behavior. Feedback control theory is designed to use information from the current state of the system in order to temper the final state toward the desired outcome. In this dissertation, I perform studies on two choices of classic and quantum dynamical systems to cover vast variety of statistical tools and methods. For classical model, I perform a study on finite-size effects at the phase transition in the Nagel-Schreckenberg traffic model as an example of non-equilibrium many body stochastic dynamical system. For quantum mechanical model, I introduce an optimal measurement-based feedback control protocol for cooling a single qubit as an example of complex system with one cell and many degrees of freedom.

I examine the Nagel-Schreckenberg traffic model for a variety of maximum speeds. I show that the low density limit can be described as a dilute gas of vehicles with a repulsive core. At the transition to jamming, I observe finite-size effects in a variety of quantities describing the flow and the density correlations, but only if the maximum speed $V_{\max}$ is larger than a certain value. A finite-size scaling analysis of several order parameters shows universal behavior, with scaling exponents that depend on $V_{\max}$ The jamming transition at large $V_{\max}$ can be viewed as the nucleation of jams in a background of freely flowing vehicles.

Feedback control of quantum systems via continuous measurements involves complex nonlinear dynamics. As a result, even for a single qubit the optimal measurement for feedback control is known only in very special cases. I show here that for a broad class of noise processes, a series of compelling arguments can be applied to greatly simplify the problem of steady-state preparation of the ground-state, while loosing little in the way of optimality. Using numerical optimization to solve this simplified control problem, I obtain for the first time a non-trivial feedback protocol valid for all feedback strengths in the regime of good control. The protocol can be described relatively simply, and contains a discontinuity as a function of feedback strength.

1. Introduction

Nature is a complex dynamical system. Of the 17th century, as a physicist, we know that there are very few problems that allow exact solutions in the fields like classical mechanics. Even in ideal classical world, a huge amount of problems cannot be solved by the complexity of the problem itself or by the enormous number of degrees of freedom. Beyond that, the most precise physical laws are quantum mechanical with its underlying principle of uncertainty. We cannot predict the future state of even the simplest imaginable system without giving a probability distribution. Since nature does not act deterministically, science needed to build up and develop probabilistic methods to describe the world. Statistical mechanics have been a successful approach to describe the rules of thermodynamics and to predict the future state of a system. Counting on the huge number of particles playing role in the system is the fact that statistical mechanics lays on. Stochastic analysis approach had been built up to explain what could happen to the system, even a single particle, which undergoes through evolution by a random variable [1, 2].

Robert Brown in 1827 discovered that the grains of pollen have a random motion in water, that exists even without any flow in the water. In 1905, Einstein characterized so-called Brownian motion with physical quantities and it became a critical test for atomic/molecular nature of matter. Later in 1908, Paul Langevin was the first to apply Newton's second law to a Brownian particle, on which the total force included a random component. Since then the Brownian motion (also called as Wiener process) has been considered as a random motion with Gaussian distribution with zero mean and variance proportional to time. In 1940's, Ito and Chandrasekhar independently built up a strong mathematical basis for stochastic analysis (named Ito calculus) and solved a number of important dynamical problems in terms of probabilistically defined random variables [3].

Nowadays stochastic and statistical methods are applied to various fields in physics from a small quantum resonator to a living world system like traffic flow or up to the huge physical

systems in galaxies. It finds heavy use in biology, chemistry, social evolution studies, coding theory, economy and financial markets.

The main purpose in studying these dynamical systems is to figure out the macroscopic behavior of the system from the microscopic properties. Prediction of the future behavior of the system as well as ability to describe the current state of the system is mostly the reason of all the complex system analysis. Correlation functions are the most important tools to analyze the dynamical systems.

Correlation functions are measuring the order in the system. They show if different parts of the system behave with respect to each other's state or independently. In other words, correlation functions show how microscopic variables such as local density at different positions are related. Using correlations, one can quantify how these variables co-vary with each other in average across the system.

The correlation length shows the typical size of the correlated regions. Long range correlations indicate that parts far away from each other change respectively while short range correlations show that only nearby parts can affect each other's behavior. Correlation functions can be defined in space or time. Spatial correlations show the size of the correlated regions in space, while time correlations indicate how much the system cares about its history or how much the current state of the system can affect its future state.

In many cases, one wants to control a system that has been undergoing a stochastic evolution, rather than just measuring and predicting the final state. Feedback control theory deals with the behavior of dynamical systems in order to obtain a desired effect on the output of the system. It uses one or more output variables of the system as a controller. Based on the controller state, it changes either the input or the evolution process so that the output state gets closer to the desired one. The feedback control theory is strongly tied to the correlation functions of the system. If there is a growing correlation length in the system, that means global information is needed to feed the control protocol. On the other hand if there only exists short range correlations in the system, local information could be sufficient

for the controlling process. To apply any control process on a given dynamical system, one should be able to characterize the main underlying features of the system. Analyzing stochastic dynamical systems is an interesting area of research with applications in a wide range of different problems from classical to quantum mechanics.

In this dissertation, I have studied two kinds of dynamical systems; classical and quantum mechanical. First I present an extensive study on main features of the traffic flow problem as a classic stochastic dynamical system. I characterize the properties of jamming transition in traffic flow. I have developed certain necessary tools to be used in any traffic control process. Second I provide an example of finding feedback control protocol for cooling a nano-mechanical resonator.

A very good example of a classical dynamical system that needs to be studied is the traffic flow problem. The rapid growth of the number of vehicles on the limited capacity of the city streets and the highways has made the existence of long traffic jams a natural daily observation. Environmental damages by vehicle emissions as well as the huge cost of the energy and time wasted in traffic jams are getting out of control. These make the research of finding ways to control the traffic dynamics a necessity. In addition, the traffic dynamic problem as a social behavioral phenomenon, could be a good example of complex social dynamics and the methods used to describe that can be applied to many other social human behavioral dynamics [4].

The phase transition from the free flow region to the jammed region should be studied extensively in order to characterize the necessary tools for controlling the traffic. Being able to describe each phase in detail and explaining the main features of the transition are keys to understand the traffic flow problem. Analyzing the correlation functions at the transition with respect to the system parameters such as the speed limit, road length, random behavior of the drivers, etc. can provide required information in order to understand the underlying features of the traffic flow.

Not only in classical but also in quantum systems, the experimental technology, particularly in the fields of cavity QED, ion trapping, and Bose-Einstein condensation, has now developed to the point where individual quantum systems can be monitored continuously with very low noise and may be manipulated rapidly on the time-scales of the system evolution. It is therefore natural to consider the possibility of controlling individual quantum systems in real time using feedback [5], which is called quantum feedback control theory.

Preparing quantum systems in pure states is so important in potential quantum technologies like quantum computer. This task is strongly linked to cooling to a non-degenerate ground state because in both cases entropy is needed to be extracted from the system. As a result cooling nano-mechanical resonators, both theoretically and experimentally, needs to be studied more. Finding the maximum achievable ground state population for a given maximum force is important. It is not usually possible to prove the optimality of control protocols for complex dynamical systems due to complexity of the cooling problem [6].

In this dissertation, I have taken two distinct approaches to study dynamical systems: classical and quantum; each with illustrating applicable cases. In Chapter 2, I describe the first approach. I discuss the traffic flow problem as an example of classical complex dynamical systems by presenting the fundamental features of each traffic phase as well as substantial study on the correlation functions in the traffic flow problem. The conclusion of this part is discussed at the end of the chapter. In Chapter 3, I explain the second approach, by introducing the cooling process for a single qubit as an example of quantum dynamical systems and representing a near-optimal measurement-based feedback control for a single qubit. The chapter concludes with a discussion about the obtained results. Conclusions are presented in Chapter 4.

2. Finite-Size Effects in the Nagel-Schreckenberg Traffic Model

2.1 Introduction

The flow of traffic represents a many-particle non-equilibrium problem with important practical consequences. Traffic flow shows well defined collective behavior where the free flow of traffic at low density changes abruptly with growing density to a denser phase with jams. The jams themselves show organized motions with start-stop waves as the cars creep forward. In addition to free flow and jam phases, there are also instances of synchronized flow at low velocity. Understanding the collective dynamical behavior and controlling the jams will give insight into effective traffic management.

The interesting dynamics of vehicular traffic has gained both engineers and physicists attention for decades. While traffic engineering has been very successful in predicting or even controlling the traffic in a given situation based on empirical data, physicists approach is usually quiet different. Physicist are mostly interested in modeling traffic in order to describe the general features of typical traffic [7]. Developing models not only can provide an understanding towards the complexity of the traffic phenomena, but also may help to extract the fundamental aspects of traffic and use them to predict and control the real traffic state.

Traffic behavior has been modeled using a variety of approaches. As many other phenomena in nature, traffic study approaches can be categorized in two major conceptual frameworks; macroscopic and microscopic. In macroscopic view the traffic is represented by compressible fluid where the fluid density is a representation of vehicles density in the road. Therefore the traffic flow should be studied by certain tools such as fluid dynamics models [8] or Boltzmann equation [9] approaches. As it is clear by the macroscopic name, in this approach the focus is on the features of the whole system and individual vehicular behavior is not the subject of interest.

In contrast, the microscopic models focus on the individual vehicles as particles who cause the macroscopic behavior of the system. The microscopic framework itself contains several

varieties of views. Modified versions of kinetic theory of gases allow probabilistic description on vehicular traffic based on Kinetic theory. Deterministic description of vehicular traffic based on principles of classical Newtonian dynamics forms another class of models called car-flowing models. The major disadvantage of described models is ignoring the humans' behavior as drivers of the vehicles which can cause stochastic dynamic for each individual vehicle. So-called particle hopping models describe the dynamics of the traffic flow based on stochastic behavior of each individual vehicle in the system. In these models each vehicle is seen as a cell. Each cell follows certain rules for its motion which can include a level of stochasticity. This approach is also known as cellular automaton (CA) [7, 4, 10]. CA approaches have become a popular and efficient tool to explore the nature of traffic flow. In CA models, vehicles occupy discrete sites and have discrete velocities, hopping from site to site according to simple rules. Despite their simplicity, these models appear to capture much of the collective behavior observed in real traffic. In this document our focus is on the most well known CA model for traffic model called Nagel-Schreckenberg

In 1992, Nagel and Schreckenberg (NS) [11] introduced a relatively simple CA model for traffic flow. The road is represented as a set of L equally spaced sites, each of can be occupied by at most one of N vehicles. Vehicles have discrete velocities v_n from 0 to a maximum velocity $V_{\max}$. The hopping dynamics follow four simple rules, applied in the following sequence.

Accelerating: First, each car with $v_n < V_{\max}$ increases its velocity by one.

Adjusting Velocity: The gap to the next car$g_n = r_{n+1} - r_n - 1$ is then computed. If the car has a speed greater than g_n, it will brake to reduce its speed to g_n to prevent a collision (gap rule).

Stochastic Decelerating: Variations in driver behavior are modeled by then lowering the speed $v_n \to v_n - 1$ with a fixed probability p.

Position Update: Finally, the position of each car is updated via $r_n \to r_n + v_n$.

The NS model successfully mimics many of the known features of the traffic flow, so it

has been widely studied during the past twenty years. Nagel and Schreckenberg [11] showed that at low density $d = N/L$, a free flow state occurred where the cars all have a speed of $V_{\max}$ or $V_{\max} - 1$, with a mean speed of $V_{\max} - p$. At a certain density, the steady state changes to a phase with a nonzero fraction of the cars participate in a jam of slowly moving or stopped vehicles. The nature of this transition from the free flowing phase to the jam phase has been the central question in many of the traffic research since this model has been introduced.

Nagel and Paczuski [12] showed in a variant of the NS model, where cars with $V = V_{\max}$ maintain their velocity as a kind of cruise control, that the jam lifetime showed a power law distribution at the transition to the jam phase. Lubeck et al. [13] studied the density distribution in the NS model and suggested that the free flow and jam phases coexist after the transition. Chowdhury et al. [14, 15] examined the gap distribution and time-headway distribution (the time delay between two consecutive cars passing a site) and also concluded that there is a two-phase coexistence after the transition. Roters et al. [16] investigated the dynamical structure factor and concluded that a continuous phase transition occurs, but later work [17, 18] suggested that the simulations were not long enough and that the critical behavior was actually a crossover phenomenon. Kerner et al. [19] observed evidence of two first order phase transitions, with an intermediate phase of synchronized flow between the free flow phase and the jam phase.

Many quantities have been used to study the transition to the jam phase. A number of them use the velocity distribution, such as the number of stopped cars ($V = 0$) [20], slowly moving cars ($V \leq V_{\max}/2$) [21] or cars not moving at the speed limit ($V < V_{\max}$) [12]. Other authors have chosen the number of vehicles forced to brake [22] or the difference between the average velocity and the free flow velocity [23]. All of these resemble order parameters, being nearly to zero in the free flow phase and nonzero in the jam phase. Other quantities have been studied that not necessarily zero in the free phase, but show an abrupt change at the transition, such as the vehicle flux [11] or the change in the vehicle's kinetic energy

per step [24, 25]. A number of different traffic correlations have also been studied, including different characteristic velocities in the spatial dynamical structure factor [13], different maxima in the velocity-position correlation [16], the gap or time-headway distribution [15], the number of cars moving cooperatively [26] and velocity correlations among the cars [27].

Despite this effort, a comprehensive picture of this transition is still incomplete, with different approaches producing differing conclusions about the nature of the transition or the presence of long range order. In this paper, we will examine how the value of $V_{\max}$ affects the transition. We will show that, while the static structure factor shows long range behavior appearing at the transition for any $V_{\max}$, we only see finite-size effects in the order parameter for $V_{\max} \gtrsim 6$. This indicates that the nature of the long range behavior is different at high and low values of $V_{\max}$. We use these finite-size effects to extract the scaling behavior at the transition for several order parameters. Our work indicates that the onset of the jam phase can be analyzed as a two-phase coexistence of free flow and localized jams, as others have observed [13, 15, 16]. We show that the dependence on $V_{\max}$ can be attributed to a qualitative change in the way jams nucleate at high and low $V_{\max}$.

In section II of this part, we review the details of our simulation and the quantities we use in our analysis. In Section III the focus is on the properties of the free flow phase. We show that the low density traffic as free flow phase shows similar behavior as a repulsive-core gas. We also present a quantitative analytic model of the behavior of the free flow phase based on the Bayesian probability theory and distribution of the vehicles' velocity. Section IV contains our analysis of the phase transition. I will be shown that long range correlations exist at the transition and if the value of $V_{\max}$ exceeds a certain limit, finite-size effects would appear in system behavior. Section V discusses how the value of $V_{\max}$ affects the fluctuations of jammed regions and how that affects the finite-size effects we see. Our conclusions are summarized in Section VI.

2.2 Methodology

2.2.1 Simulation

We have performed a set of Monte Carlo simulations in order to examine the main features of the phase transition in the Nagel-Schreckenberg traffic flow model. We have used a wide range of values for the model parameters such as maximum speed $V_{\max}$, density d and slow down probability p. We have also varied the length of the track L in order to find out whether it is a size sensitive transition or not. All the traffic flow simulations in this dissertation are done for a single lane track with periodic boundary conditions. The track lengths varied from 5,000 to 100,000 sites. We initially distributed the cars uniformly around the track. The system was then evolved for at least 10^6 time steps to form a random steady state, a time step being one update of all N vehicle positions and velocities. We then sampled the system every ten time steps for the next 10^7 to 10^8 time steps, the exact length depending on the system size.

Since this is a non-equilibrium problem, we were careful to look for non-ergodic effects and sensitivity to initial conditions. We used different random seeds to generate 5-10 different steady states for each choice of density and track length. We also did simulations using two different random number generators. We have seen no evidence that the choice of initial condition or random generator affected our results, although we have seen the need for long simulation times (much longer than typically used) to ensure that we are seeing the steady state behavior.

It is common in some non-equilibrium problems that if one takes the ending configuration of a system at a higher density, and uses its ending configuration (minus a few cells) as a starting configuration at lower density, the results may be different than a fresh simulation at lower density. This effect is called hysteresis. I have checked such a situation in this problem (used the ending configuration at higher density minus a few cars as a starting configuration at lower density) and saw the same results as starting from an initially uniform distribution

of cars for the lower density. This shows that the effects I report in this dissertation could not be the artifact of hysteresis in the model. The values I show in this dissertation represent averages over simulation time, initial condition and random number generator.

2.2.2 Fundamental Diagrams

The main goal of most of the traffic control protocols is to maximize the average flux of the vehicles on the road. The flux of the vehicles can easily be computed by:

$$\text{flux} = \langle v \rangle d, \tag{2.1}$$

where d represents the density of vehicles on the road and $\langle v \rangle$ denotes the average velocity of the cars. At low densities, vehicles form an independent free flow phase with $\langle v \rangle \approx v_{max} - p$. As the density of the vehicles d or the slow down probability p raises, the average velocity decreases, and system undergoes a transition from the free flow phase to the jammed phase. Through this transition the system goes from the homogeneous regime to an inhomogeneous regime, characterized by low local density and high local density (jams), respectively. The so-called fundamental diagram for velocity shows how the average velocity changes with respect to density d and slow down probability p (Figure2.1).

For a given value of slow down probability p, the average velocity $\langle v \rangle$ decreases as the density d grows. Therefore there exists a density which maximizes the $flux$ of the vehicles. The fundamental diagram for flux of the vehicles shows how the average flux changes with respect to density d and slow down probability p (Figure2.2).

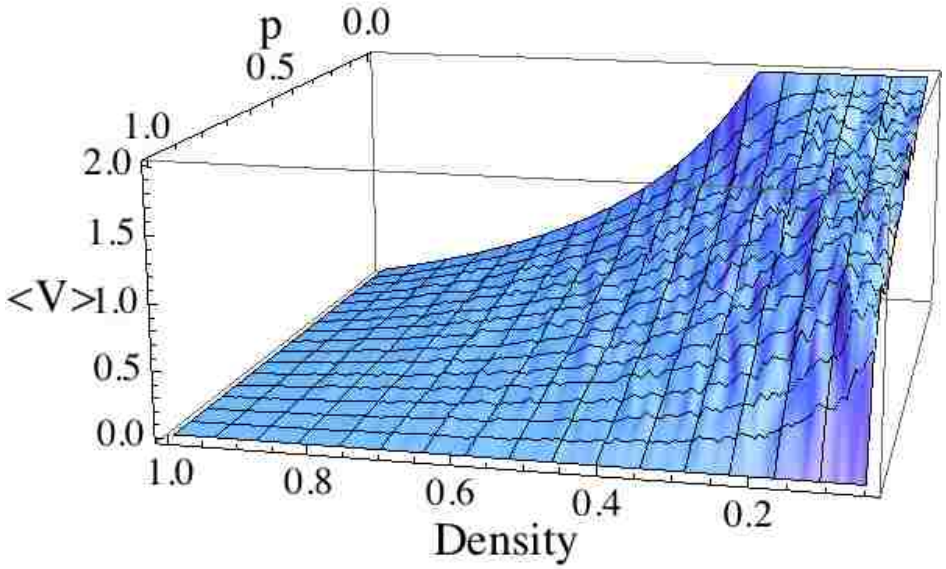

(a)

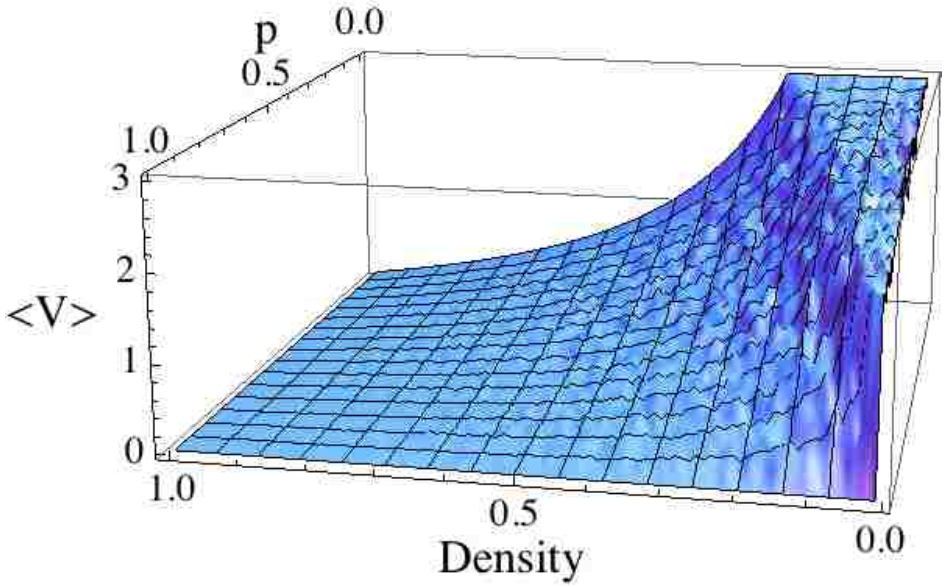

(b)

Figure 2.1: The Fundamental diagram for velocity. Plots show how the average velocity changes with respect to density d and slow down probability p for (a) $v_{max} = 2$ and (b) $v_{max} = 3$. Two distinct phases are clearly observable in terms of how the value of $\langle v \rangle$ changes.

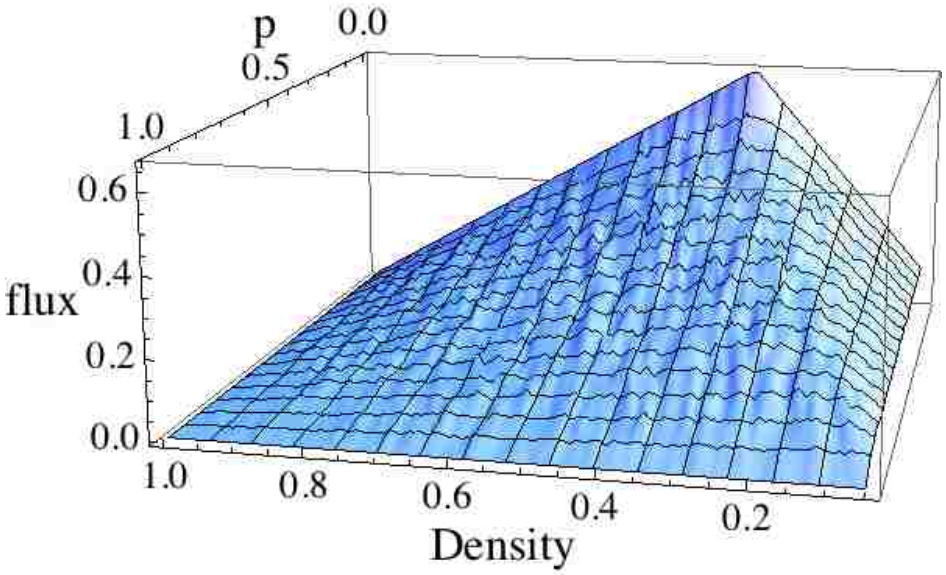

(a)

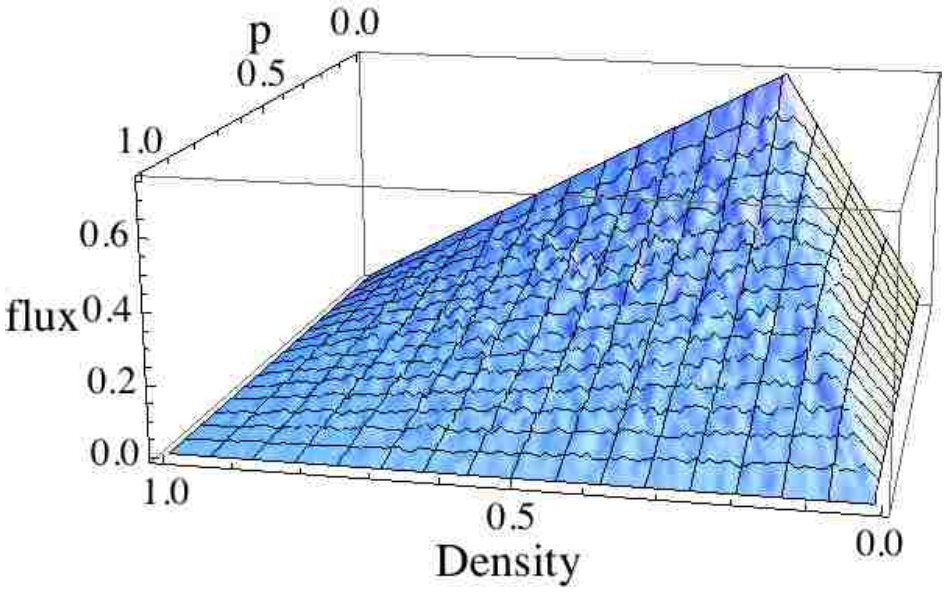

(b)

Figure 2.2: The Fundamental diagram for flux. Plots show how the average flux changes with respect to the density d and slow down probability p for (a) $V_{\max} = 2$ and (b) $V_{\max} = 3$. For each given value of slow down probability p, there is a density which maximizes the value of flux $= \langle v \rangle d$.

2.2.3 Tools

To analyze this model, we chose to study density correlations. To define the local density we use $n(r)$, where $n(r) = 1$ if there is a car at site r and zero otherwise. The static structure factor $S(q)$ is defined as:

$$S(q) = \langle |\rho(q)|^2 \rangle, \tag{2.2}$$

where $\rho(q)$ is the Fourier transform of the density function $n(r)$:

$$\rho(q) = \sum_{r=1}^{L} e^{-iqr} n(r). \tag{2.3}$$

$S(q)$ shows the frequency (respectively the wave length) of the correlated regions. The value of $S(q)$ at low frequencies (respectively long wave lengths) indicates how strong the long range correlations in the system are. Figure2.3 shows the typical behavior of the static structure factor for choices of low and high density.

Another useful correlation function is the pair correlation $G(r)$:

$$G(r) = \frac{1}{L} \sum_{q} e^{iqr} \left(\frac{S(q)}{N} - 1 \right) = \left\langle \frac{1}{N} \sum_{l=1}^{L} n(l) n(l+r) \right\rangle, \tag{2.4}$$

where the angle brackets denote an average over configurations. $G(r)$ is also known as the density-density correlation. The value of the pair correlation $G(r)$ is simply the probability of finding two vehicles on the road with distance r. Figure2.4 shows the typical behavior of the pair correlation function for choices of low and high density.

The other function we examine is the nearest neighbor distribution $P(r)$:

$$P(r) = \left\langle \frac{1}{N} \sum_{n=0}^{N-1} \delta(r_{n+1} - r_n, r) \right\rangle, \tag{2.5}$$

where r_n denotes the position of the n-th car and $\delta(,)$ denotes a Kronecker delta. $P(r)$

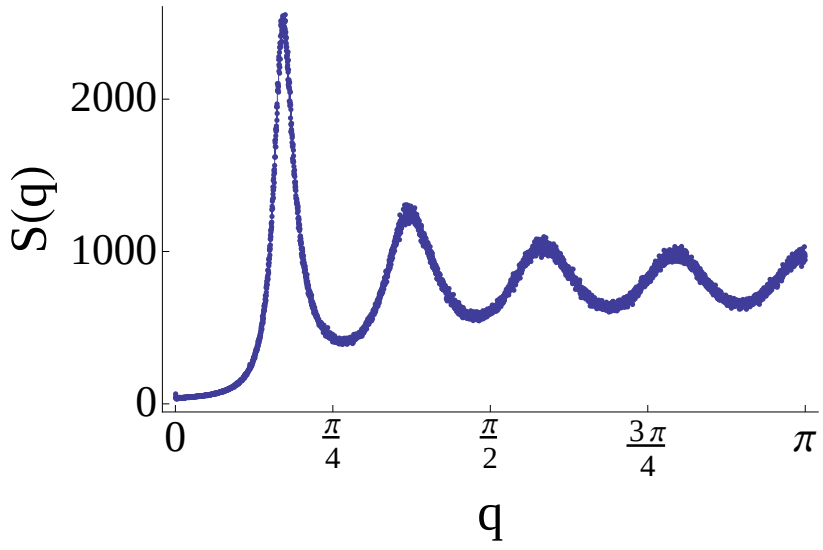

(a)

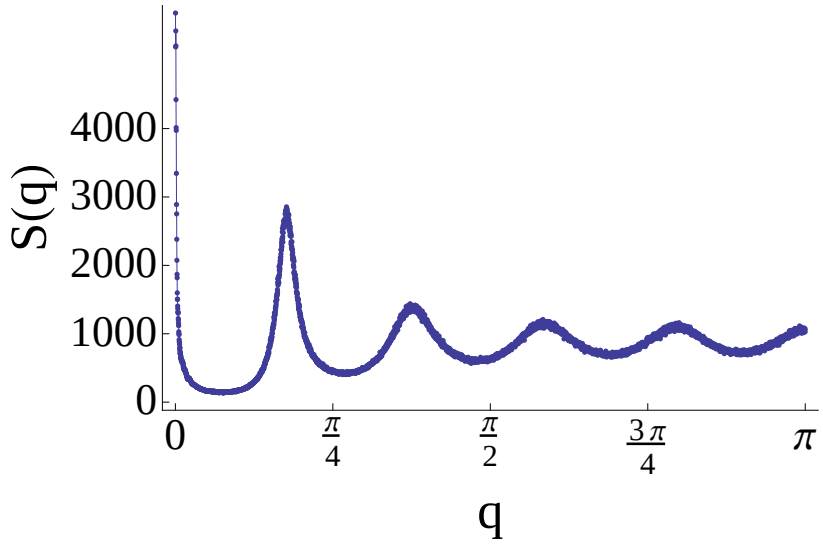

(b)

Figure 2.3: The static structure factor for values of $V_{\max} = 9$, $p = 0.1$ and choices of (a) low density $d = 0.08$ and (b) high density $d = 0.09$. There are $V_{\max}$ ordinary peaks in 2π range of the $S(q)$ plot. There could be an extra peak at a very low frequency in case of long range correlation existence.

is simply the probability that the distance to the next car ahead is equal to r. That is equivalent to finding a gap equal to $r - 1$ between the cars. Figure2.5 shows the nearest neighbor distribution for the same parameters in Figs 2.3 and 2.4.

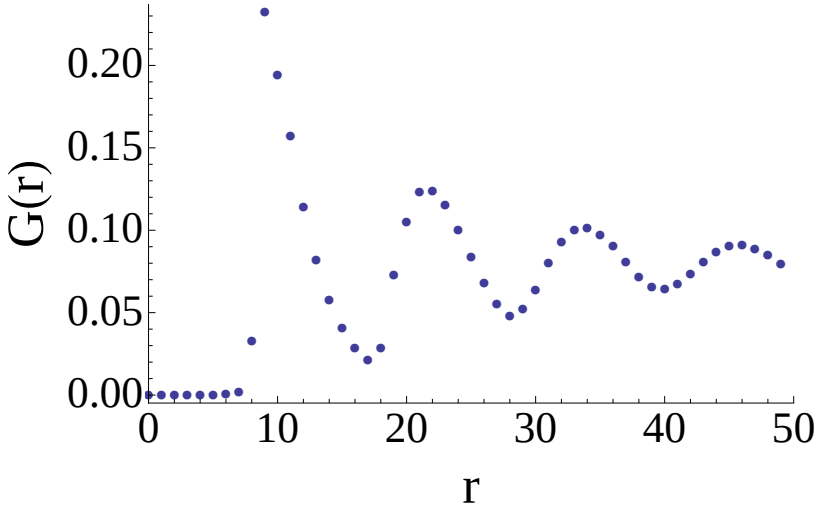

(a)

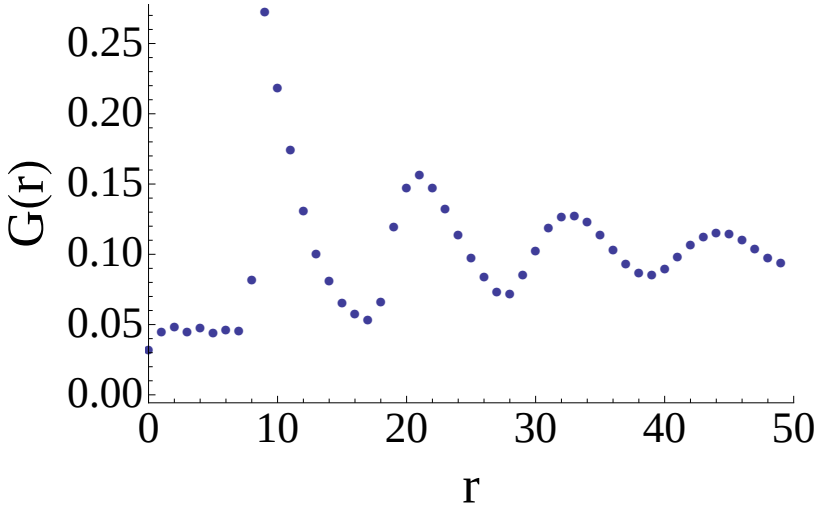

(b)

Figure 2.4: The pair correlation factor of $V_{\max} = 9$, $p = 0.1$ and choices of (a) low density $d = 0.08$ and (b) high density $d = 0.09$. The first peak is at $r = V_{\max}$. Other peaks are the resonance influence of the first peak.

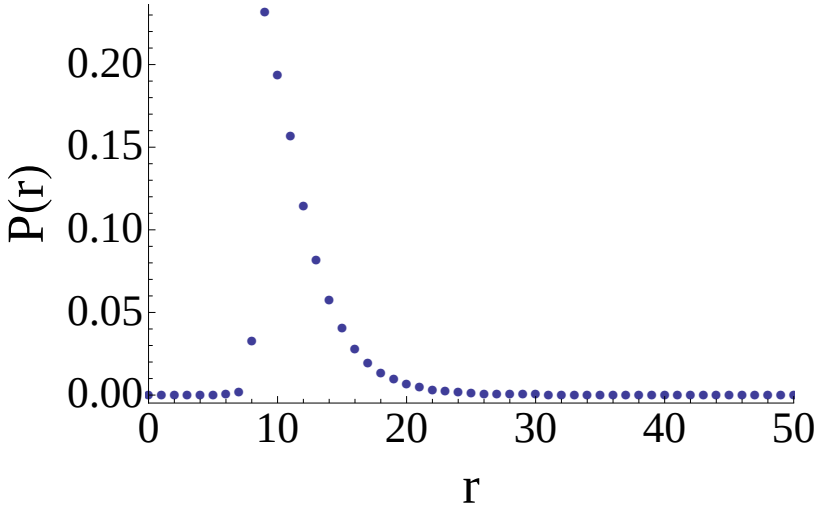

(a)

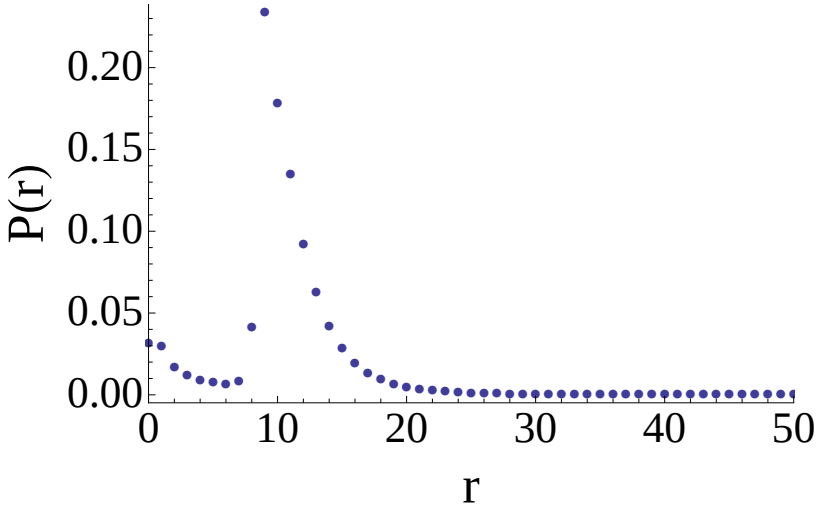

(b)

Figure 2.5: The nearest neighbor correlation of $V_{\max} = 9$, $p = 0.1$ and choices of (a) low density $d = 0.08$ and (b) high density $d = 0.09$. The probability of two consecutive cars at distance r from each other goes to zero when $r >> V_{\max}$.

2.3 Free Flow Regime

In this model, the only interaction between the vehicles is the gap rule, which comes into play only when the distance to the next car is less than or equal to $V_{\max}$. At low density $d = N/L$, when the vehicle spacing is typically much larger than $V_{\max}$, naively applying the other dynamical rules produces a steady state with each vehicle having a speed of $V_{\max}$ or $V_{\max} - 1$ with a mean speed of $V_{\max} - p$. If the vehicles have this speed distribution, the vehicle spacing evolves as a random walk with a diffusion constant of $p(1-p)$. However, this produces a steady state where all spacings between cars are equally likely, including spacings of less than $V_{\max}$.

Therefore, even in the dilute regime, the gap rule followed by the random slowdown, forces some cars to spend a small fraction of the time at a speed of $V_{\max} - 2$ because the gap to the vehicle ahead of it is $V_{\max} - 1$. This vehicle will, on the next time step, have a gap of $V_{\max} - 1$ or larger. Thus each car has a "repulsive core" that strongly favors at least $V_{\max} - 2$ empty sites ahead of it. In Figure 2.6 we show a typical example.

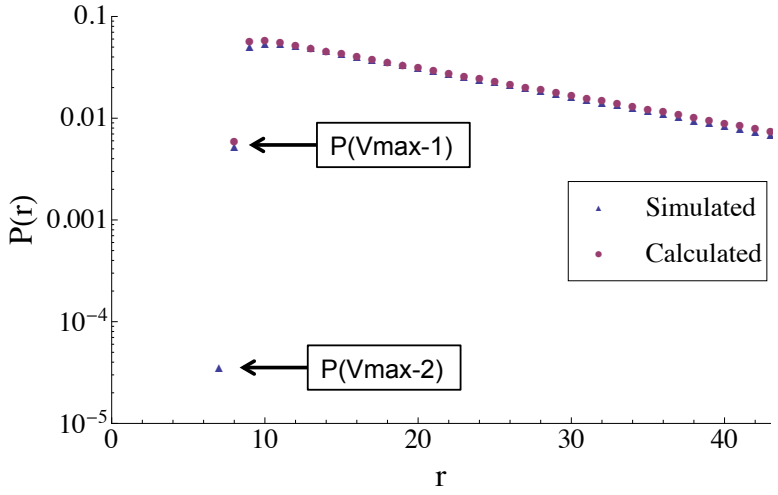

Figure 2.6: Semilog plot of simulated $P(r)$ and that calculated from the kinetic model for $V_{\max} = 9$ and $p = 0.1$ at a density $d = 0.04$, about half the critical density for the jams to form.

2.3.1 Kinetic Model for Dilute Traffic

In the dilute limit, the interaction between cars produced by the gap rule only applies to a pair of vehicles at a time, and simultaneous interactions among a triple of adjacent vehicles are rare. We define a distribution function $f(v, g)$ as the probability that a car has a velocity v and the gap to the vehicle ahead is g.

From this distribution we can calculate the velocity distribution $P_v(v)$ as

$$P_v(v) = \sum_{g=0}^{L-1} f(v, g)\,. \tag{2.6}$$

We can also calculate the distribution of gaps $\Delta(g)$ via

$$\Delta(g) = \sum_{v=0}^{V_{\max}} f(v, g)\,, \tag{2.7}$$

from which we can find the nearest neighbor distribution $P(r)$ from the relation $P(r) = \Delta(r-1)$.

Each of the 4 rules of the NS model alters the form of $f(v, g)$. We find it simplest to examine $f(v, g)$ right after the velocity updates and before the position update. This is tantamount to assigning the position update as the first step instead of the last.

The position update rule produces an altered distribution $\hat{f}(v, g)$ via

$$\hat{f}(v, g) = \sum_{u=0}^{m} P_v(u) f(v, g + v - u)_t\,, \tag{2.8}$$

where for convenience we have denoted $V_{\max}$ as m, since it will appear frequently in this section. Since we are ignoring triple correlations, the speed distribution of the vehicle ahead is $P_v(v)$ from Eq. (2.6). The velocity update rules then alter the $\hat{f}(v, g)$ distribution. For

gaps greater than or equal to $V_{\max}$ the rules yield

$$\begin{aligned} f(m,g) &= (1-p)\left[\hat{f}(m,g)+\hat{f}(m-1,g)\right] \\ f(m-1,g) &= p\left[\hat{f}(m,g)+\hat{f}(m-1,g)\right]+ \\ &\quad +(1-p)\hat{f}(m-2,g) \\ f(v,g) &= p\hat{f}(v,g)+(1-p)\hat{f}(v-1,g) \\ &\qquad\qquad v=1\ldots m-2 \\ f(0,g) &= p\hat{f}(0,g)\,, \end{aligned} \tag{2.9}$$

while for gaps smaller than $V_{\max}$ we have

$$\begin{aligned} f(v,g)_{t+1} &= 0 \qquad v=g+1\ldots m \\ f(g,g)_{t+1} &= (1-p)\left[\sum_{u=g-1}^{m}\hat{f}(u,g)\right] \\ f(g-1,g)_{t+1} &= p\left[\sum_{u=g-1}^{m}\hat{f}(u,g)\right]+(1-p)\hat{f}(g-2,g) \\ f(v,g)_{t+1} &= p\hat{f}(v,g)+(1-p)\hat{f}(v-1,g) \\ &\qquad\qquad v=1\ldots g-2 \\ f(0,g)_{t+1} &= p\hat{f}(0,g)\,. \end{aligned} \tag{2.10}$$

Our simulations show that the three velocity update steps for dilute traffic rapidly create a local equilibrium in the velocity distribution where the vehicle is moving at the highest speed it can with probability $1-p$, or at the next to highest speed with probability p. For

$g \geq m$, the highest speed is $V_{\max}$ and so the distribution is

$$f(v,g) = \begin{cases} (1-p)\Delta(g) & v = m \\ p\Delta(g) & v = m-1 \\ 0 & v = 0 \ldots m-2\,, \end{cases} \tag{2.11}$$

while for gaps less than $V_{\max}$ we have

$$f(v,g) = \begin{cases} 0 & v = g+1 \ldots m \\ (1-p)\Delta(g) & v = g \\ p\Delta(g) & v = g-1 \\ 0 & v = 0 \ldots g-2\,. \end{cases} \tag{2.12}$$

Deviations from this distribution relax exponentially as p^n after n steps.

The leading order correction that arises from the gap rule occurs when a faster vehicle catches up to a slower vehicle so that the gap between them is $V_{\max} - 1$. The gap rule then limits the speed of the car behind to $V_{\max} - 1$, causing it to spend a fraction of its time at a speed of $V_{\max} - 2$. The fraction of vehicles that do that is $P_v(V_{\max} - 2) = p\Delta(V_{\max} - 1)$.

The speed distribution from Eq. (2.6) is then

$$\begin{aligned} P_v(m-2) &= \alpha p \\ P_v(m-1) &= (1-\alpha)p + \alpha(1-p) \\ P_v(m) &= (1-\alpha)(1-p)\,, \end{aligned} \tag{2.13}$$

where $\alpha = \Delta(m-1)$ is the fraction of cars with a gap of $V_{\max} - 1$.

Putting this speed distribution into Eq. (2.8) with the assumed distribution for $f(v,g)$ given by Eqs. (2.11) and (2.12), we can produce an evolution equation for the gap distribution

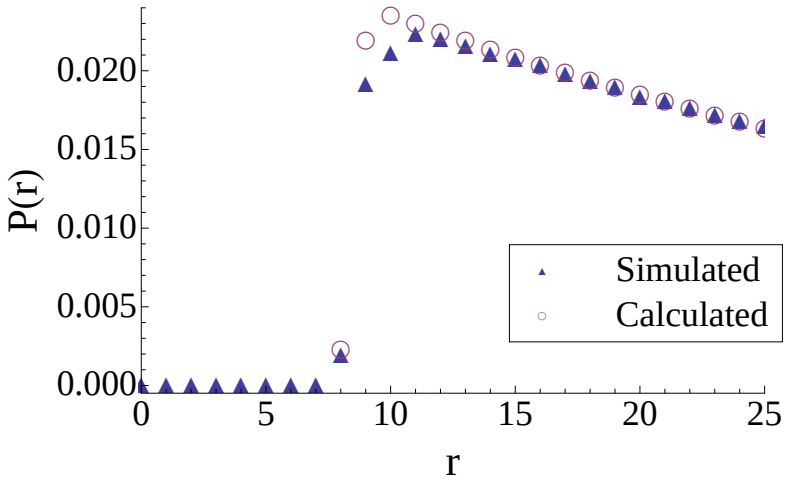

(a)

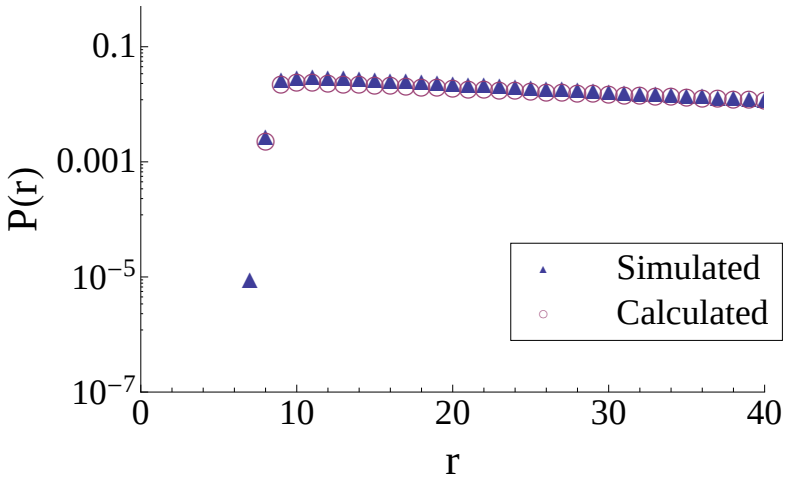

(b)

Figure 2.7: Nearest neighbor correlation from the simulations and Eq. (2.17) for $V = 9$ and $p = 0.1$ at a density of 0.02 on (a) a regular scale and (b) a semilog scale.

of the form

$$\Delta(g)_{t+1} = \sum_{g'} \Gamma(g' \to g)\Delta(g')_t \,.$$

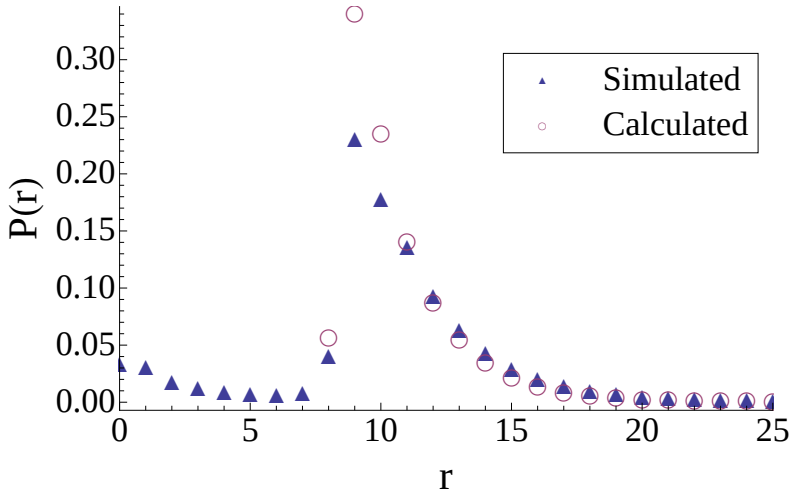

(a)

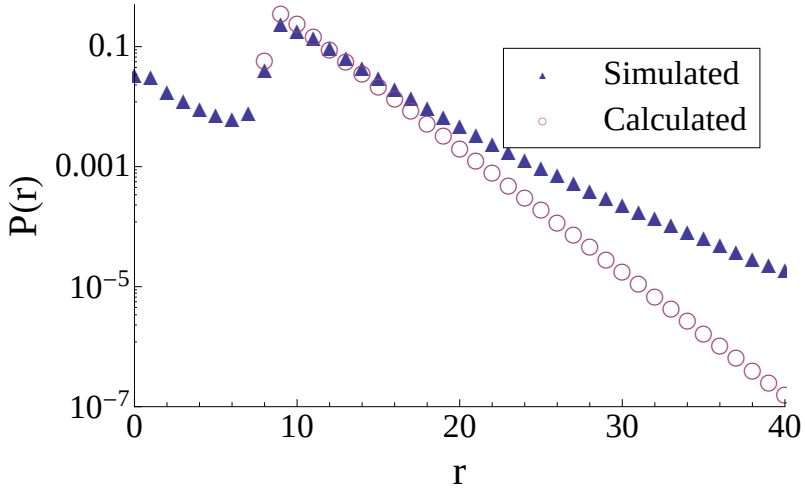

(b)

Figure 2.8: Comparison of the simulations and the analytic prediction of the nearest neighbor correlation at a higher density of 0.09 for $V_{\max} = 9$ and $p = 0.1$.

We find for $g \geq m + 2$ that

$$\begin{aligned} \Delta(g)_{t+1} - \Delta(g)_t &= A(\Delta(g-1)_t - \Delta(g)_t) + \\ &\quad B(\Delta(g+1)_t - \Delta(g)_t) + \\ &\quad C(\Delta(g+2)_t - \Delta(g)_t) \\ &\equiv \Phi[\Delta(g)]\,, \end{aligned} \tag{2.14}$$

where $A = p'(1-\alpha)$, $B = p' + \alpha(1-3p')$ and $C = \alpha p'$, with $p' = p(1-p)$. The evolution equations for smaller gaps are then

$$\begin{aligned}
\Delta(m+1)_{t+1} - \Delta(m+1)_t &= \Phi[\Delta(m+1)] + A\Delta(m-1)_t \\
\Delta(m)_{t+1} - \Delta(m)_t &= \Phi[\Delta(m)] \\
&+ (1-3p'+\alpha(1-2p'))\Delta(m-1)_t \\
\Delta(m-1)_{t+1} &= \alpha\,. \qquad (2.15)
\end{aligned}$$

In the continuum limit and for $g > m+1$, Eq. (2.14) becomes a drift-diffusion Fokker-Plank equation of the form

$$\frac{\partial \Delta}{\partial t} = \alpha \frac{\partial \Delta}{\partial g} + (p(1-p) + \alpha/2)\frac{\partial^2 \Delta}{\partial g^2}\,, \qquad (2.16)$$

for which the steady-state solution is of the form

$$\Delta(g) \propto \exp\left(-\frac{\alpha}{p(1-p)+\alpha/2}\, g\right)\,. \qquad (2.17)$$

If we solve Eqs. (2.14) and (2.15) and compare them to our simulations, we see from Figure 2.7 that the agreement is excellent except near the peak of the distribution. Since both distributions are normalized, the error at the peak results in slightly different slopes for large g. At higher densities, the agreement is not as good. Figure 2.8 shows the analytic description predicts the position of the peak at $g = V_{\max}$, but the presence of the second jam phase in the simulations alters the distribution.

If we assume that no cars have a gap of less than $V_{\max} - 1$, we showed that we can find $P(r)$ from a simple kinetic equation. For $r > V_{\max} + 2$, rewriting Eq. 2.16 in terms of the nearest neighbor correlation, $P(r)$ obeys a drift-diffusion Fokker-Planck equation in the continuum limit

$$\frac{\partial P(r)}{\partial t} = \alpha \frac{\partial P(r)}{\partial r} + (p(1-p) + \alpha/2)\frac{\partial^2 P(r)}{\partial r^2}\,, \qquad (2.18)$$

where $\alpha = P(V_{\max})$. The term $\alpha/2$ is the leading repulsive core correction to the diffusion constant. The steady state solution to the Eq. (2.18) for $r > V_{\max} + 2$ is

$$P(r) = P_0 \exp\left(-\frac{\alpha}{p(1-p) + \alpha/2}\, r\right), \tag{2.19}$$

where P_0 is a constant determined from solving the equations for $P(V_{\max}+1)$ and $P(V_{\max}+2)$ (Eq. 2.15), together with the normalization condition $\sum_r P(r) = 1$.

There is a simple interpretation of the form of Eq. (2.19). Each vehicle has an excluded region of size $\approx V_{\max}$ ahead of it. If the typical vehicle spacing is $L/N = 1/d$, the effective free space between vehicles is $1/d - V_{\max} \approx p(1-p)/\alpha + 1/2$. We can find an analytic value for $P(V_{\max} - 1)$ by:

$$P(V_{\max} - 1) = \alpha = \frac{p(1-p)}{1/d - V_{\max} - 1/2}\,. \tag{2.20}$$

In Figure2.9 it the calculated value of the $\alpha = P(V_{\max} - 1)$ has been compared to the values obtained for $P(V_{\max}-1)$ by direct simulation. It shows that although α is not perfectly representing the exact value for $P(V_{\max} - 1)$ (we did not expected that either), the rough estimate for the free effective space between the vehicles is a perfectly reasonable estimate.

2.3.2 Ornestein-Zerneke Equation

The model above assumes that no vehicles have a gap of less than $V_{\max} - 1$. The event that first results in a gap of $V_{\max} - 2$ requires a configuration of *three* cars, each separated by a gap of $V_{\max} - 1$, with the middle car then slowing down by the randomization rule while the last car does not. Thus we need three body interactions to see violations of this analytic model.

Since three-body interactions are neglected, we expect that the pair correlation function $G(r)$ in the dilute limit can be found from the nearest neighbor distribution $P(r)$ via an

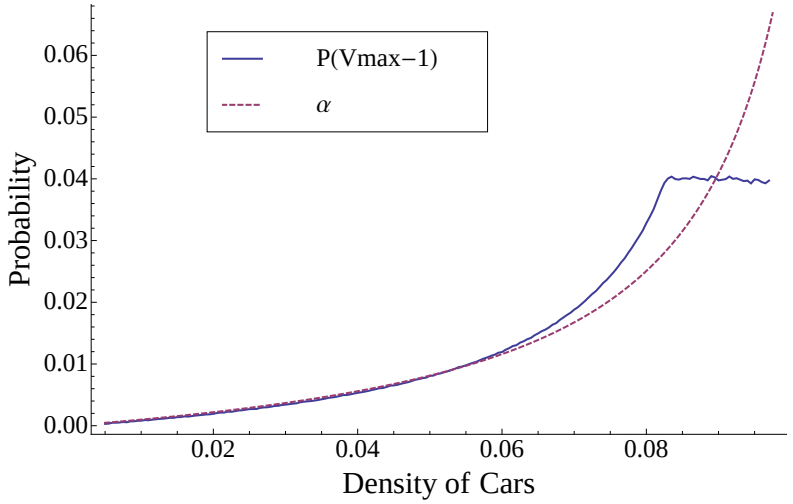

(a)

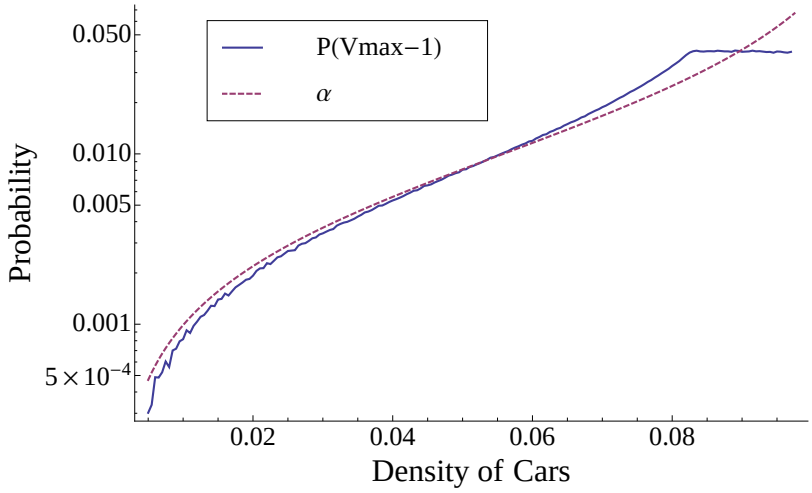

(b)

Figure 2.9: Comparison of the simulations and the analytic prediction for value of $P(V_{\max}-1)$ for $V_{\max} = 9$ and $p = 0.1$ in (a) regular and (b) semilog plot.

Ornstein-Zernicke relation

$$G(r) = P(r) + \sum_{i=1}^{r-1} P(i)\, G(r-i)\,. \tag{2.21}$$

Figure 2.10(a) shows an example in the free flow regime for that the $G(r)$ that we find from the Eq. (2.21) is indistinguishable from the $G(r)$ that we found directly from the simulations. That mean just the nearest neighbor distribution $P(r)$ in low density limit is

sufficient to build all the other correlation functions that we need to study the problem in this phase.

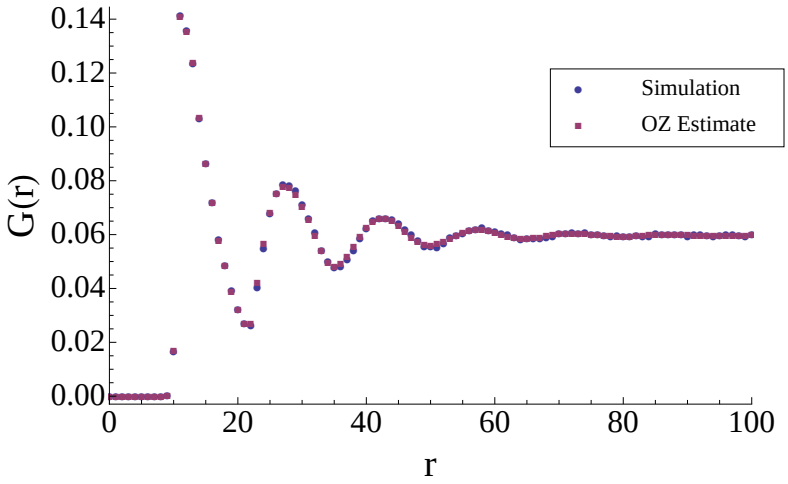

Figure 2.10: Simulated vs. Calculated pair correlation $G(r)$ for $V_{\max} = 11$, $p = 0.1$, $L = 10k$ for low density of $d = 0.06$. Plot shows that the calculated $G(r)$ using the just nearest neighbor correlation $P(r)$ from the Ornstein-Zernicke relation (Eq. 2.21) and the pair correlation $G(r)$ obtained from direct simulation are indistinguishable in the free flow phase.

Figure 2.11(a) shows the nearest neighbor correlation $P(r)$ and the $G(r)$ we get from the simulations in this regime. Since $P(r)$ is vanishingly small for $r < V_{\max}$, Eq. (2.21) predicts that $P(r)$ and $G(r)$ are identical up to $r = 2V_{\max}$ which Figure 2.11(a) shows. Figure 2.11(b) shows the corresponding structure factor $S(q)$. The peaks in $S(q)$ at multiples of $q = 2\pi/V_{\max}$ are simply the result of the repulsive core seen in $G(r)$. We note for future reference that $S(q)$ shows no upturn at $q \to 0$, indicating there is no long range order in the dilute regime.

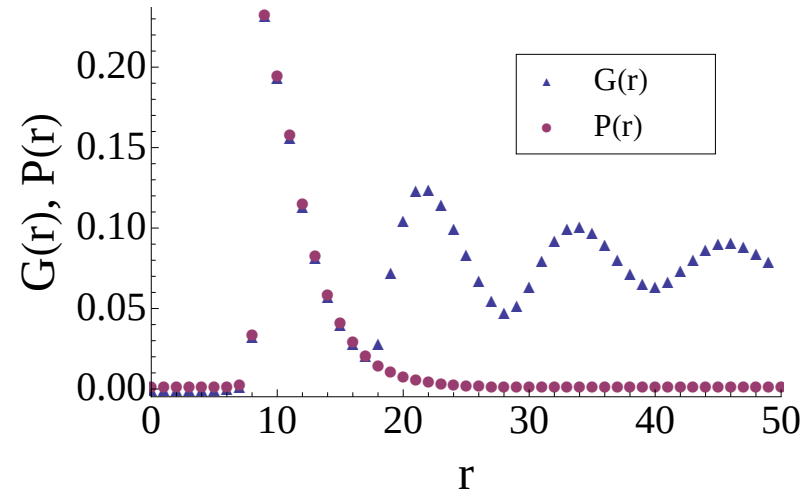

(a)

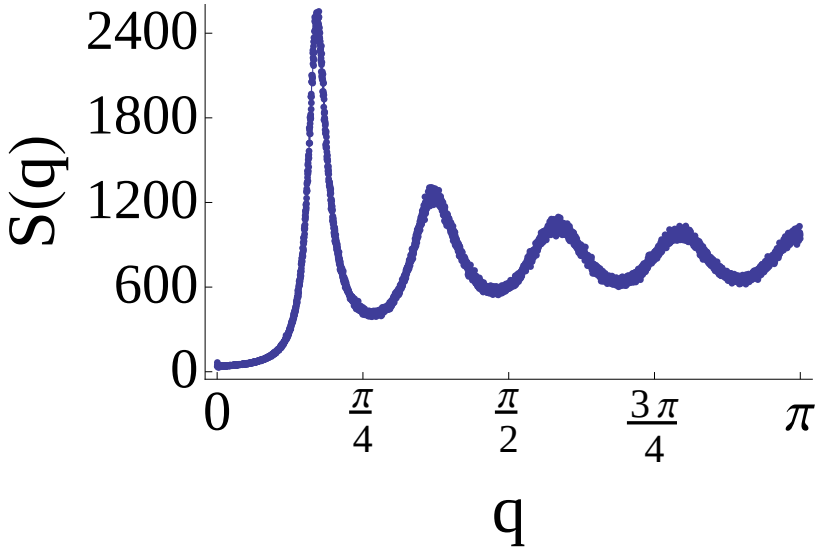

(b)

Figure 2.11: (a) Simulated nearest neighbor distribution $P(r)$ and pair correlation $G(r)$ for $V_{\max} = 9$ and $p = 0.1$ at a density $d = 0.08$. (b) Structure factor $S(q)$ obtained from $G(r)$ through Eq. (2.21) and from simulations.

2.3.3 Nearest Neighbor Correlation; Evolution of P(r)

Nearest neighbor correlation $P(r)$ is identical to the distribution of gaps $g(r\prime)$ where $r\prime = r-1$. It is shown that in the dilute limit, the NS model acts like a repulsive core gas with nearest neighbor correlation. Therefore $P(r)$ plays a key role in identifying the correlation functions in the model. Figures 2.12 and 2.13 show the evolution of the nearest neighbor distribution of the cars $P(r)$ for two cases of low value of $V_{\max} = 5$ and high value of $V_{\max} = 9$. In both cases we have covered a range of densities from well before the transition to well after that. The topic of transition will be discussed in details in next chapter. For future references note that all the values of $P(r < V_{\max} - 2) \simeq 0$ for the densities before the transition and there is an abrupt raise in the value of $P(0)$ at the transition (Figure 2.12(d) and 2.13(f)) .

A more complete perspective of the nearest neighbor correlation could be found by looking at the evolution of the $P(r)$ and specific values of r for different values of $V_{\max}$. Comparing the plots for different densities in Figures 2.12 and 2.13, one can find that the peaks happen at $r = V_{\max}$ and $r = 0$. So the evolution of $P(V_{\max})$ and $P(0)$ would be our subject of inerest. In addition to that we already mentioned the key role of value of $P(V_{\max} - 1)$ in the drift-diffusion equation of the gap distribution in the dilute phase.

Figures 2.14, 2.15 and 2.16 show the evolution of the nearest neighbor correlation $P(V_{\max})$, $P(V_{\max} - 1)$ and $P(0)$ respectively. Note how behavior of the $P(r)$ changes by increasing the value of $V_{\max}$. We will refer to this phenomena later at the length dependent transition section.

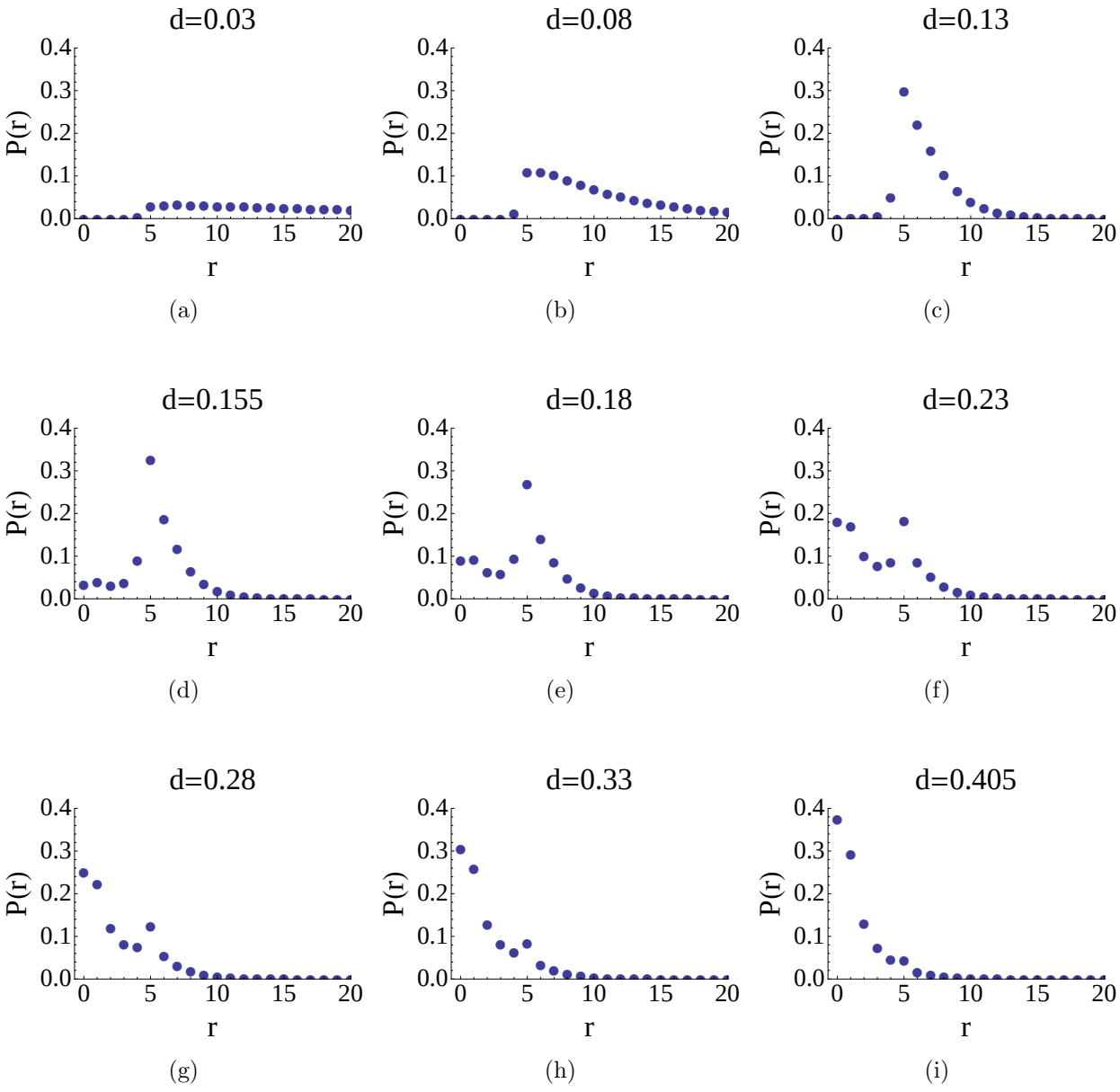

Figure 2.12: Nearest neighbor correlation $P(r)$ vs. r for a range of densities fronm below the transition to above that for $V_{\max} = 5$ and $p = 0.1$. All the values of $P(r < V_{\max} - 2) \simeq 0$ for the densities before the transition and there is an abrupt raise in the value of $P(0)$ at the transition (d).

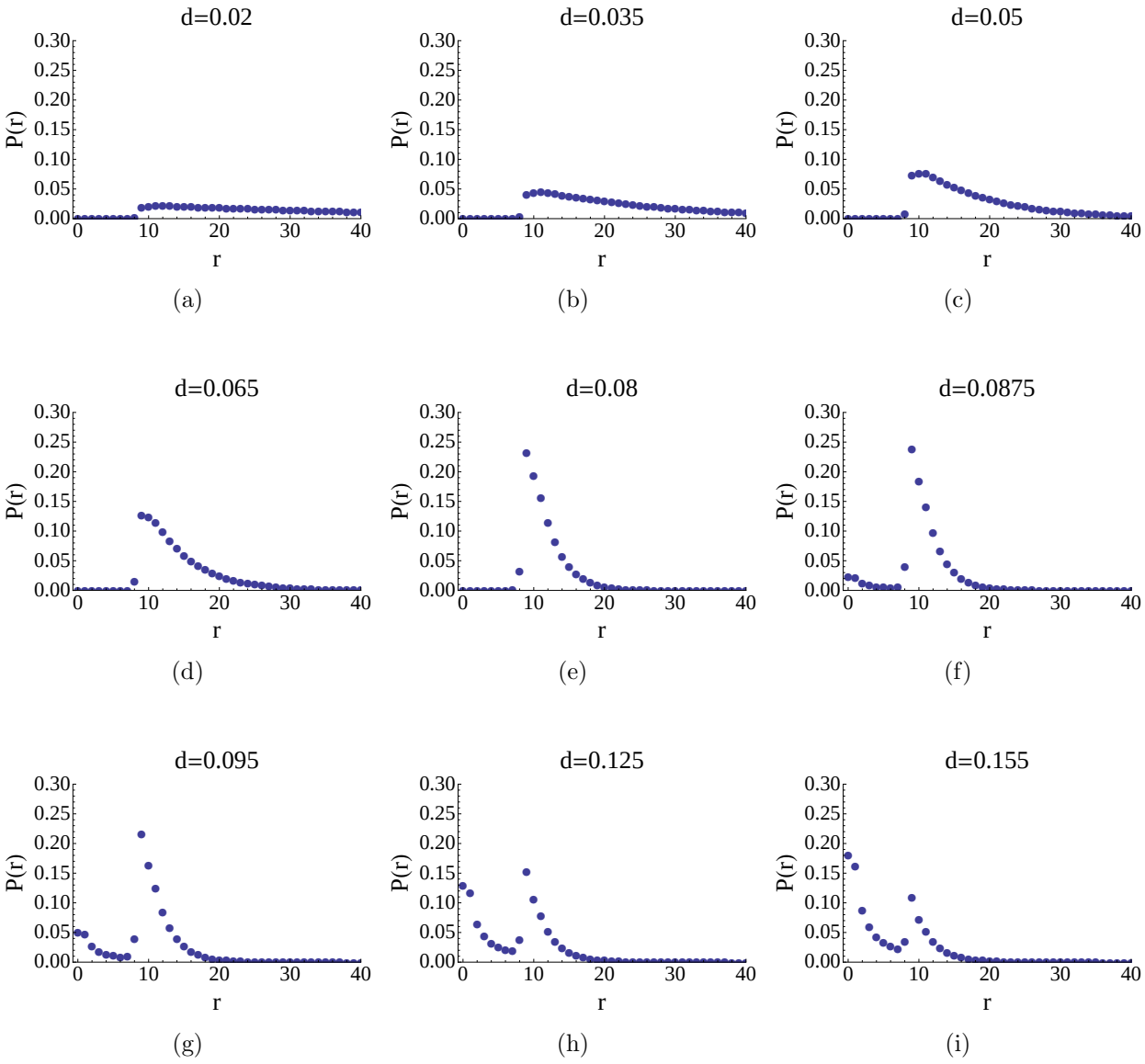

Figure 2.13: Nearest neighbor correlation $P(r)$ vs. r for a range of densities from below the transition to above that for $V_{\max} = 9$ and $p = 0.1$. All the values of $P(r < V_{\max} - 2) \simeq 0$ for the densities before the transition and there is an abrupt raise in the value of $P(0)$ at the transition (f).

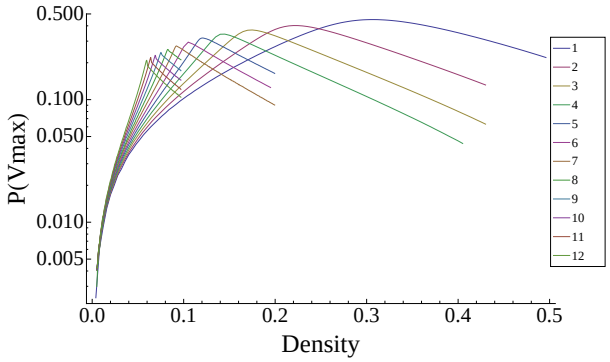

Figure 2.14: Evolution of nearest neighbor correlation function $p(V_{\max})$ vs. density for different values of $V_{\max}$.

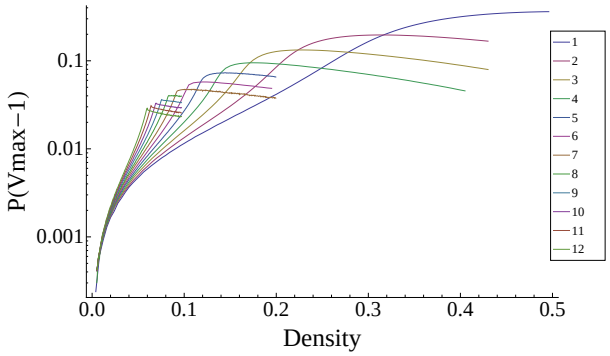

Figure 2.15: Evolution of nearest neighbor correlation function $p(V_{\max} - 1)$ vs. density for different values of $V_{\max}$.

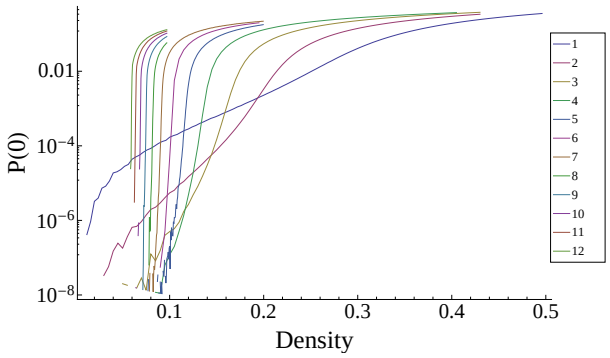

Figure 2.16: Evolution of nearest neighbor correlation function $p(0)$ vs. density for different values of $V_{\max}$.

2.4 Finite-Size Effects: Long-Range Correlation

2.4.1 Observing Long-Range Correlation at the Transition

As the vehicles density is raised, the repulsive core gas description we developed above remains qualitatively correct, with a gradual growth in the number of vehicles spaced at shorter distances $V_{\max}-2$, $V_{\max}-3$, ... When the jams appear, we see an abrupt change in the shape of the nearest neighbor distribution $P(r)$ with the sudden appearance of a nonzero fraction of vehicles with $r = 1, 2$ or respectively the probability of finding $gap = 0$ *or* 1 as shown in Figures 2.12 and 2.13. Figure 2.17 shows that as the transition density is passed, the calculated $G(r)$ using the just nearest neighbor correlation $P(r)$ from the Ornstein-Zernicke relation (Eq. 2.21) does not match the pair correlation $G(r)$ directly found from the simulation any more.

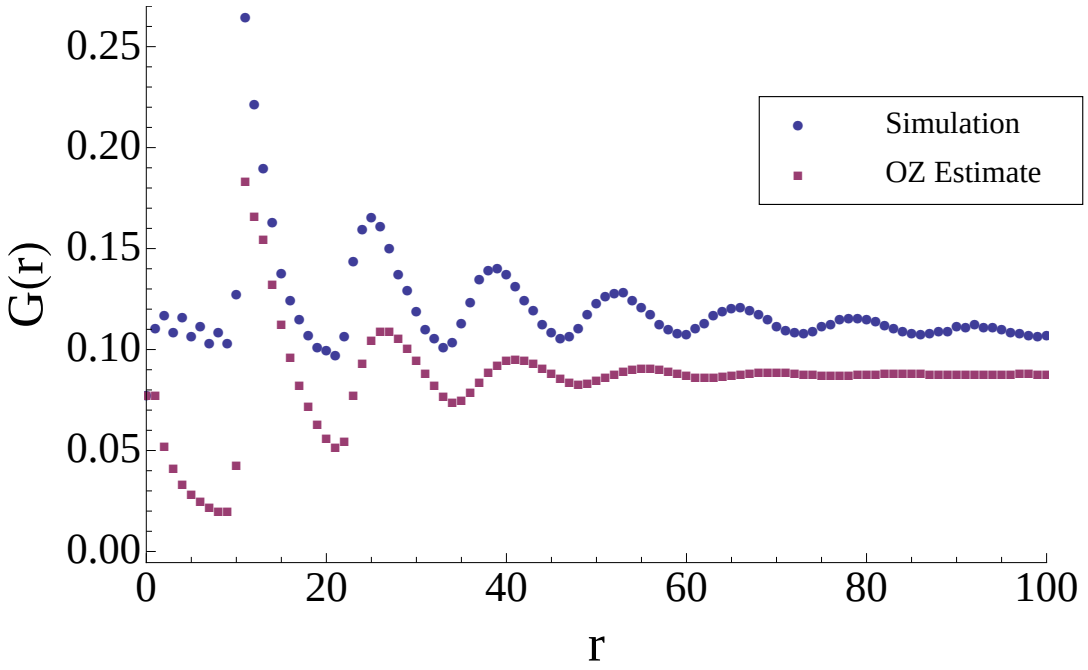

Figure 2.17: Simulated vs. Calculated pair correlation $G(r)$ for $V_{\max} = 11$, $p = 0.1$, $L = 10k$ for high density of $d = 0.088$, Plots show that the calculated $G(r)$ using the just nearest neighbor correlation $P(r)$ and the Ornstein-Zernicke relation (Eq. 2.21) do not agree in the jammed phase.

As Figure 2.18(a) shows, the pair correlation $G(r)$ no longer agrees with $P(r)$ for $r \leq 2V_{\max}$, and the Ornstein-Zernicke relation (2.21) between the two no longer holds. At the same time, Figure 2.18(b) exhibits an upturn in $S(q)$ for $q \to 0$, indicating the appearance of long range correlations in the density.

We interpret this as indicating that the free flow phase is still stable, but that we have nucleated a new phase of localized jams that appear and disappear. Indeed, by examining the permanent stability of a localized jam, Gerwinski and Krug [28] have shown that the jams should should be permanently at a density $\geq (1-p)/(1+V_{\max}-2p)$, which is a higher density than where we see the onset of jams. The upturn in $S(q)$ for small q indicates some long-range order, which implies that we might observe finite-size effects in various quantities that are sensitive to the presence of that long range order. In the coming chapters we will examine the existence of such finite-size effects in the NS model.

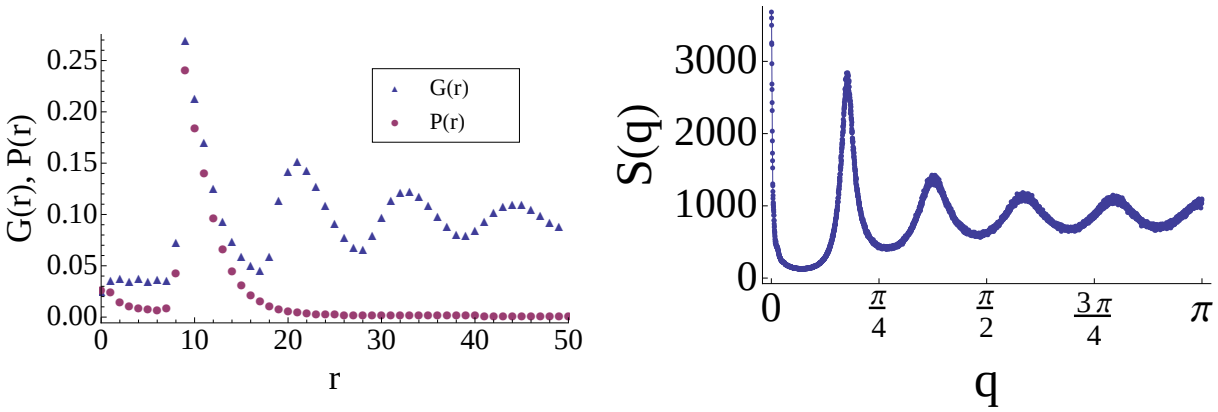

(a) (b)

Figure 2.18: (a) Nearest neighbor distribution $P(r)$ and pair correlation $G(r)$ for $V_{\max} = 9$ and $p = 0.1$ for a density $d = 0.088$, just above the density where jams appear. (b) Corresponding structure factor $S(q)$ with an upturn near $q \to 0$.

2.4.2 Finite-Size Effects in Fundamental Diagrams for $V_{\max} \gtrsim 7$

The fundamental diagrams introduced in Section I, are the first candidates to be checked for the possibility of existence of finite-size effects in the system. Figure 2.19 shows how the average velocity changes with density for different values of $V_{\max}$ and different track lengths. For $V_{\max} \lesssim 6$ we observe no length dependence. The figure also shows that once the density is well above the transition density, the system is insensitive to both the value of $V_{\max}$ and the system size.

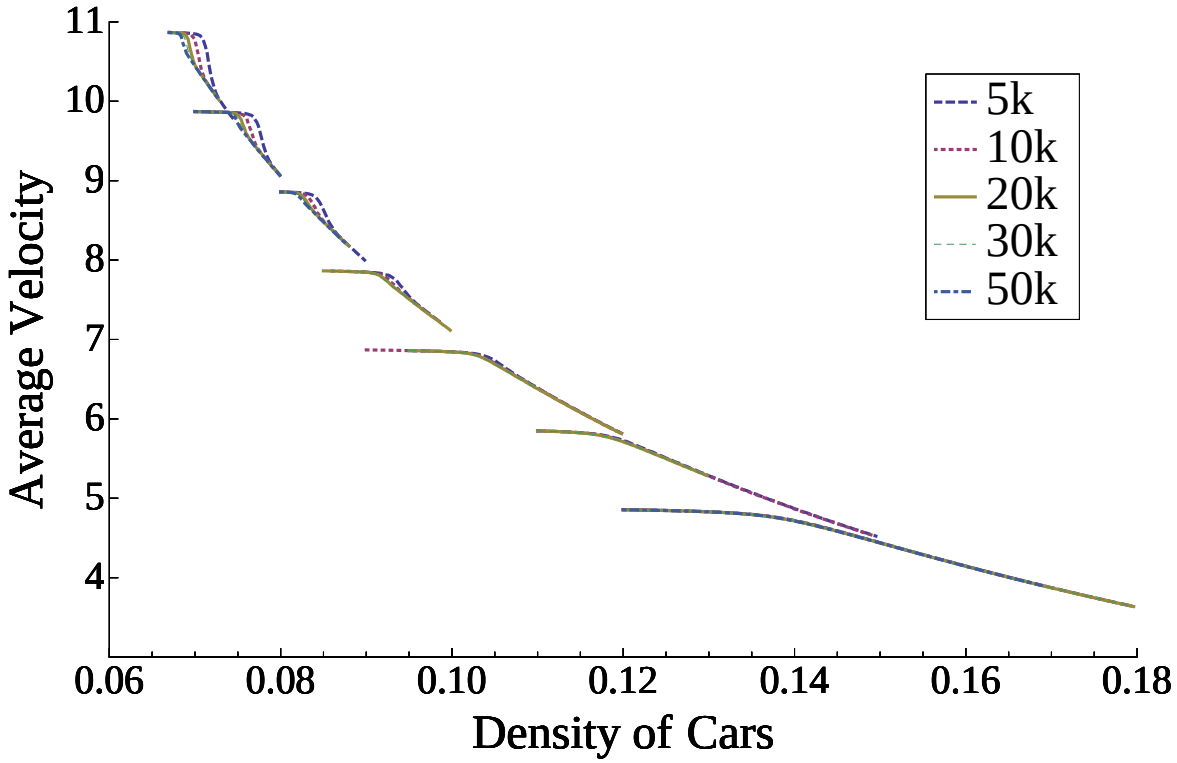

Figure 2.19: The dependence of the mean velocity on density for various values of $V_{\max}$ and $p = 0.1$, and a variety of track lengths (shown as different colors). The average velocity of the cars for different lengths varies at the transition for values of $V_{\max} \gtrsim 7$.

Figure 2.20(a) shows a zoomed version of Figure 2.19 for value of $V_{\max} = 5$. The plot shows that there is no size sensitivity observable for different track lengths. Figure 2.20(b) shows that the finite-size effect if perfectly observable for $V_{\max} = 9$. The system with shorter

tracks show a delay in dropping the average velocity. In other words the tradition happens at a higher density for the shorter track lengths.

This size sensitivity is even more apparent in the mean flux of vehicles, presented in Figure 2.21. As in the Figure 2.19 shown, it is only for $V_{\max} \gtrsim 7$ that we see this size sensitivity. This figure shows that for a given track length, there could be a value of $V_{\max}$ for which the system has the maximum current. For example, at $d = 0.08$, the vehicle flux with $V_{\max} = 10$ is greater than any other value of $V_{\max}$.

Figures 2.22 (a) and (b) show the average flux vs. density for different teack length for values of $V_{\max} = 5$ and $V_{\max} = 9$ respectively. The size sensitivity of the average flux diagram shows that in a system of smaller size, the vehicle flux is actually higher than it is in larger systems, and that the size of the effect depends on $V_{\max}$. This behavior is the reverse of what one would expect from hysteresis, where a large system would get trapped in a high flux free flow regime while a smaller system would not.

Since the value of $V_{\max}$ represents the number of degrees of freedom for each car, it is not surprising that the finite-size behavior can depend on the number of degrees of freedom, as it does in equilibrium systems. However, we do not have any clear evidence that there is a critical value of $V_{\max}$ for which the finite-size effects appear, but they are clearly suppressed for $V_{\max} \leq 6$.

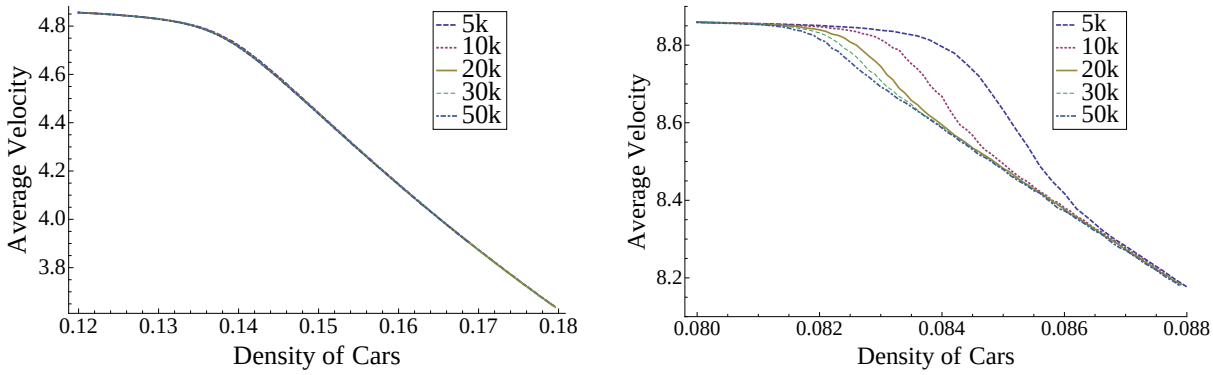

Figure 2.20: Average velocity vs. density for different track lengths and $p = 0.1$ for (a) $V_{\max} = 5$ and (b) $V_{\max} = 9$.

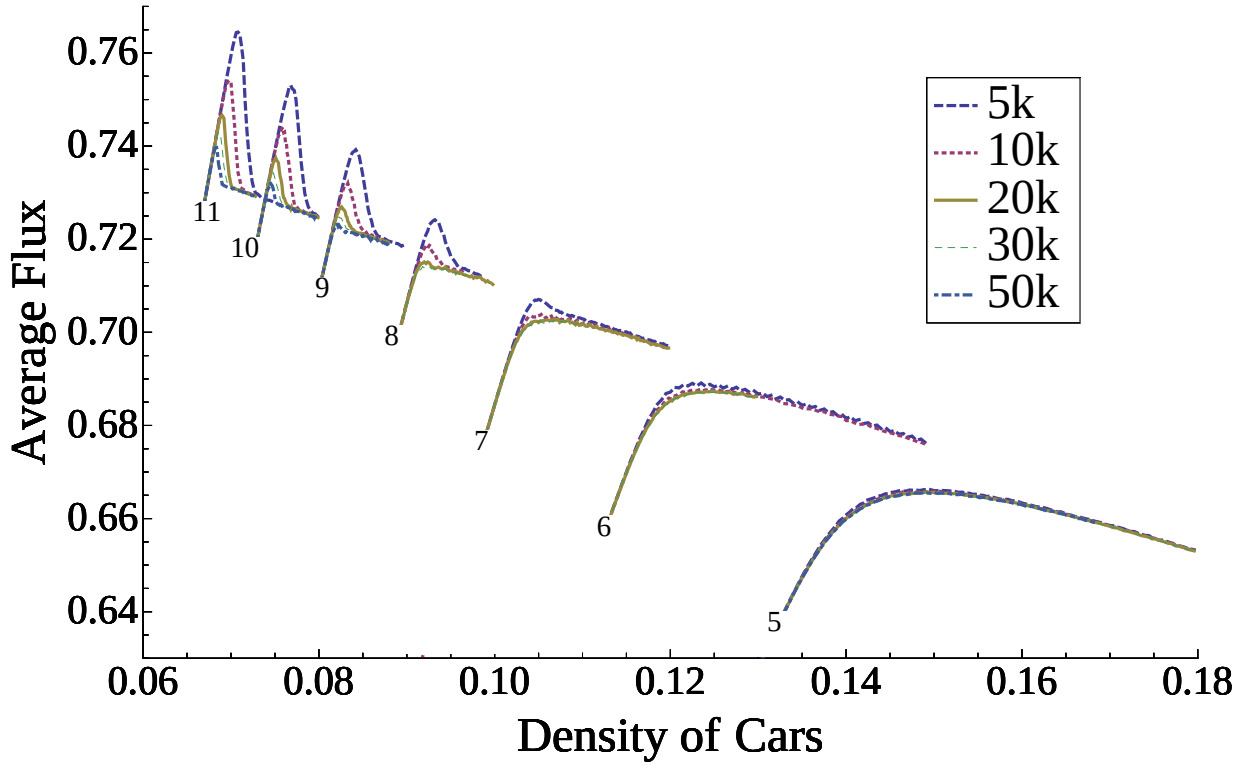

Figure 2.21: The average flux vs. density for various $V_{\max}$ with $p = 0.1$ and track lengths (different colors) of $L =$ 5k, 10k, 20k, 30k, 40k, 50k.

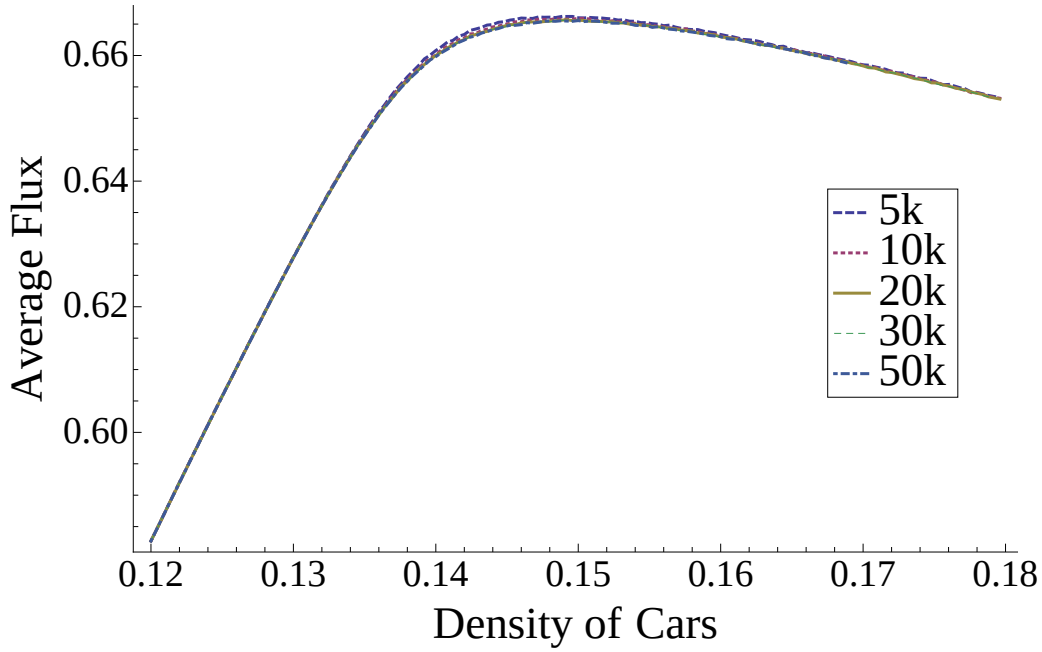

(a)

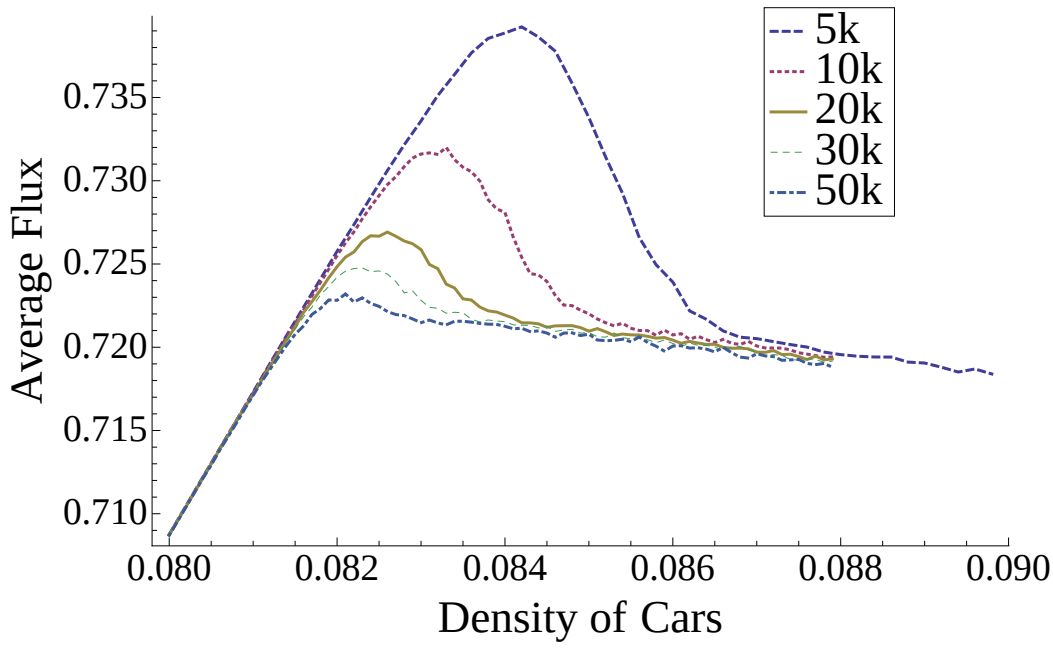

(b)

Figure 2.22: Average flux vs. density for different track lengths and $p = 0.1$ for (a) $V_{\max} = 5$ and (b) $V_{\max} = 9$.

2.4.3 Well-Defined Order Parameter

To characterize the transition, we need a quantity sensitive to the presence of jams. We discussed in the introduction a variety of choices that others have used that are based on the velocity distribution. In this study, where we focus on the spatial distribution of the cars, we have used the gaps rather than the vehicle speeds to characterize the jams. The gap rule, however, produces a strong correlation between the speed of a vehicle and the distance to the next car, so our order parameter is closely related to these other choices.

Figure 2.23 shows how the probability of finding gaps of different sizes varies with density near the transition. We see that the probability of having a gap $\leq V_{\max}/2$ changes dramatically here. Therefore, we will define the order parameter x_0 to be the fraction of vehicles with a gap $\leq V_{\max}/2$. We could have used just the vehicles with a gap of zero [20], but using all of these gaps gives us more reliable statistics.

Figure 2.24 shows that this order parameter x_0 exhibits the same finite-size effects, including its dependence on $V_{\max}$, that we observed for the mean flux and velocity. Figures 2.25 (a) and (b) are zoomed versions of Figure 2.24 for values of $V_{\max} = 5$ and $V_{\max} = 9$ respectively. These finite-size effects suggest that the phase transition from the free flow phase to the jammed phase does not occur as first order phase transition, at least for values of $V_{\max} \gtrsim 7$.

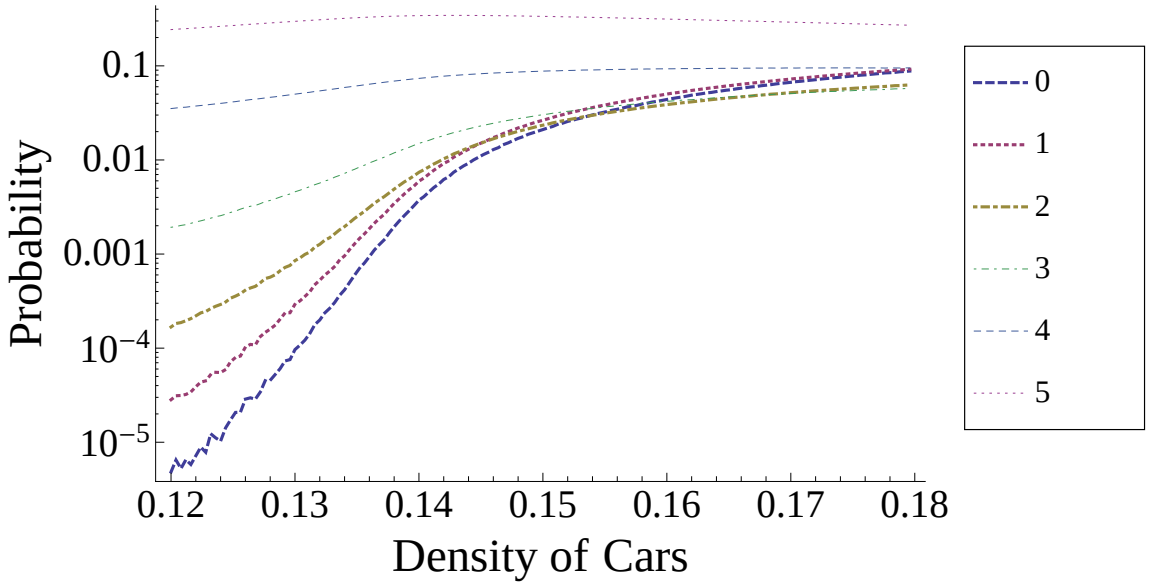

(a)

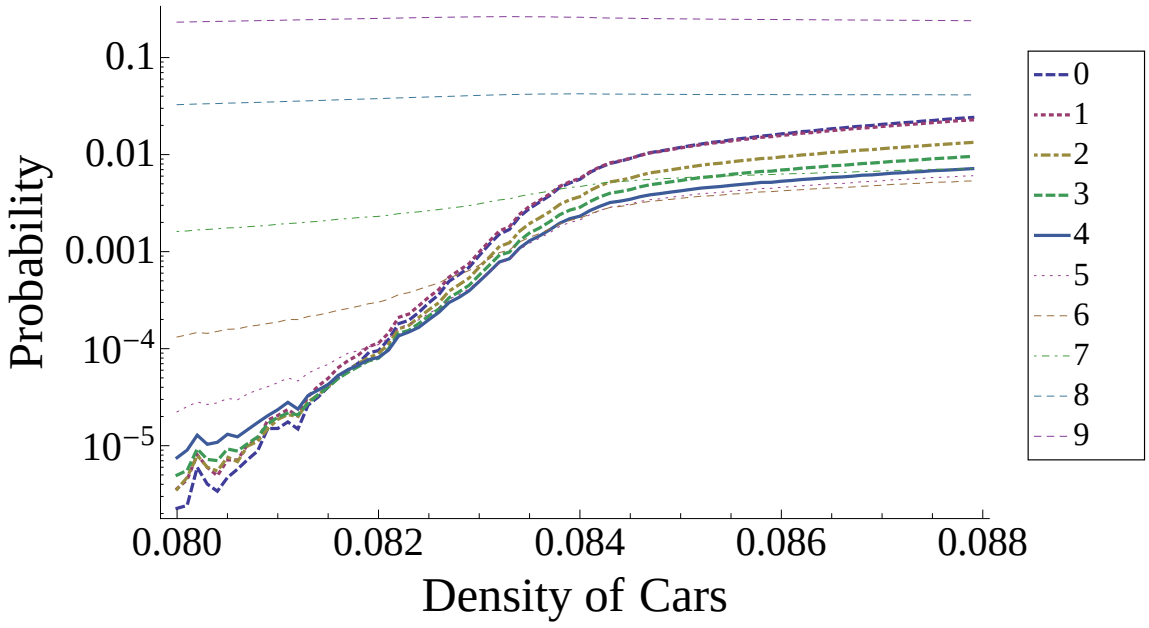

(b)

Figure 2.23: Probability of finding a gap of a particular size for various densities for $p = 0.1$ and values of (a) $V_{\max} = 5$ and (b) $V_{\max} = 9$. The change in values of $gap < V_{\max}/2$ (thick lines) is more abrupt at the transition than other values of gap.

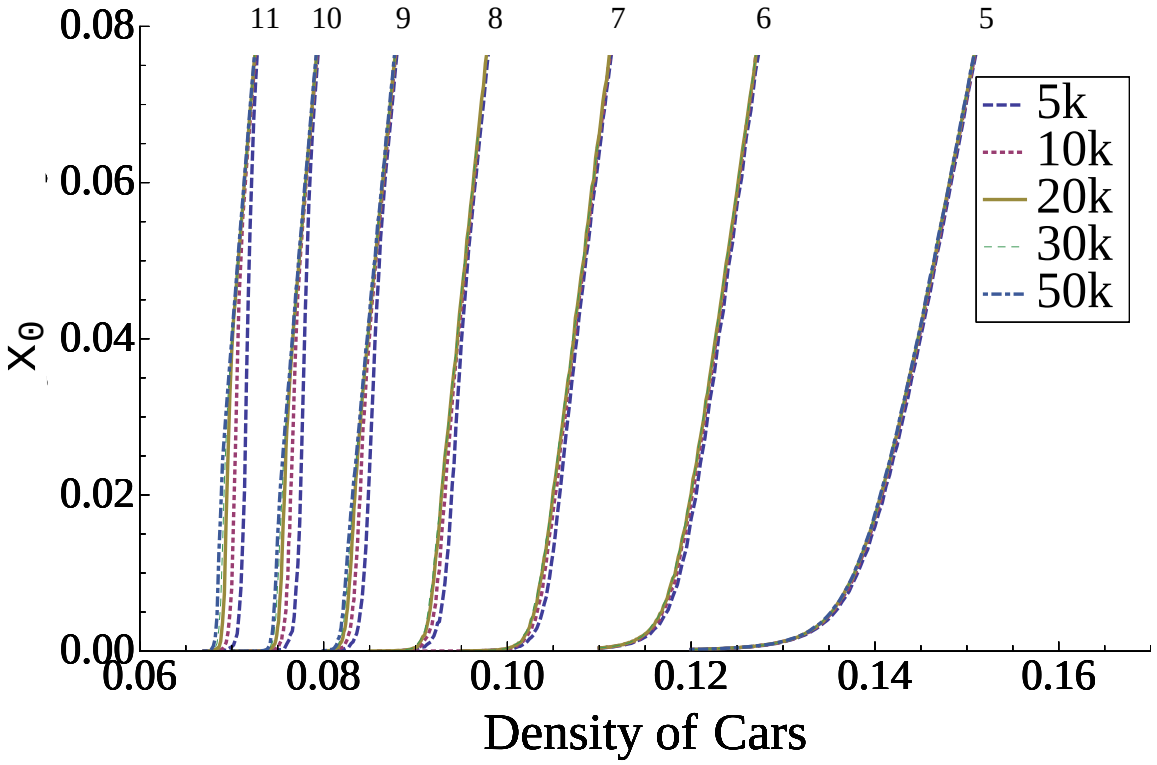

Figure 2.24: Probability of having gap $\leq V_{\max}/2$ for different track lengths and $p = 0.1$ for various value of $V_{\max}$. The finite-size effects is observable for the order parameter x_0 for values of $V_{\max} \gtrsim 7$.

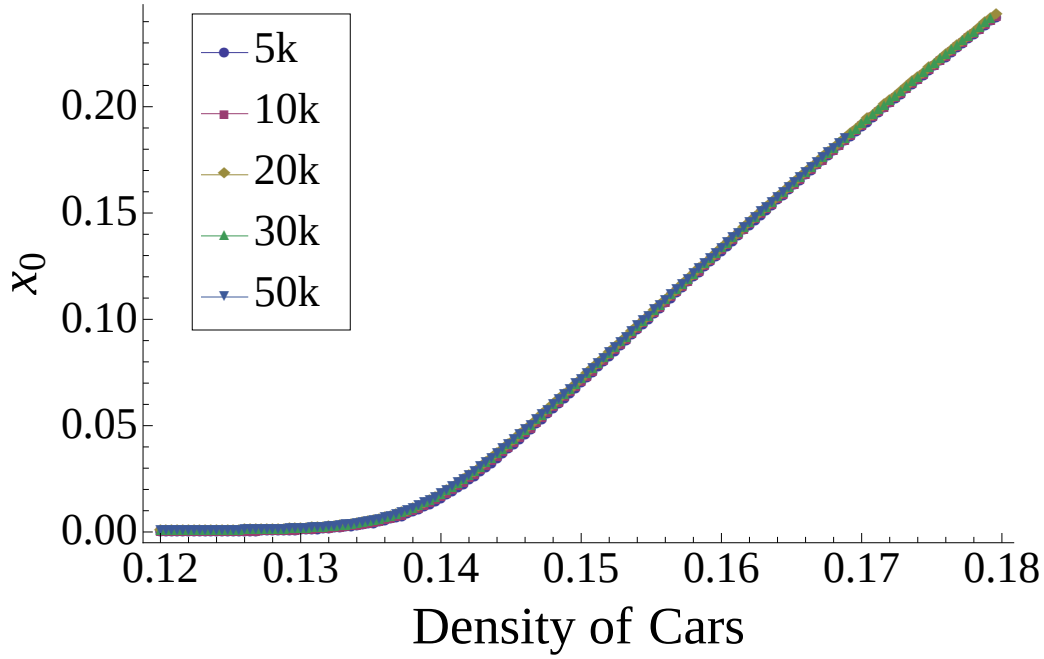

(a)

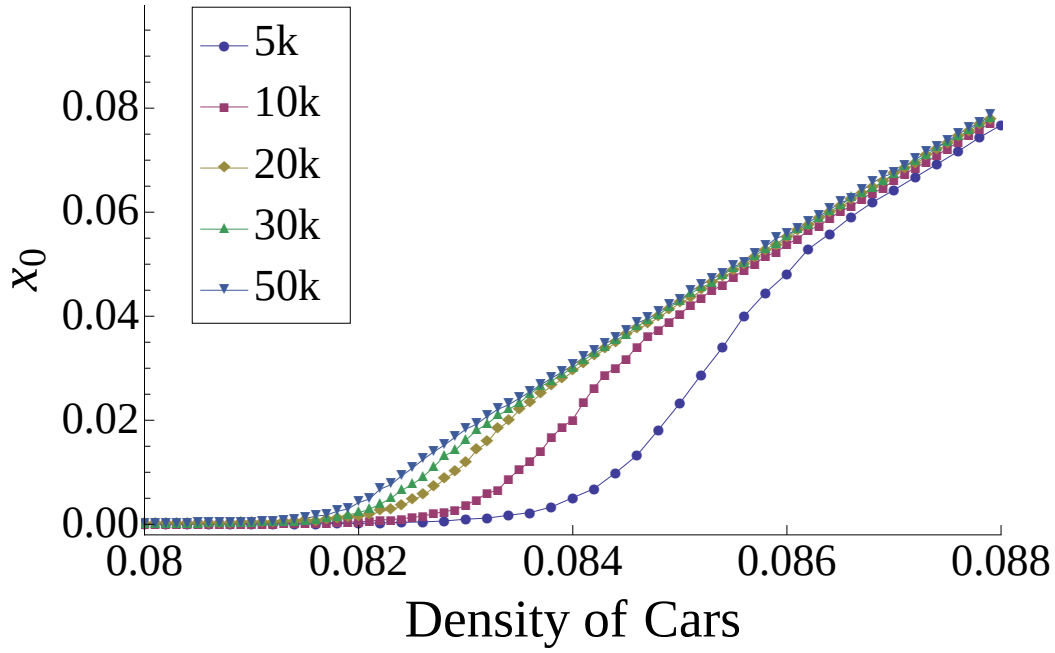

(b)

Figure 2.25: Probability of having gap $\leq V_{\max}/2$ for different track lengths and $p = 0.1$ for (a) $V_{\max} = 5$ and (b) $V_{\max} = 9$.

2.4.4 Examining More Order Parameters

As discussed in the Introduction, many other quantities have been used to characterize the distinct phases in the NS traffic flow model. We intend to show that the finite-size effects are observable for all these different order parameters. We briefly introduce a list of possible order parameters and show their behavior with at the transition area for various values of track length for the case of $V_{\max} = 9$.

The *gap rule* in the NS model causes a strong correlation between the gap distribution and the velocity distribution for the values of gap and velocity smaller than $V_{\max}$. Therefore we define the order parameter v_0 to be the fraction of cars with velocity less than or equal to $V_{\max}/2$. Figure 2.26 (a) and (b) show that the plots for x_0 and v_0 are very similar and the same finite-size effects could be observed for the quantity v_0. We could have just used the standing cars or the fraction of cars with $v = 0$ instead as many others have suggested [20]. The reason we prefer v_0 is to get the better statistics.

We have already shown that the finite-size effects are clearly observable in the fundamental diagram for velocity. The other quantity that may worth to be analyzed is the average variance in the velocity of cars. Figure 2.27 shows the average variance also shows the similar size sensitive behavior for the system with $V_{\max} = 9$. All these four order parameters (x_0, v_0, $\langle V \rangle$ and $\mathrm{Var}(V)$) show an abrupt change at the transition.

A well-defined order parameter should have a zero value at one side of the transition and a nonzero value at the other side. x_0 and v_0 are almost zero at the dilute phase and suddenly raise at the transition to the jammed phase. To produce a well-define order parameter from $\langle V \rangle$ and $\mathrm{Var}(v)$, we need to get help from our analytical model. We first use the $P_v(r)$ (velocity distribution) obtained from our analytical model described in Free Flow Phase Section, to find the supposed plots for $\langle V \rangle_{\mathrm{free}}$ and $\mathrm{Var}(V)_{\mathrm{free}}$. That means if there was no transition in the system, how these two parameters would evolve. Note that the analytical model we discussed is based on the vehicles just interact with their nearest neighbors. We know that this assumption would fail the transition because of the growth of the long range

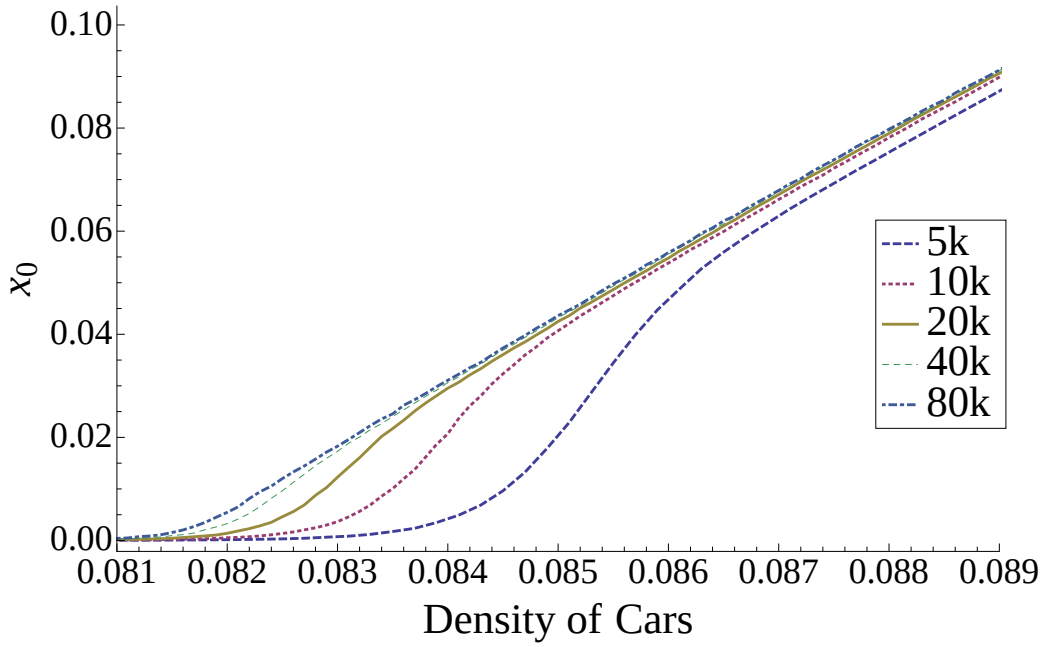

(a)

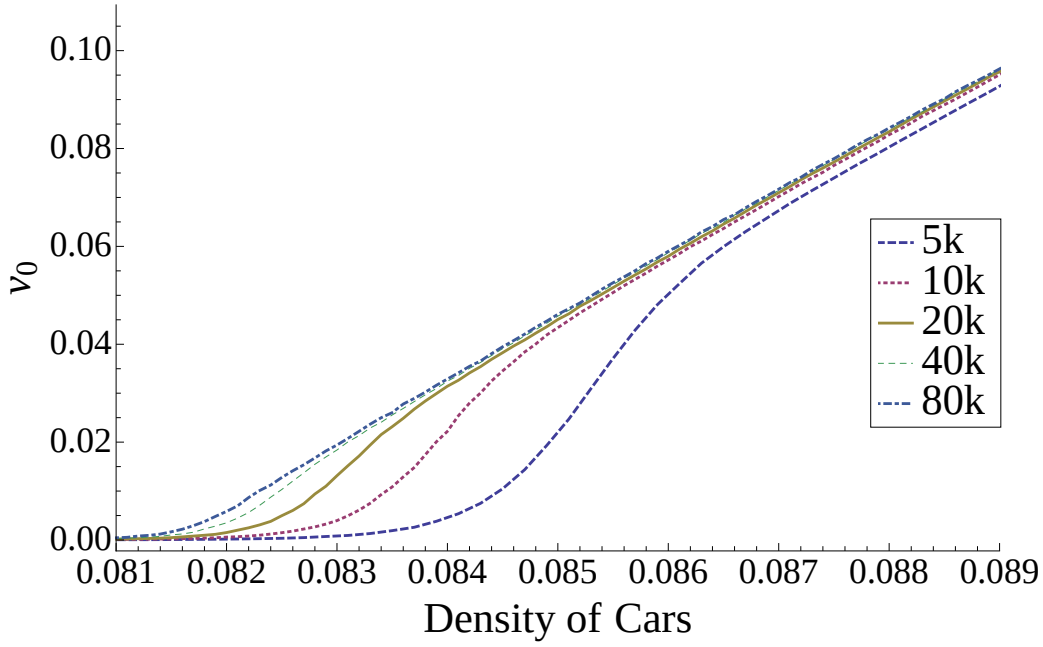

(b)

Figure 2.26: Plots of order parameters (a) x_0: probability of having gap $\leq V_{\max}/2$ and (b) v_0: probability of having velocity $v \leq V_{\max}/2$ for different track lengths and $p = 0.1$ for $V_{\max} = 9$.

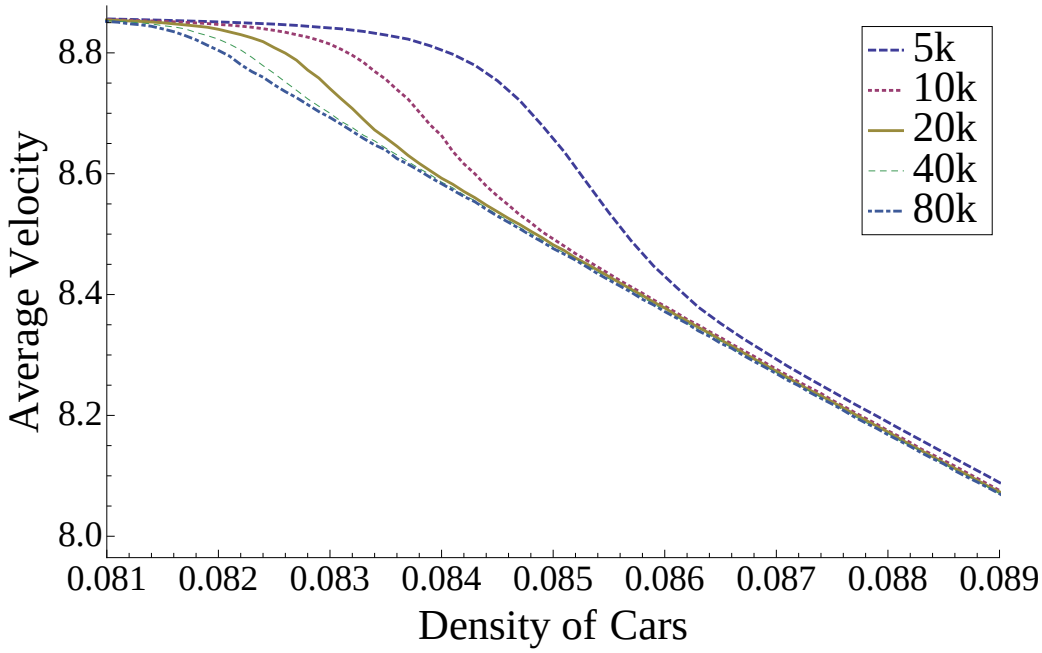

(a)

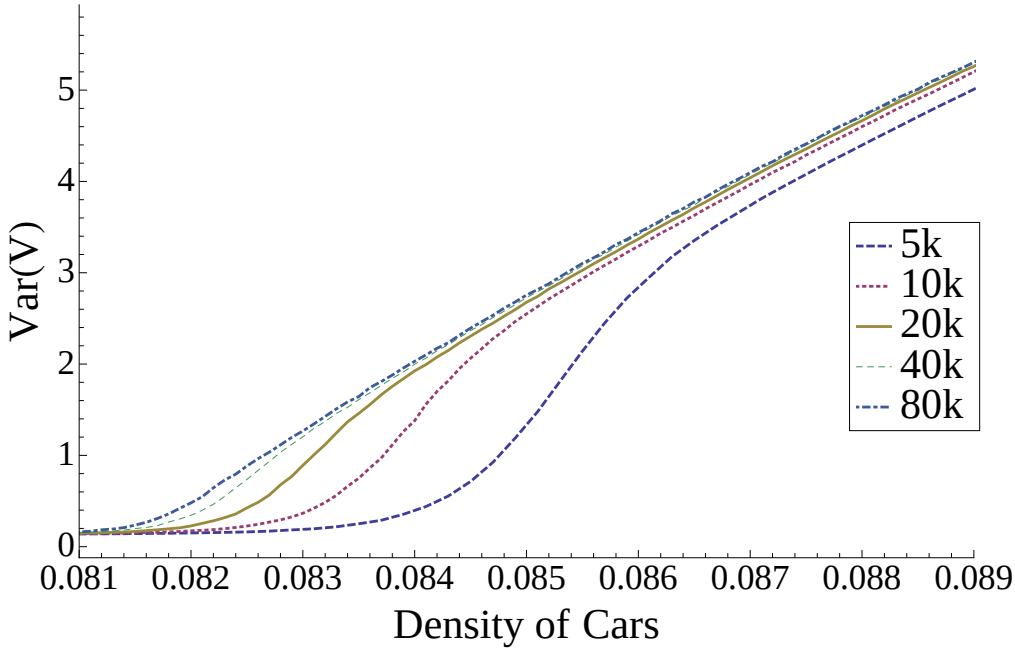

(b)

Figure 2.27: Plots of order parameters (a) $\langle V \rangle$: Average velocity and (b) Var(V): Average variance in the velocity, for different track lengths and $p = 0.1$ for $V_{\max} = 9$.

correlation. But we still can obtain what the values of $\langle V \rangle_{\text{free}}$ and $\text{Var}(V)_{\text{free}}$ would have been, if there was no such long range correlation in the system. Figure 2.28 (a) and (b) show the behavior of $\langle V \rangle_{\text{free}}$ and $\text{Var}(V)_{\text{free}}$ respectively. Note that there is no size dependence in the free flow phase. Now we can our new well-defined order parameters to be the variation of $\langle V \rangle$ and $\text{Var}(V)$ from their supposed values to be if there was no transition. In Figure 2.29 we show how the order parameters $\langle V \rangle - \langle V \rangle_{\text{free}}$ and $\text{Var}(V) - \text{Var}(V)_{\text{free}}$ are well-defined order parameter and show the same finite-size effects at the transition as x_0 and v_0 did.

Sudden raise from zero values to a nonzero value is not the only type of behavior characteristic of the order parameters at the transition. To find the critical density, the typical approach [29] is to study a quantity like a susceptibility that has a peak at the transition. The already introduce order parameters have no maximum at the transition. While at first thought, a quantity like $\langle x_0^2 \rangle$ might act like a susceptibility, we have found that this jamming transition is not like an equilibrium transition with large fluctuations in the order parameter correlations before the transition. Instead, we are seeing the nucleation of a different phase (the jams) in a background of the free phase, and the fluctuations in x_0 basically track x_0.

Instead, we can examine the dynamic susceptibility, χ_4, which was used to study glassy behavior in the NS model in the $p \to 1$ limit [26]

$$\chi_4 = \frac{1}{\langle v^2 \rangle - \langle v \rangle^2} \left\langle \frac{1}{N} \sum_{i=1}^{N} \sum_{j=0}^{N} (v_{\text{i}} - \overline{v})(v_{\text{J}} - \overline{v}) \right\rangle , \tag{2.22}$$

where v_{i} is the velocity of the i-th car at a particular time and $\overline{v}$ denotes the mean speed of all the cars at that time. χ_4 measures the number of vehicles that move cooperatively. Note that the expression for χ_4 here is the equal time correlation $\chi_4(0)$ used in Ref. [26].

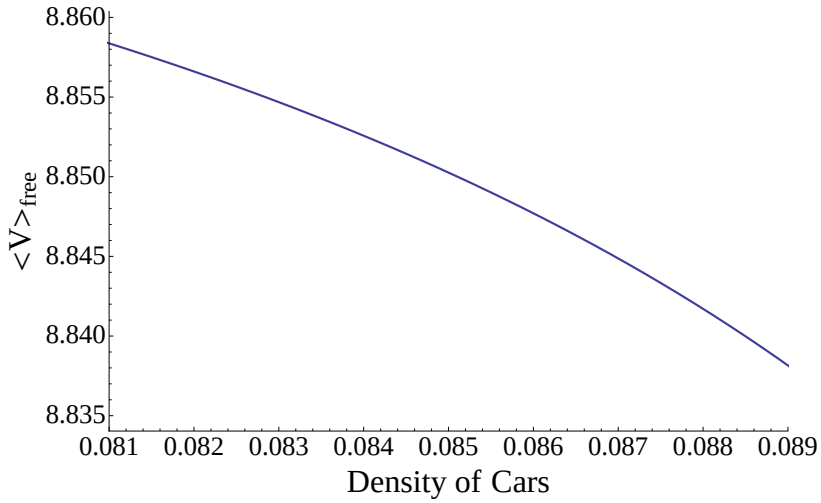

(a)

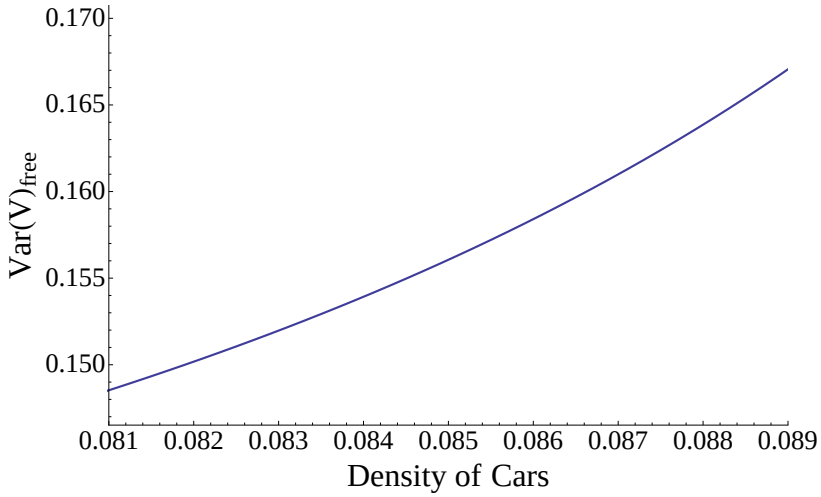

(b)

Figure 2.28: Plots of supposed free flow phase values for parameters (a) $\langle V \rangle_{\text{free}}$: Average velocity and (b) $\text{Var}(V)_{\text{free}}$: Average variance in the velocity, obtained from the analytical model for $p = 0.1$ for $V_{\max} = 9$.

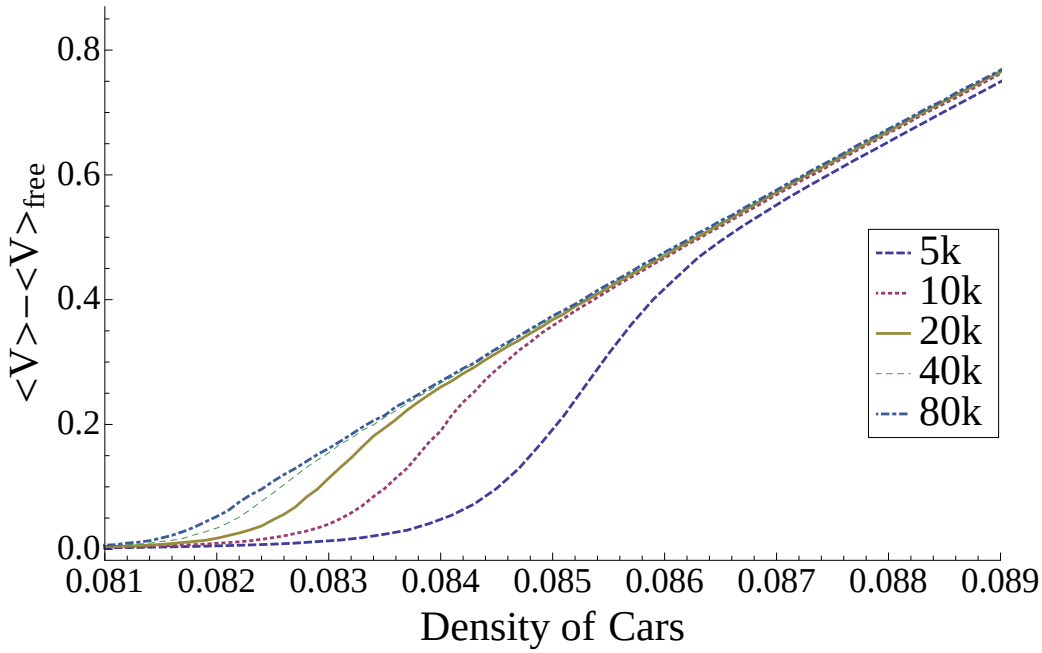

(a)

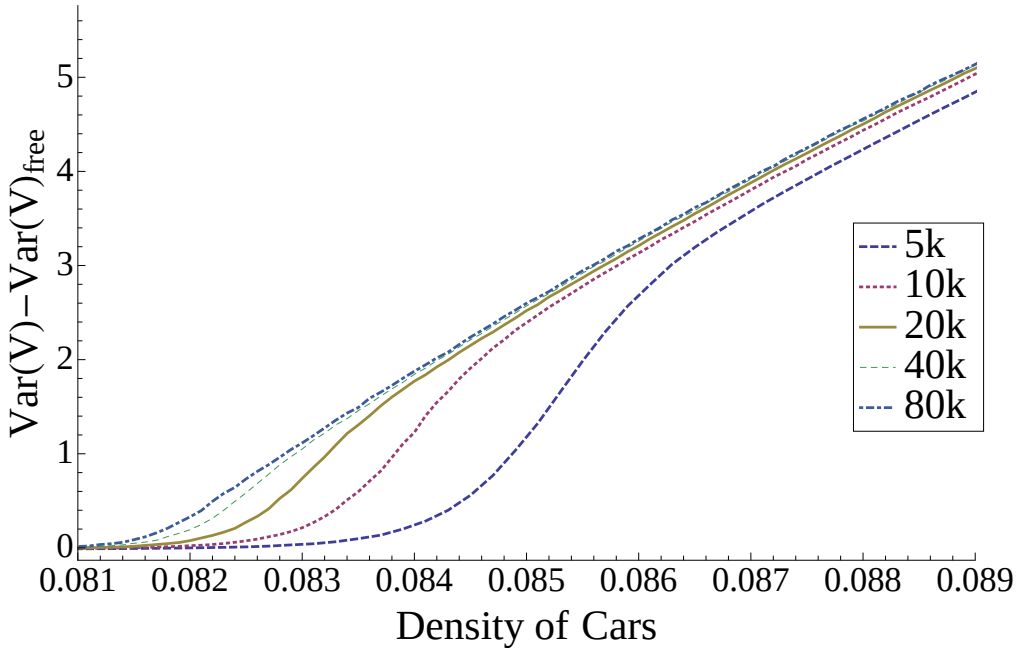

(b)

Figure 2.29: Well-defined order parameters (a) $\langle V \rangle_{\text{free}}$: Variation of the average velocity and (b) $\text{Var}(V)_{\text{free}}$: Variation of the average variance in the velocity from the supposed free flow phase for different track lengths and $p = 0.1$ for $V_{\text{max}} = 9$. The values of the order parameters are zero at the free flow phase and show and abrupt change at the transition.

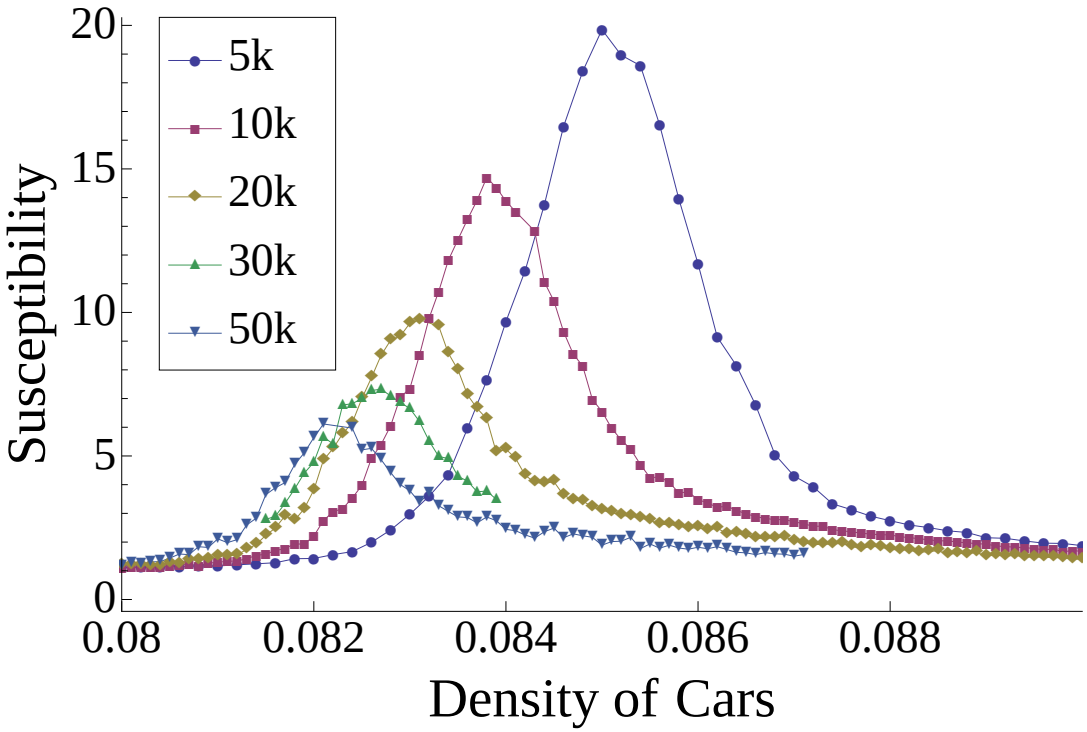

Figure 2.30: The dynamic susceptibility χ_4 for $V_{\max} = 9$, $p = 0.1$ and various system sizes.

2.5 Finite-Size Scaling

2.5.1 Optimized Method for Finite-Size Scaling

In order to examine the long range correlations in this transition, we use a finite-size scaling approach [30, 31, 29]. Accordingly, we assume that the order parameter x_0 near the transition point depends on the size of the system as:

$$x_0 = L^{-a_0} f(L/\xi)\,, \tag{2.23}$$

where a_0 is the scaling exponent, and ξ is the correlation length, which itself depends on L via

$$\xi \propto (d - d_c(L))^{-\nu}\,, \tag{2.24}$$

where $d_c(L)$ is the critical density.

In most finite-size scaling studies, the transition point itself is dependent on the system size. That effect is usually considered as a correction to scaling [29], and $d_c(L)$ then considered independent of L. We found that we got much better scaling fits by considering a length dependent critical density via

$$d_c(L) = d_0 + cL^{-b}\,, \tag{2.25}$$

where d_0 is the critical density for the infinite system.

To find the shift in the critical density, the typical approach [29] is to study a quantity like a susceptibility that has a peak at the transition. Figure 2.30 shows that χ_4 has such property. The order parameters we introduced have no maximum at the transition. While at first thought, a quantity like $\langle x_0^2 \rangle$ might act like a susceptibility, we have found that this jamming transition is not like an equilibrium transition with large fluctuations in the order parameter correlations before the transition. Instead, we see the nucleation of a different phase (the jams) in a background of the free phase, and the fluctuations in x_0 basically track

x_0. Therefore we study their derivatives [29] instead. Figure 2.31 shows how the derivatives of the regular order parameters we introduced in Section $Finite - Size\ Effects$ behave at the transition area. They have a maximum point which could be used as reference point for scaling purposes.

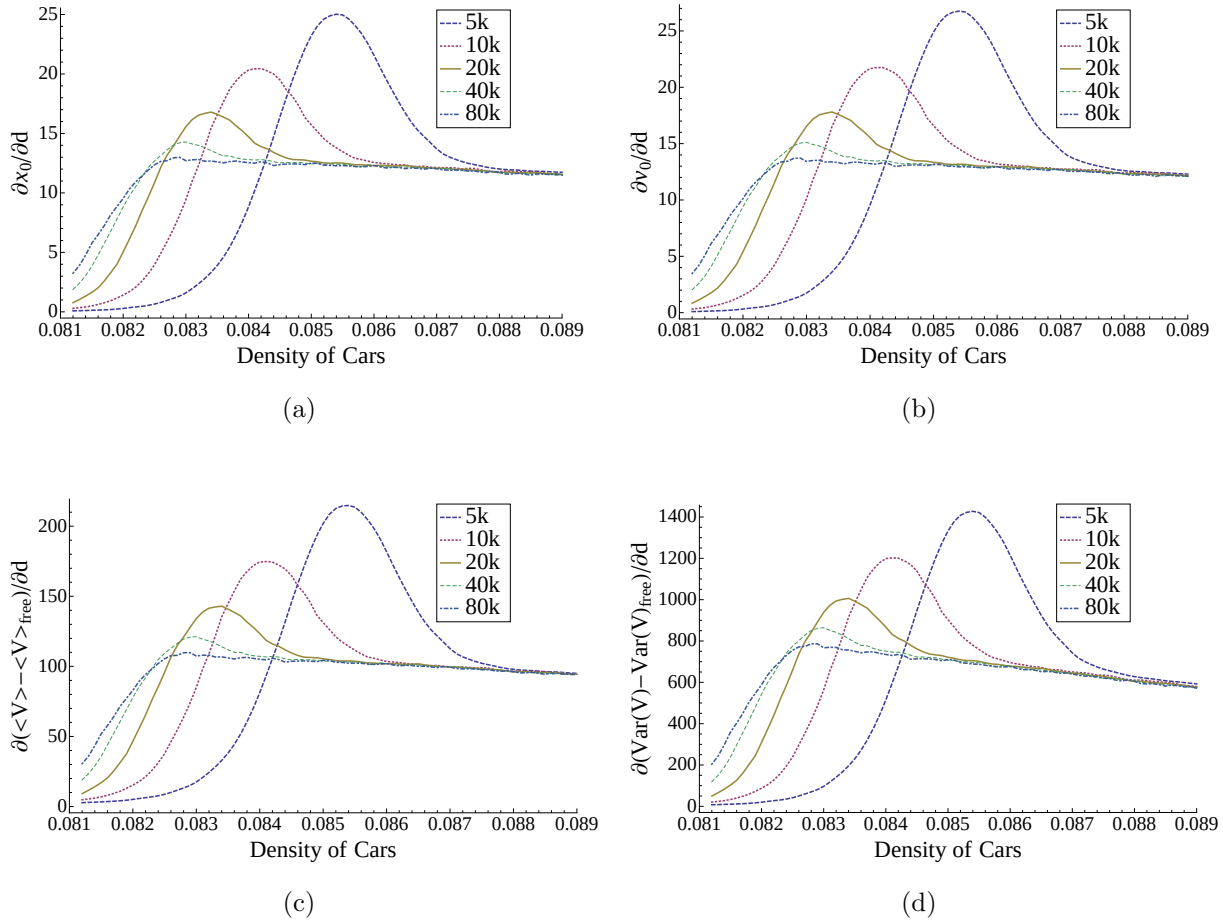

Figure 2.31: Derivatives of the order parameters (a) x_0, (b) v_0, (c) $\langle V\rangle - \langle V\rangle_{\text{free}}$ and (d) $\text{Var}(V)_{\text{free}}$ with respect to density around the transition area vs. the density, for the system with $V_{\max} = 9$, $p = 0.1$, and various track lengths. Plots show that they have a maximum which could be used as a reference point for scaling purposes.

The first step in our scaling process is to scale the density such that the transition happens at the origin (Equation 2.25). If we use the positions of the peaks to calculate the shift of the transition point, we find $d_0 = 0.08267 \pm 0.00001$, $c = 9.415 \pm 5.278$, and $b = 0.956 \pm 0.065$. Figure 2.32 shows how this scaling in density affects the position of the

peak in the corresponding order parameters. Figure 2.33 shows the original values of the order parameters vs. the scaled density $d_c(L)$.

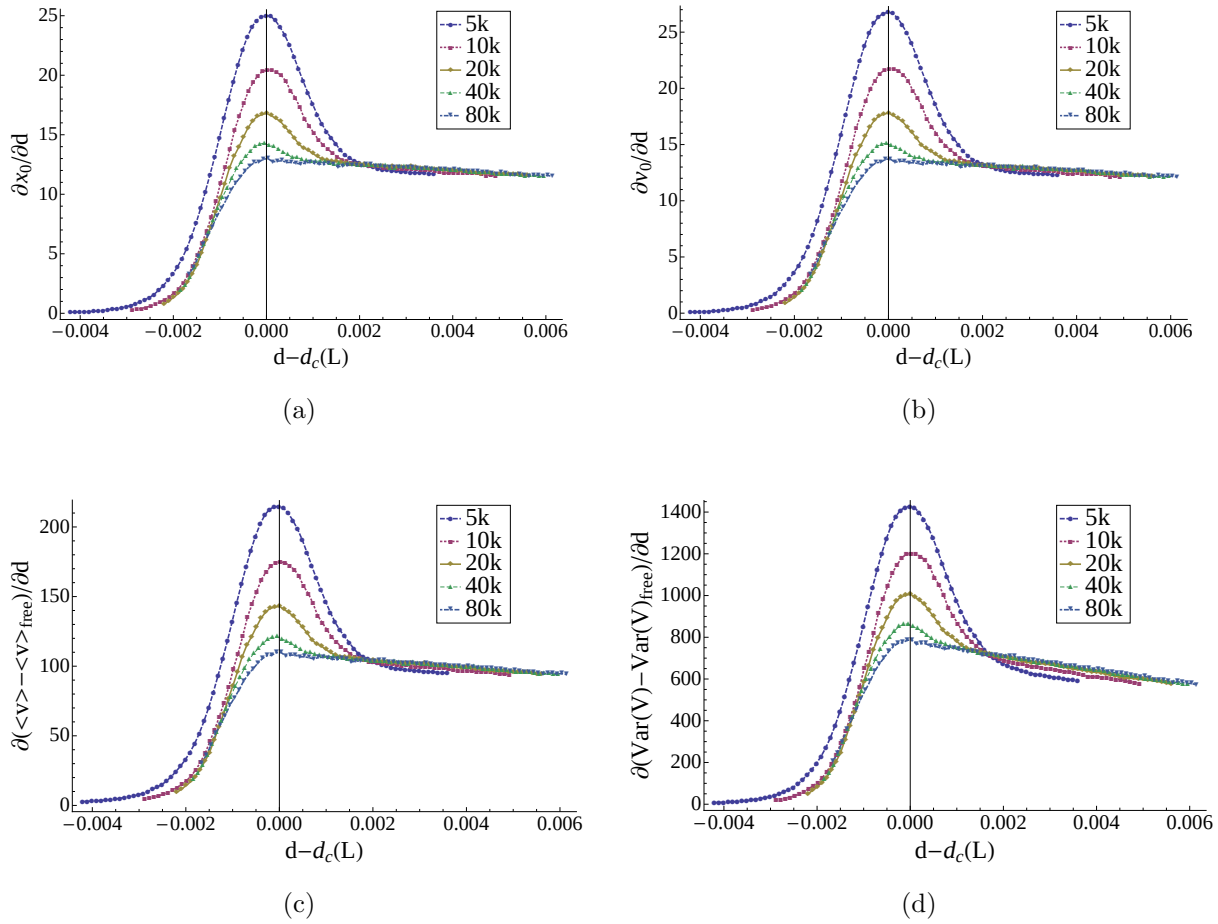

Figure 2.32: Derivatives of the order parameters (a) x_0, (b) v_0, (c) $\langle V\rangle - \langle V\rangle_{\text{free}}$, and (d) $\text{Var}(V) - \text{Var}(V)_{\text{free}}$ with respect to density around the transition area vs. the scaled density, for the system with $V_{\max} = 9$, $p = 0.1$, and various track lengths. Plots show that the maximum points are shifted to the origin of the scaled density $d_c(L)$ axis.

Second step is to scale the values of the order parameter at the reference points in order to put all the maximums on top of each others. This would be done by finding the amplitude exponent a in Equation 2.23. Table 2.1 and 2.2 show the fitted values for the amplitude exponent for different order parameters discussed. Figure 2.34 shows scaled amplitude of the order parameters (e.g. $x_0 L^a$) vs. the scaled density.

The last step in the scaling process is to find the correlation length exponent ν. After finding the shift in the transition and adjusting the height of reference points by determining

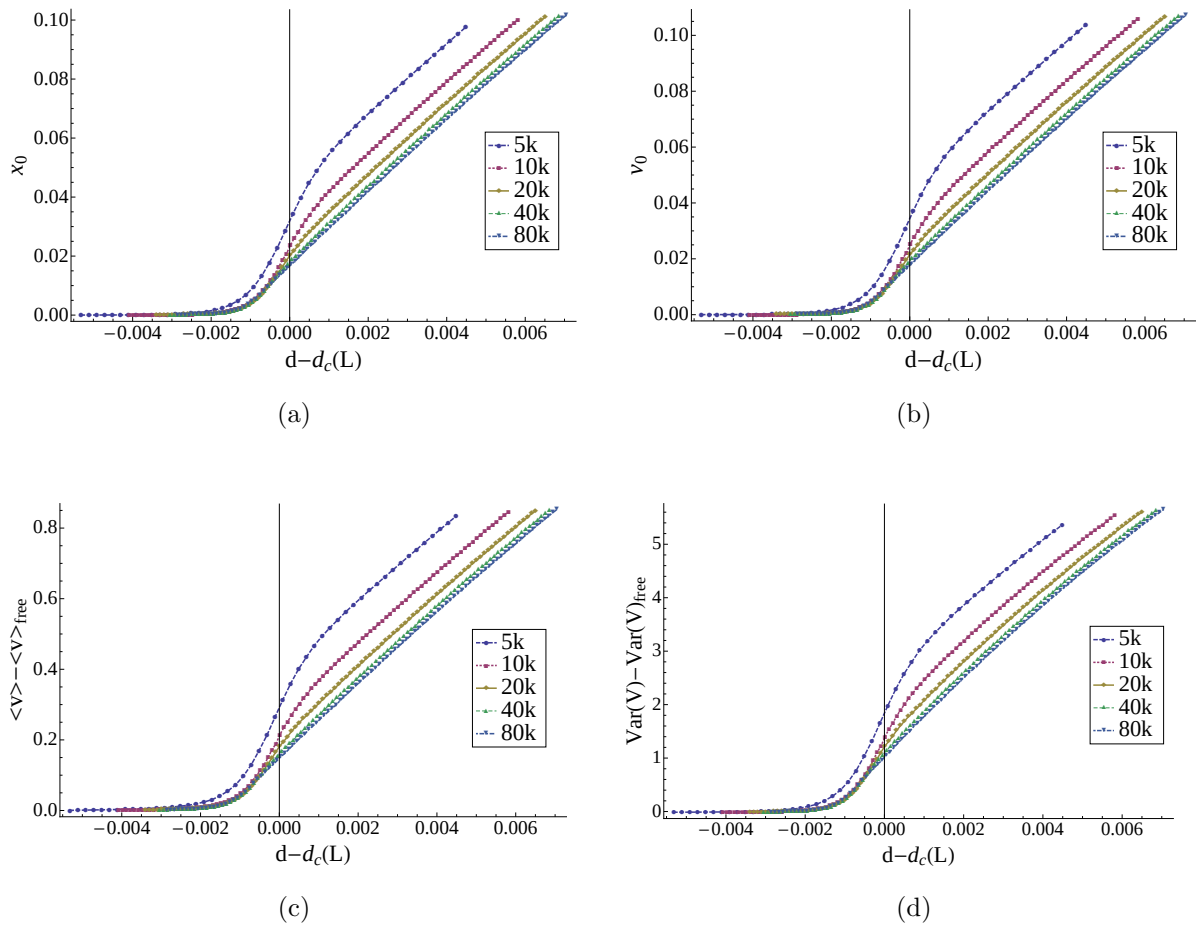

Figure 2.33: Order parameters (a) x_0, (b) v_0, (c) $\langle V\rangle - \langle V\rangle_{\text{free}}$, and (d) $\text{Var}(V) - \text{Var}(V)_{\text{free}}$ vs. the scaled density, for the system with $V_{\max} = 9$, $p = 0.1$, and various track lengths. Plots show that transition points are shifted to the origin of the scaled density $d_c(L)$ axis.

the amplitude exponent, we collapse the data onto a single curve by plotting the quantity versus $(d - d_c(L))L^{\nu}$ and adjust the exponents to minimize the area bounded by the scaled data. The scaled plots of the order parameter discussed above are shown in Figure 2.35.

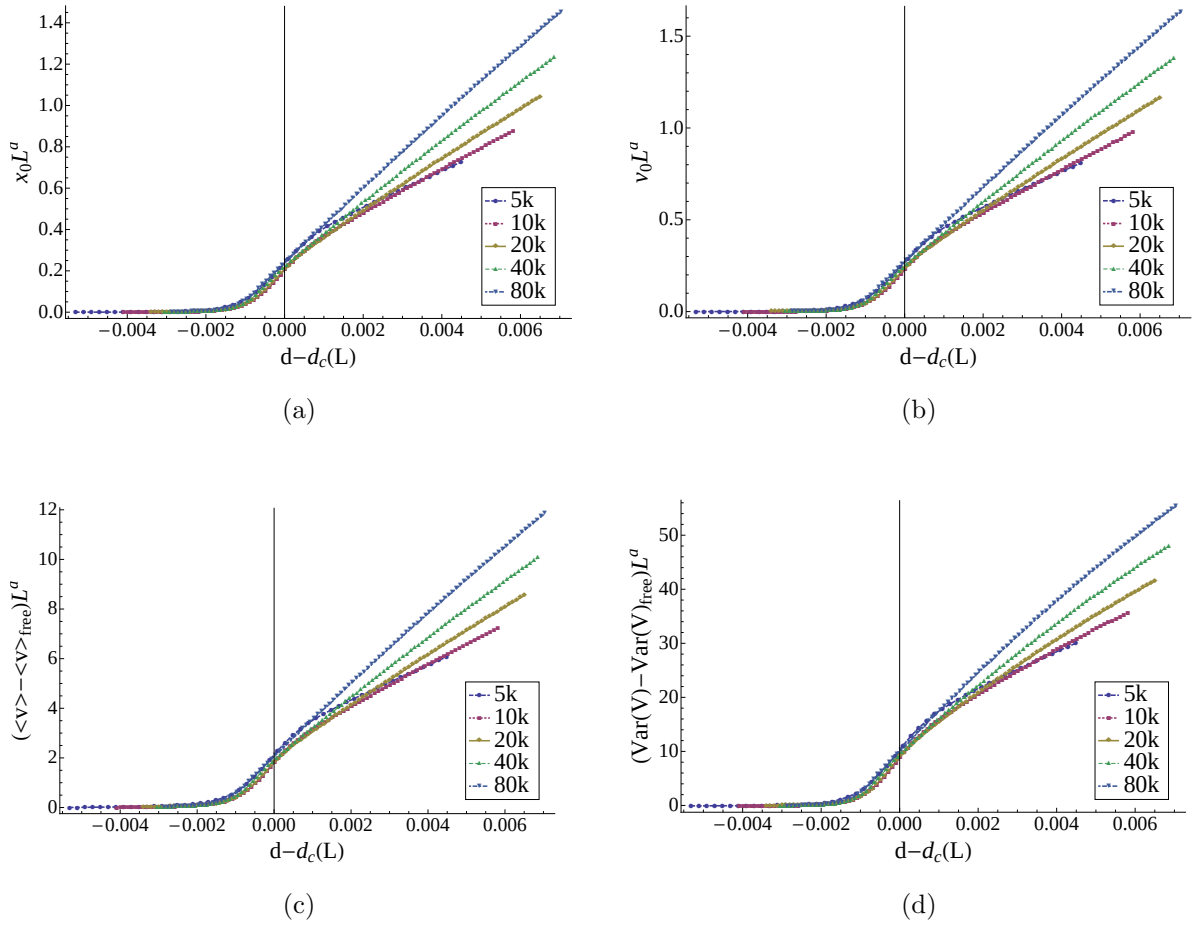

Figure 2.34: Scaled order parameters (a) x_0, (b) v_0, (c) $\langle V\rangle - \langle V\rangle_{\text{free}}$, and (d) $\text{Var}(V) - \text{Var}(V)_{\text{free}}$ vs. the scaled density, for the system with $V_{\max} = 9$, $p = 0.1$, and various track lengths. Plots show that transition points are shifted both on the scaled amplitude (i.e. amplitude $\times$ L^a) axis and the scaled density $d_c(L)$ axis in order to fit on top of each others.

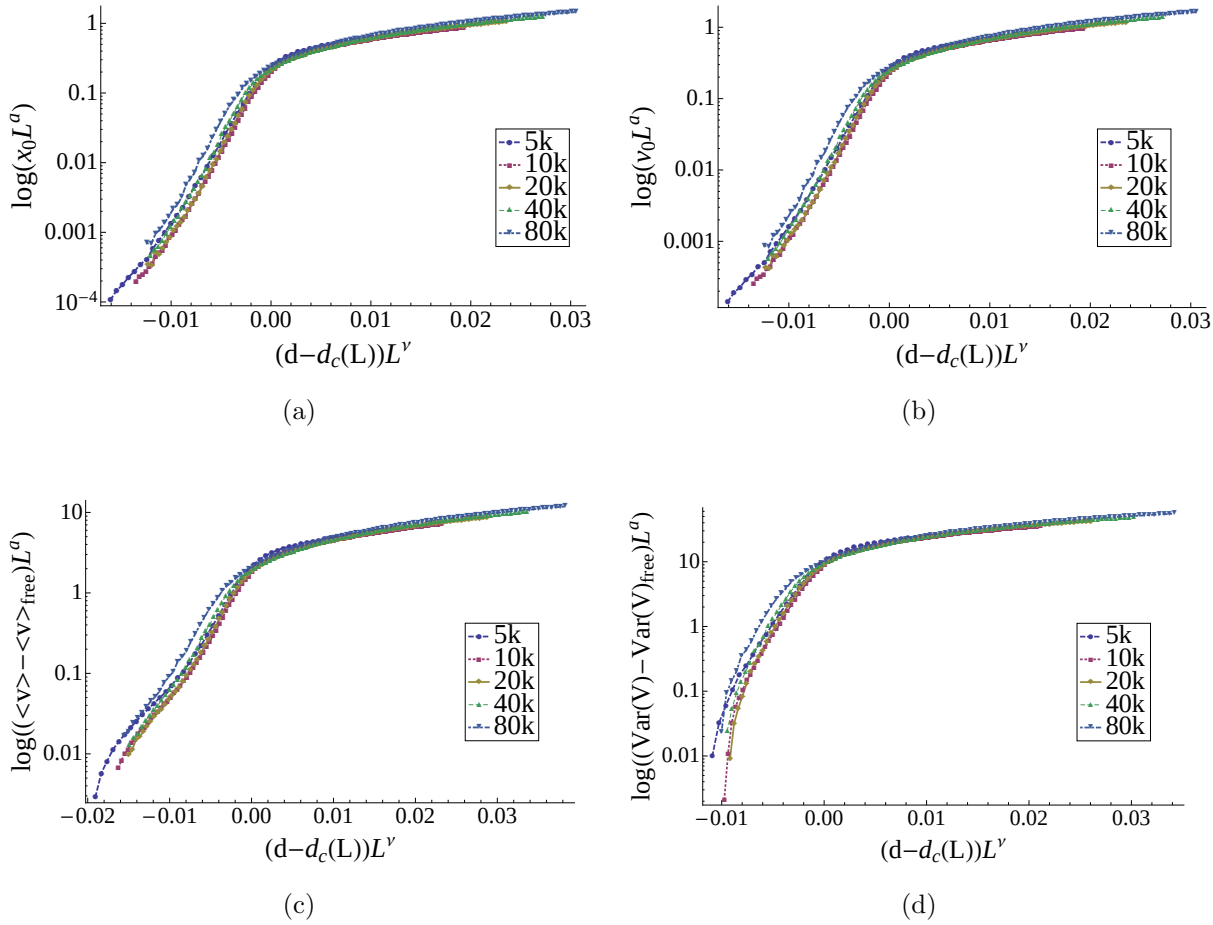

Figure 2.35: Logarithmic plot of the scaled order parameters (a) x_0, (b) v_0, (c) $\langle V\rangle - \langle V\rangle_{\text{free}}$, and (d) $\text{Var}(V) - \text{Var}(V)_{\text{free}}$ vs. the scaled density, for the system with $V_{\max} = 9$, $p = 0.1$, and various track lengths. Plots show that the scaled curves for different track lengths are collapsed when using the scaling exponents from Table2.1 and 2.2.

2.5.2 Critical Exponents of the Nagel-Schreckenberg Model

We assume χ_4 also obeys a finite-size scaling form:

$$\chi_4 = L^{-a_4} f(L/\xi)\,. \tag{2.26}$$

Using the peaks in χ_4 in Figure 2.38(a) as the reference points, we find the scaling relation for the critical density as well as the amplitude exponent. Figure 2.36 shows the fitted function for the position of the reference points. This fit allows us to accurately find the critical density. We find for $V_{\max} = 9$ and $p = 0.1$ that the bulk transition occurs at $d_0 = 0.08122 \pm 0.00004$. The shift in the transition due to the finite system size has an amplitude of $c = 0.375 \pm 0.006$ and a scaling exponent of $b = 0.54 \pm 0.02$. Figure 2.37 shows the fitted scaling function for the amplitude of the order parameter χ at its maximum for each size. We obtain the amplitude exponent a by finding the corresponding exponent in the power function. Figure 2.38 shows the steps of the scaling process for the susceptibility χ_4. There is no reason to expect that the peak in the derivative of x_0 should be at the same place as the χ_4 peak, so it is not surprising the two results for the shift in the transition point are different. No matter which method we use to determine the shift in the transition point, we find that x_0 and χ_4 produce values for the correlation length exponent ν of 0.13 ± 0.02 and 0.14 ± 0.02, respectively.

The scaling exponent for the amplitude of x_0 is $a_0 = 0.24 \pm 0.04$ and that of χ_4 is $a_4 = 0.52 \pm 0.02$. We also examined the scaling behavior of several alternative order parameters: the probability of a car having a speed $< V_{\max}/2$ [21], the difference between the mean speed and that of the free flow speed [23], and the difference between the variance in the velocity and its value in the free flow regime. All of them gave results for ν and the scaling amplitude exponent a_0 that were consistent with those found for x_0. The determined values for the scaling exponents for different order parameters are presented in Table 2.1 and 2.2.

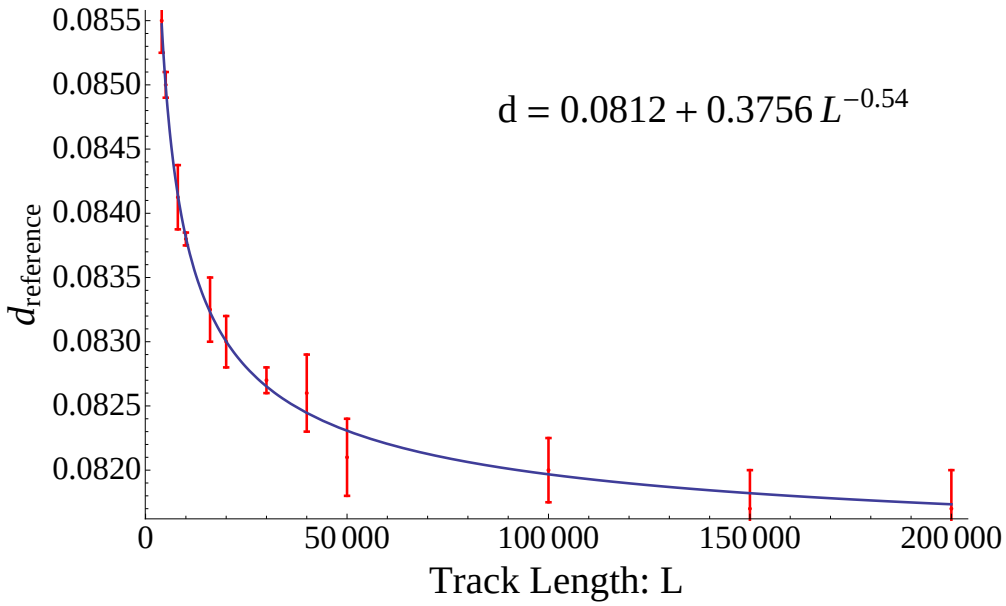

Figure 2.36: Fitted function for the position of the reference points in χ_4 vs. track length for systems with $V_{\max} = 9$ and $p = 0.1$. Parameters of this fit show the critical density d_0 for an infinitely large system as well as the length dependent correction in Equation 2.25.

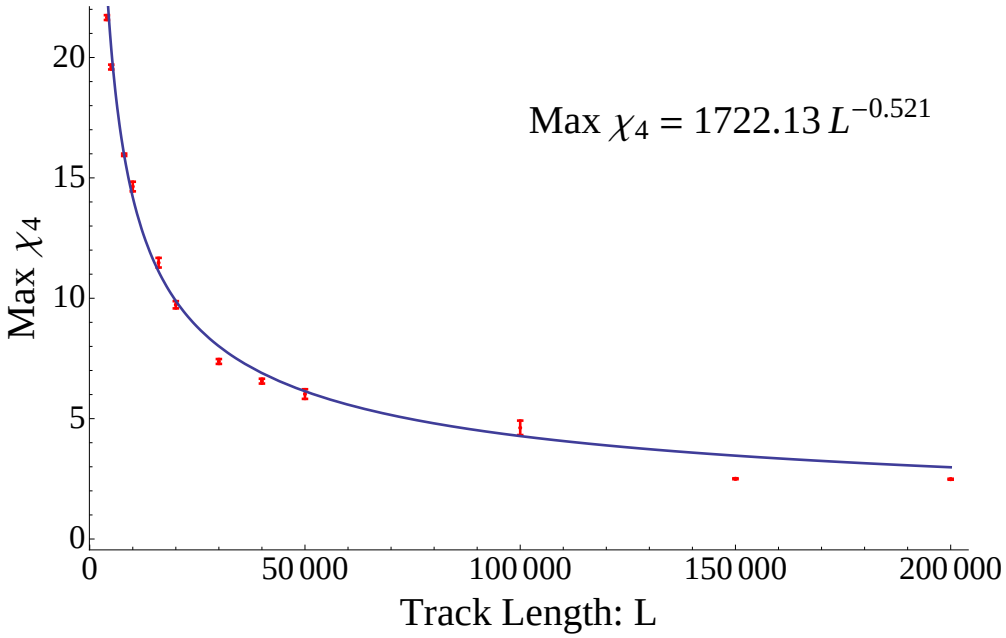

Figure 2.37: Fitted function for the values of the reference points in χ_4 vs. track length for systems with $V_{\max} = 9$ and $p = 0.1$. The obtained exponent in this fit is the amplitude exponent a for the corresponding order parameter (Equation 2.23).

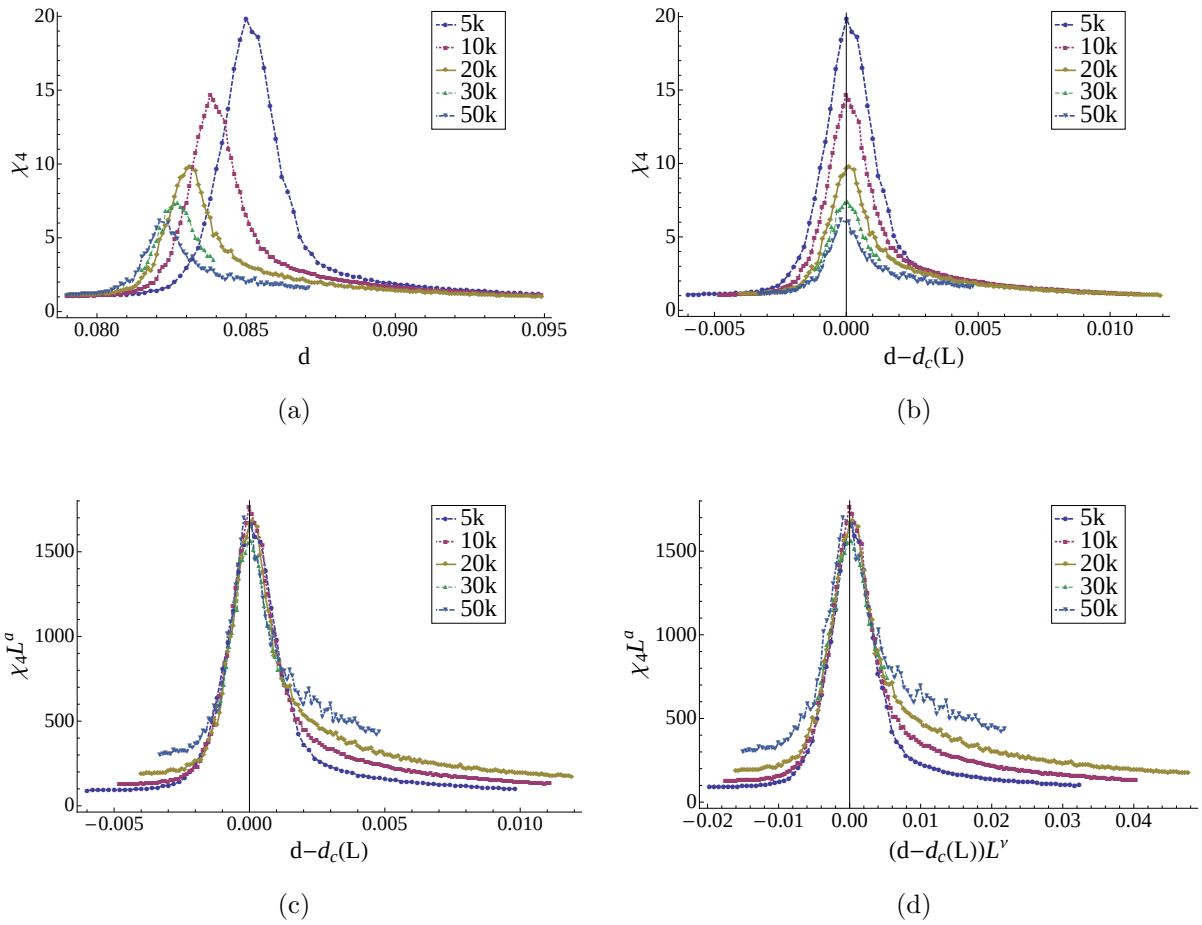

Figure 2.38: Finite-size scaling process for χ_4 in systems with $V_{\max} = 9$, $p = 0.1$, and various track lengths: (a) χ_4 vs. d, the original values of order parameter. (b) χ_4 vs. $d - d_c(L)$, step one, shifting the density to find the critical density d_0. (c) $\chi_4 L^a$ vs. $d - d_c(L)$, step two, scaling the amplitude of the maximum to find the amplitude exponent a. (d) $\chi_4 L^a$ vs. $(d - d_c(L))L^\nu$, final step, minimizing the area surrounded by the curves around the origin to collapse the curves and find the length correlation exponent ν. The value used for the critical exponents are the values represented in Table 2.1 and 2.2.

We have also determined the values of ν and the scaling exponents for the amplitude of x_0 and χ_4 for a range of values of $V_{\max}$ and p. The values of the exponents for different values of $V_{\max}$ and $p = 0.1$ are shown in Figure 2.39. The scaling behavior of χ_4 and x_0 both yielded values for ν that were statistically the same for $V_{\max} > 7$. For $V_{\max} = 6$ and $V_{\max} = 7$, the finite-size dependence was so weak that we could not get reliable values for the scaling amplitude of x_0, and we were only able to extract a value for ν from χ_4.

While this data does not imply a sharp change in the scaling behavior for $V_{\max} = 6$, it does indicate that the finite-size effects for $V_{\max} > 7$ are completely different than for $V_{\max} \leq 6$, which is already apparent in Figs. 2.19 and 2.21. Figure 2.39 clearly shows that the exponent ν appears to vanish or take on unphysical negative values for $V_{\max} = 5$ and 6, indicating that the long range correlations are absent below $V_{\max} = 7$.

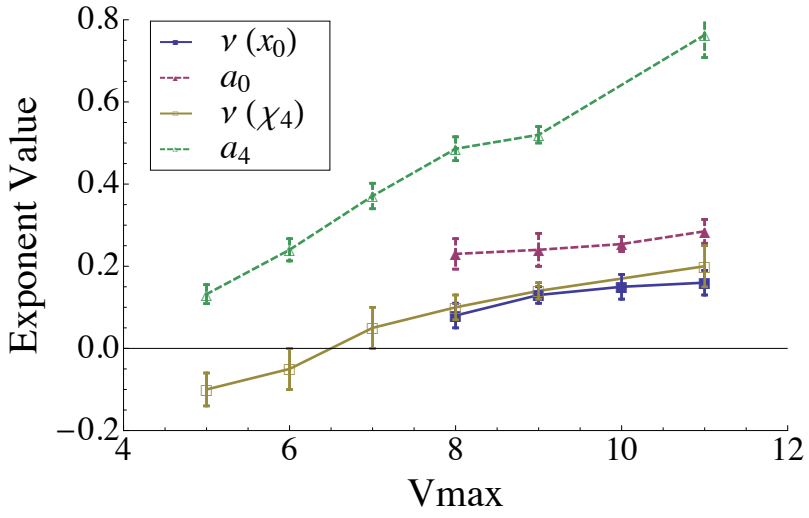

Figure 2.39: Exponents ν and a for various values of $V_{\max}$, with $p = 0.1$. The smaller error bars on $V_{\max} = 9$ result from using more track sizes.

Table 2.3 shows the scaling exponents for $V_{\max} = 9$ and three values of p, and we see no significant variation of ν or a_0 with p. We do not expect to observe any variation of the exponents for $0 < p < 1$, since the value of p controls the amount of stochastic behavior and the rate the system evolves through its configurations. Of course, in the special limits $p \to 0$ [24] and $p \to 1$ [26], glassy irreversible behavior is observed instead.

Table 2.1: Set of the critical density and coefficients for $V_{\max} = 9$ and $p = 0.1$. All the parameters have been fitted directly from the data with no degrees of freedom reduction. The critical density d_0 may differ depending on the type of the order parameter.

Parameter	d_0	c	b
x_0	0.08267 ± 0.00001	9.415 ± 5.278	-0.956 ± 0.068
v_0	0.08267 ± 0.00001	9.415 ± 5.278	-0.956 ± 0.068
$\langle V \rangle - \langle V \rangle_{\text{free}}$	0.08267 ± 0.00001	9.415 ± 5.278	-0.956 ± 0.068
$\text{Var}(V) - \text{Var}(V)_{\text{free}}$	0.08267 ± 0.00001	9.415 ± 5.278	-0.956 ± 0.068
χ_4	0.08122 ± 0.00004	0.375 ± 0.006	-0.54 ± 0.02

Table 2.2: Set of the exponents and coefficients for $V_{\max} = 9$ and $p = 0.1$. All the parameters have been fitted directly from the data with no degrees of freedom reduction. The main exponents ν and a remain unchanged no matter what method we use to find the other variables.

Parameter	ν	a
x_0	0.13 ± 0.01	0.2356 ± 0.0375
v_0	0.13 ± 0.01	0.2412 ± 0.0380
$\langle V \rangle - \langle V \rangle_{\text{free}}$	0.14 ± 0.01	0.2331 ± 0.0407
$\text{Var}(V) - \text{Var}(V)_{\text{free}}$	0.15 ± 0.01	0.2022 ± 0.0369
χ_4	0.14 ± 0.01	0.52 ± 0.02

2.5.3 Testing the Scaling Method on the 3d Ising Model

The Ising model is a well-known model commonly used in statistical physics. The transition in the Ising model has been studied widely. The study performed by Ferrenberg and Landau [29] on finite-size scaling corrections in 3d Ising model is known as one of the most accurate analyses on Ising model finite-size scaling. We have tested our approach on the 3d Ising model to compare the results with the values of finite-size scaling corrections in [29].

The Ising model is a set of up-down spins located at the discrete sites of the 3d lattice with size of $L \times L \times L$. The Hamiltonian of the system is defined as it follows:

$$H = -J\Sigma_{\langle i,j\rangle}\sigma_i\sigma_j, \tag{2.27}$$

where the spins σ_i can get the values of ± 1 and $\langle i, j\rangle$ means all the nearest neighbor pairs. Dimensionless coupling constant K is defined as $K = J/k_BT$. Therefore the dimensionless energy would be $E = \Sigma_{\langle i,j\rangle}\sigma_i\sigma_j$. The order parameters studied are listed as:

Magnetization:

$$|m| = L^{-d}\Sigma_i|\sigma_i| \tag{2.28}$$

Logarithm of magnetization:

$$\ln(|m|) = L^{-d}\Sigma_i ln(|\sigma_i|) \tag{2.29}$$

Logarithm of squared magnetization:

$$\ln(m^2) = L^{-d}\Sigma_i ln(\sigma_i^2) \tag{2.30}$$

Fourth-order magnetization cumulant:

$$U = 1 - \frac{\langle m^4\rangle}{3\langle m^2\rangle^2} \tag{2.31}$$

Table 2.3: Exponents ν and a_0 for $V_{\max} = 9$ and various values of p.

p	ν	a_0
0.1	0.13 ± 0.02	0.24 ± 0.04
0.2	0.12 ± 0.02	0.26 ± 0.04
0.5	0.14 ± 0.02	0.30 ± 0.01

Heat Capacity:

$$C = K^2 L^{-d}(\langle E^2 \rangle - \langle E \rangle^2) \tag{2.32}$$

Susceptibility:

$$\chi = kL^d(\langle |m|^2 \rangle - \langle |m| \rangle^2). \tag{2.33}$$

In Figure 2.40 we show the steps of applying our scaling method on the susceptibility χ which has maximum at the transition. In Figure 2.41 we have applied the scaling process on the derivative of the heat capacity $\partial C/\partial k$ to find the critical exponent for the heat capacity C. Figure 2.42 shows how fine this scaling method could collapse the magnetization ($|m|$) curves using the values in Table 2.4 as an example of the order parameter which does not have a maximum at the transition.

Table 2.4 shows the values we obtained from our analysis. Figure 2.43 indicates a method to find the critical temperature k_0 for an infinitely large system, using the finite-size scaling length correction method we introduced above. We have plotted the critical temperature for each order parameter at various system sizes versus the scaled system size. This plot shows that the fitted lines for all different order parameters point to the same density at the origin, which represents the critical temperature k_0 for an infinitely large system. We have found the critical temperature for the 3d Ising to be $k_0 = 0.221676 \pm 0.000007$. We find excellent agreement between our results and commonly accepted values for the 3d Ising mode critical temperature and scaling exponents reported in [29].

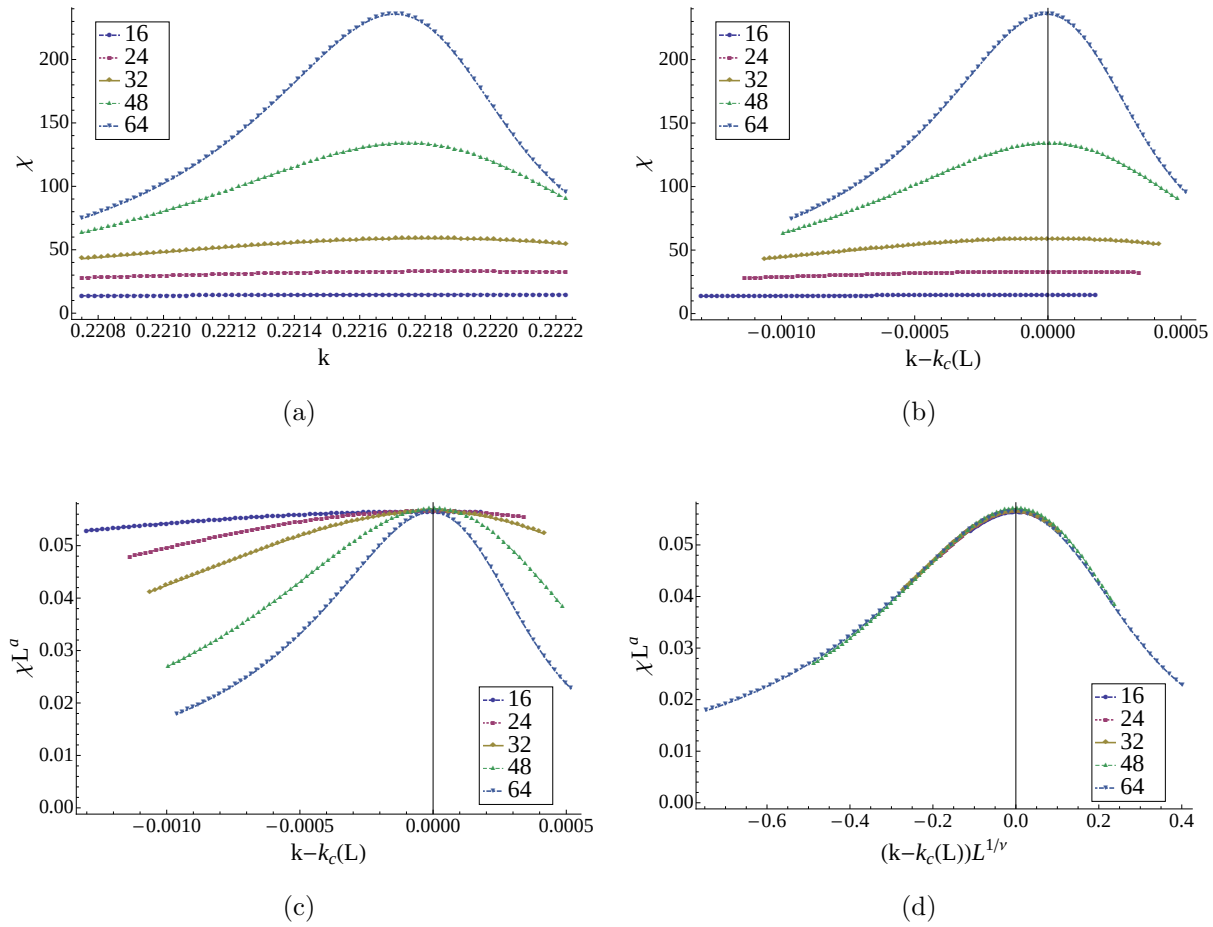

Figure 2.40: Finite-size scaling process for the susceptibility χ for 3d Ising model. The values used for the critical exponents are the values represented in Table 2.4. Subfigures (a), (b), (c), and (d) represent the original values, step one, step two, and the last step of the scaling process, respectively.

Table 2.4: Set of the critical exponents for the 3d Ising model using various order parameters. k_0 represents the critical dimensionless temperature using $k_c(L) = k_0 + cL^{-b}$, $1/\nu$ is the length correlation exponent using $\xi \propto (k - k_c(L))^{-1/\nu}$, and a represents the amplitude exponent in $x = L^{-a} f(L/\xi)$, where x is the corresponding order parameter.

Parameter	k_0	$1/\nu$	a
$\lvert m \rvert$	0.221574 ± 0.000011	-1.6051 ± 0.013	1.7 ± 0.05
$ln(m^2)$	0.221623 ± 0.000015	-1.6051 ± 0.011	1.7 ± 0.05
U	0.221666 ± 0.000063	-1.6108 ± 0.0231	1.65 ± 0.05
C	0.221722 ± 0.000051	-1.6055 ± 0.015	1.6 ± 0.05
χ	0.220795 ± 0.001804	-2.0049 ± 0.0089	1.6 ± 0.05

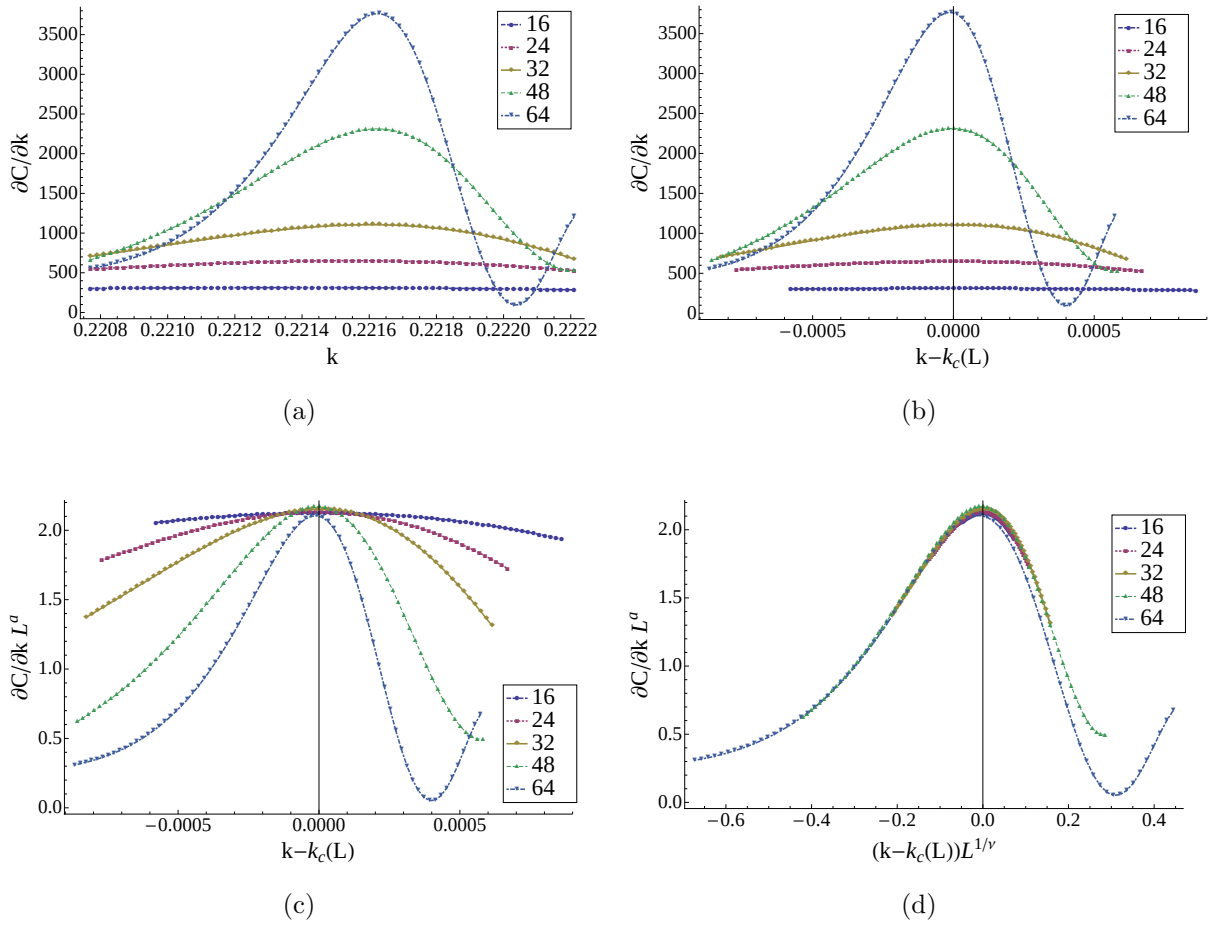

Figure 2.41: Finite-aize scaling process for the derivative of the heat capacity $\partial c/\partial k$ for 3d Ising model. The values used for the critical exponents are the values represented in Table 2.4. Subfigures (a), (b), (c), and (d) represent the original values, step one, step two, and the last step of the scaling process, respectively.

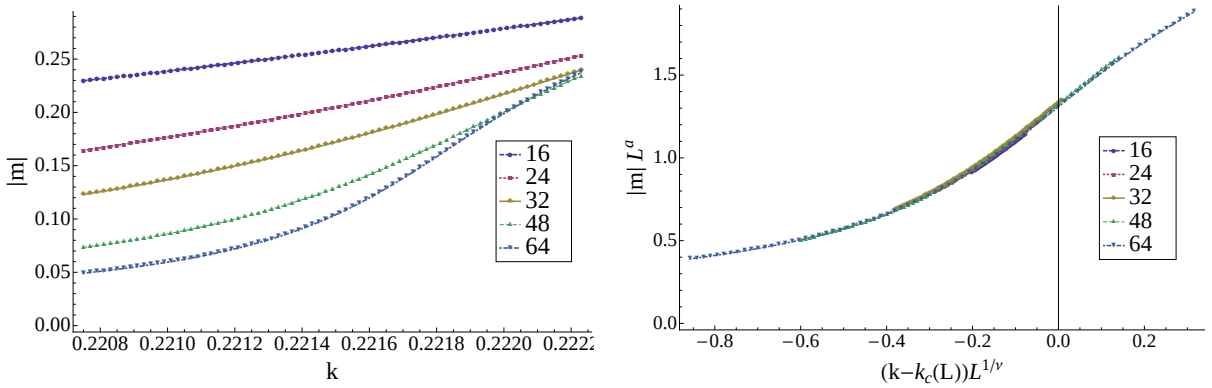

(a) (b)

Figure 2.42: Magnetization $|m|$ vs. dimensionless temperature for 3d Ising model. The values used for the critical exponents are the values represented in Table 2.4. Plot (a) shows the original values and plot (b) shows how well the values found for the critical exponents can collapse the plots of the magnetization for different lengths.

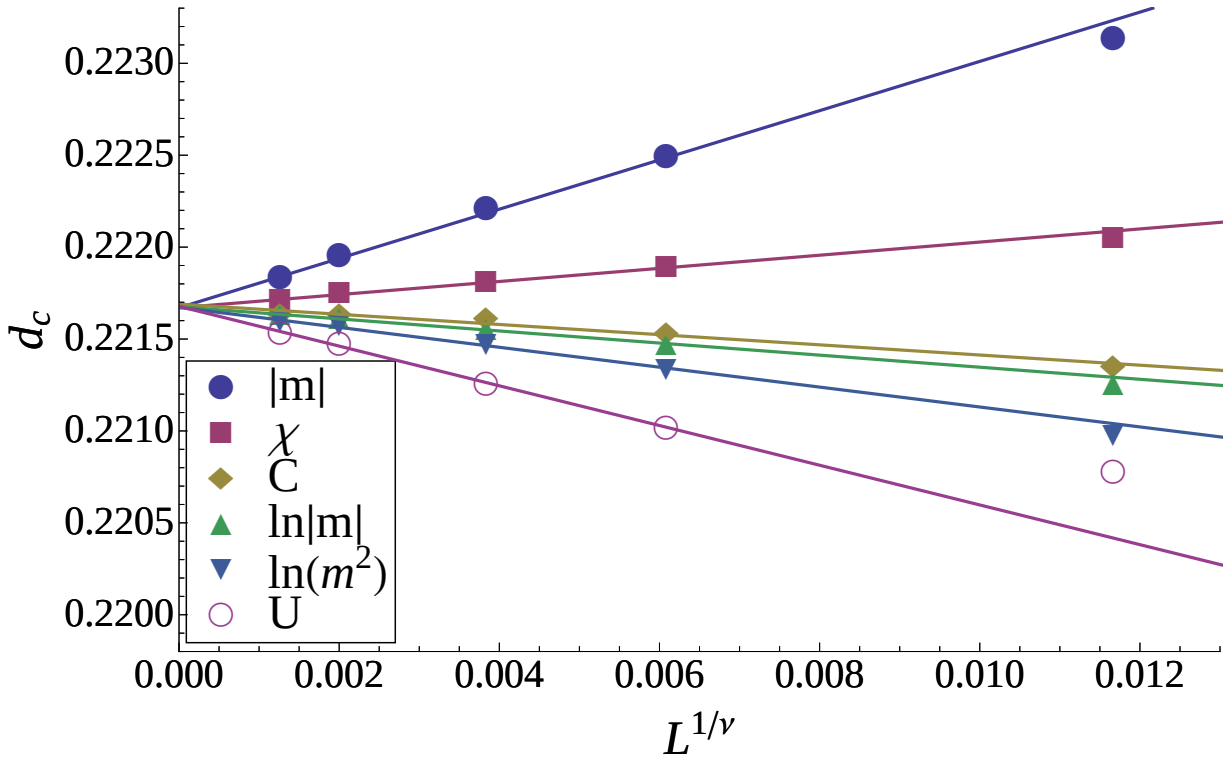

Figure 2.43: Critical dimensionless temperature vs. scaled system size for various order parameters in the 3d Ising model. All the fitted lines consistently point to the critical temperature for an infinitely large system.

2.6 Growth of the Jams

2.6.1 Braking Vehicles

As we noted in Section 2.1, there are several possible order parameters to study the phase transition in the NS model. We have studied many of these order parameters in Sections 2.4 and 2.5. In order to understand the nature of the finite-size effects at the transition, it is useful to study the number of cars affected by the *gap rule*. Being forced to brake to avoid a collision could be the initial step of forming the jams. The forced slow down applies whenever two vehicles are too close to each other. Figure 2.44 shows the probability of seeing at least one forced braking vehicle in the entire system at each time step. Although the probability that the *gap rule* being applied at least once does not show any size sensitivity for the system with $V_{\max} = 5$ (Figure 2.44(a)), it is clear that the finite-size effects exist for the system with $V_{\max} = 9$ (Figure 2.44(b)).

The next step is to check the probability that the *gap rule* is applied on at least two vehicles in the system at the same time. Figure 2.45(a) shows that it is still impossible to observe any size sensitive behavior in this parameter for the system with $V_{\max} = 5$. Figure 2.45(b) indicates the existence of finite-size behavior of this parameter for the system with $V_{\max} = 9$.

We further study the conditional probabilities to investigate the nature of size dependent behavior of the NS model in range of high values of $V_{\max}$. We are interested in the situations that the *gap rule* applies for the second time given that at least one forced slow down already exists. In other words, if we just select the time steps with at least one effective forced slow down (Figure 2.44), what percentage of those also include a second effective forced slow down (Figure 2.45). Figures 2.46(a) and 2.46(b) show that the same behavior is also observable for the systems with values of $V_{\max} = 5$ and 9, respectively. For future references (e.g. Section 2.6.5), note that at the transition area in Figure 2.46(b) (e.g. d=0.085), it is clear that the

probability of having the second forced slow down is much less for the systems with shorter lengths than that for the systems with longer lengths.

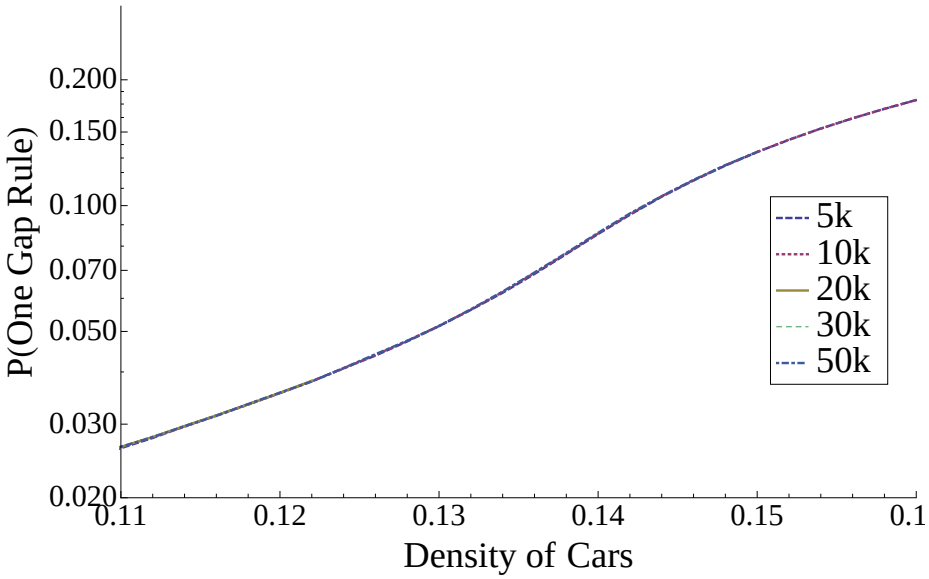

(a)

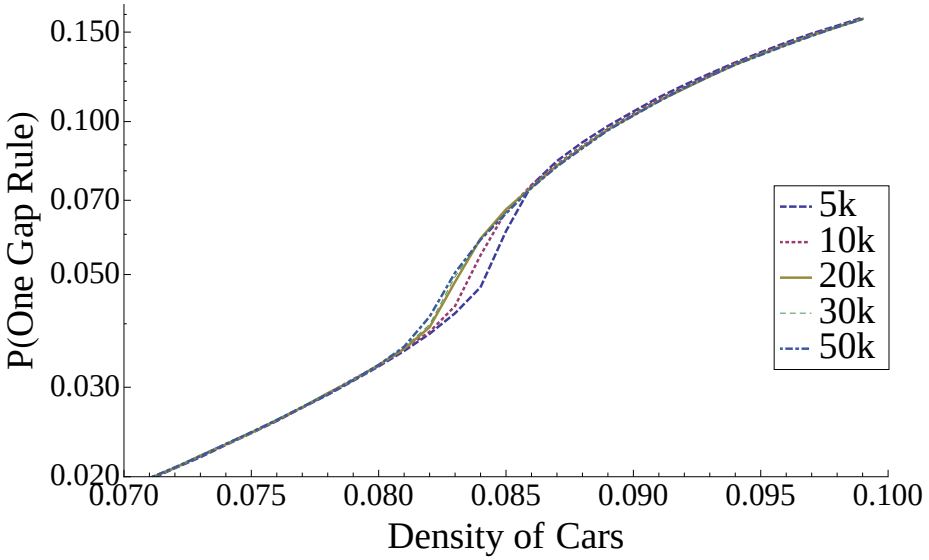

(b)

Figure 2.44: Probability of having at least one vehicle brake at each time step as a result of the *gap rule* vs. density of the vehicles for a system with $p = 0.1$, and (a) $V_{\max} = 5$ and (b) $V_{\max} = 9$. Plots show that while there is no finite-size effect observable for the system with $V_{\max} = 5$, same finite-size effect as the other order parameters exist for the system with $V_{\max} = 9$.

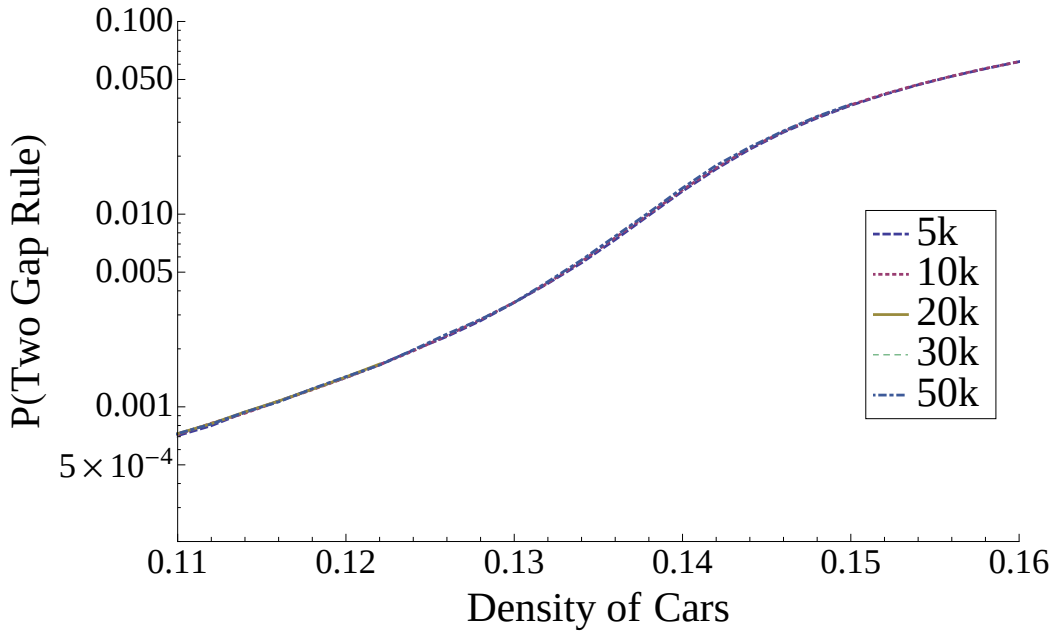

(a)

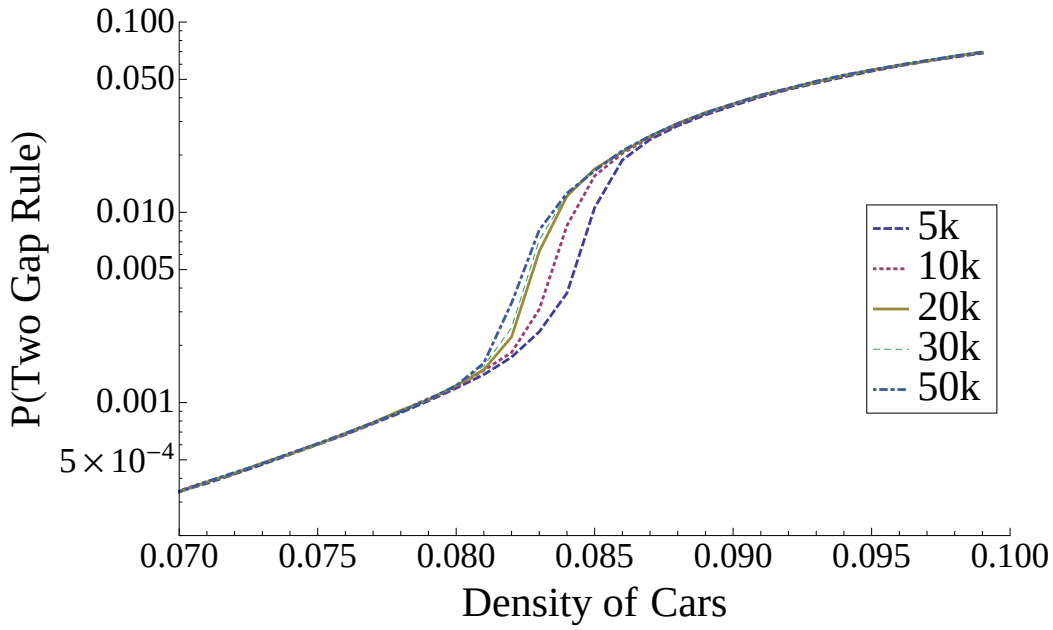

(b)

Figure 2.45: Probability of having at least two vehicles brake at each time step as a result of the *gap rule* vs. density of the vehicles for a system with $p = 0.1$, and (a) $V_{\max} = 5$ and (b) $V_{\max} = 9$. Plots show that while there is no finite-size effect observable for the system with $V_{\max} = 5$, same finite-size effect as the other order parameters exist for the system with $V_{\max} = 9$.

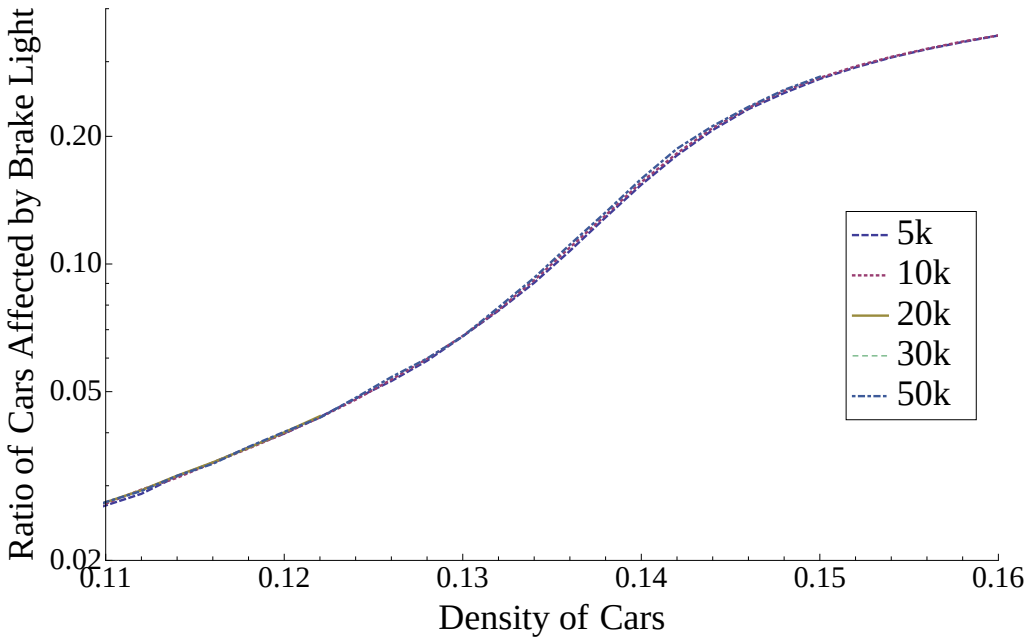

(a)

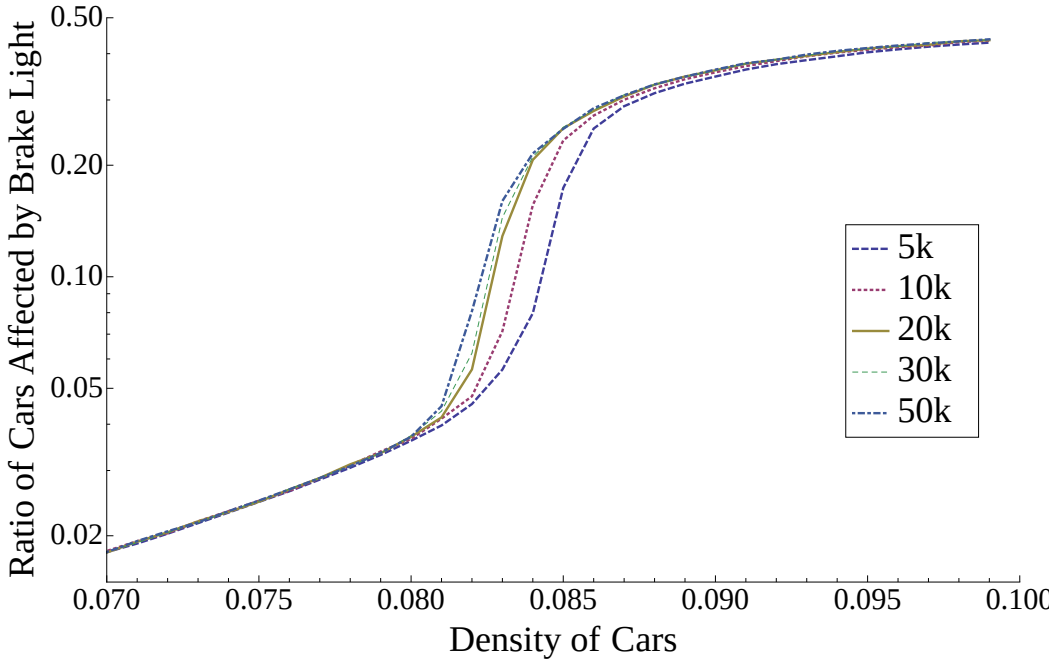

(b)

Figure 2.46: Conditional probability of at least two vehicles brake at each time step as a result of the *gap rule*, given that at least one forced slow down already happened in the system vs. density of the vehicles for a system with $p = 0.1$, and (a) $V_{\max} = 5$ and (b) $V_{\max} = 9$. Plots show that while there is no finite-size effect observable for the system with $V_{\max} = 5$, same finite-size effects as the other order parameters exist for the system with $V_{\max} = 9$.

2.6.2 Spatial Correlations of Jams

As we noted earlier in Figure 2.18, the finite-size effects that appear at the transition are accompanied by an upturn in the structure factor $S(q)$ for small q. It is therefore tempting to see whether the upturn in $S(q)$ merely reflects long range spatial correlations in x_0. We therefore define a local density $n_0(r)$ which is 1 if a vehicle is at site r and the gap to the next car ahead is less than $V_{\max}/2$. The extensive quantity $N_0 = \sum_r n_0(r) \equiv x_0 N$ provides a measure of the number of cars participating in a jam.

To study the spatial correlations in $n_0(r)$, we examine the static structure factor

$$S_0(q) = \langle |\rho_0(q)|^2 \rangle \tag{2.34}$$

$$\rho_0(q) = \sum_r n_0(r) e^{-iqr} \, . \tag{2.35}$$

In Figure 2.47 we show the magnitude of $S(q)$ and $S_0(q)$ at small values of q for a several densities spanning the transition to jamming for $V_{\max} = 9$ and $p = 0.1$. We see that most of the upturn in $S(q)$ for small q in the transition to jamming comes from correlations in $n_0(r)$ of order less than a hundred lattice spacings or so. The behavior for $V_{\max} = 5$ is similar, except that the width of the peak in $S_0(q)$ (and $S(q)$) is much wider, indicating that the jammed regions are significantly smaller at low $V_{\max}$. This behavior is also visible in Figure 2.48, where we display the variation of $S(q)$ and $S_0(q)$ with density for the longest wavelength $q = 2\pi/L$ in our simulation. The behavior for $V_{\max} = 5$, shown in Figure 2.48(b) is very similar to that seen for $V_{\max} = 9$, so we can conclude that the upturn in $S(q)$ in the transition region is due to long-range correlations in $n_0(r)$. This is surprising, since we did not see finite-size effects for $V_{\max} = 5$. We will see in the next section that it is the dynamics and statistics of the jams that is different for the two situations.

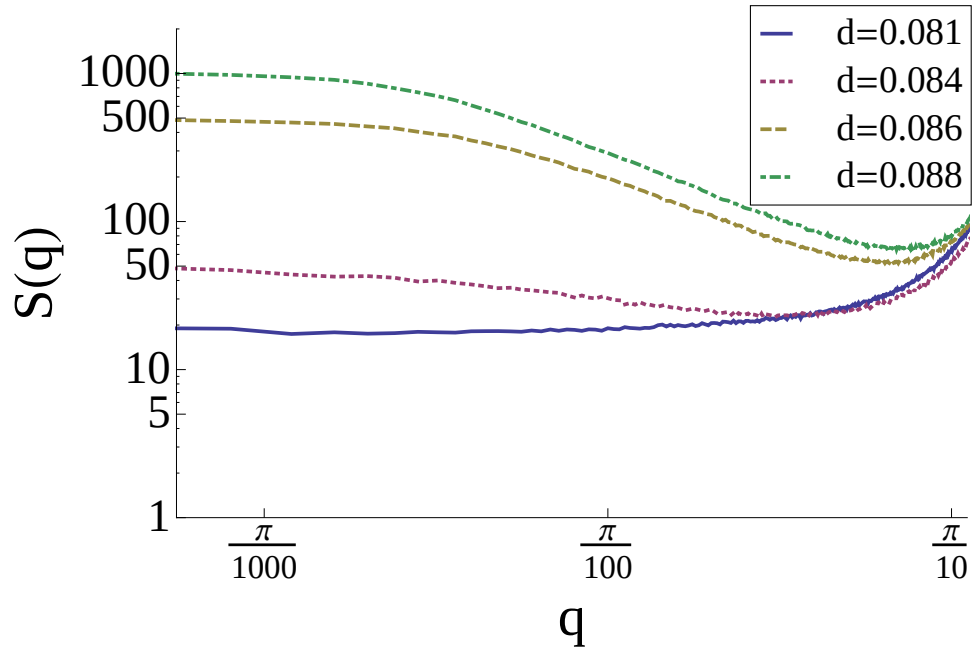

(a)

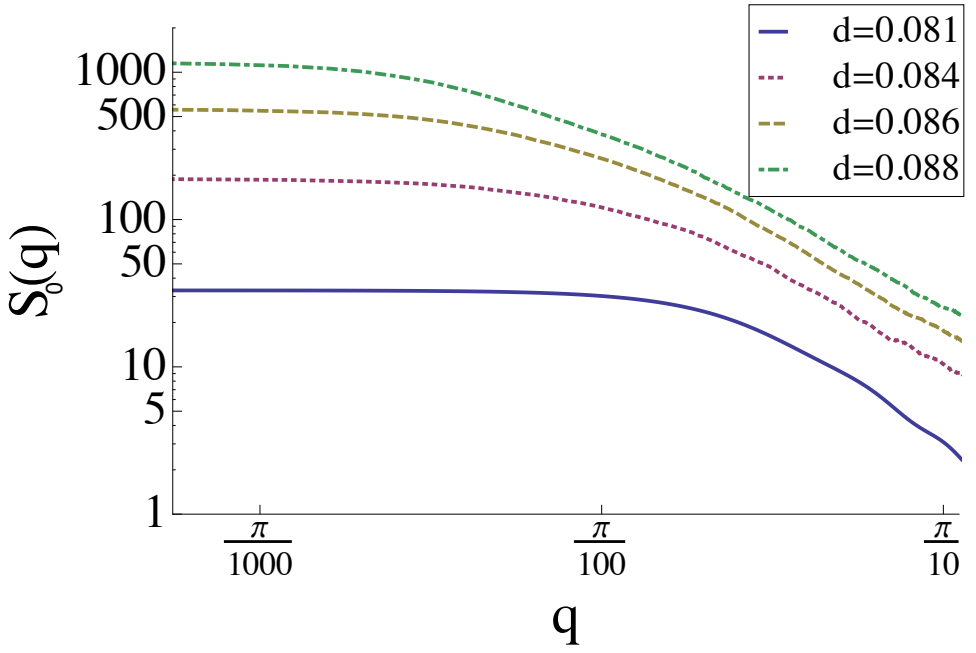

(b)

Figure 2.47: Behavior of (a) the total structure factor $S(q)$ and (b) the structure factor for jammed vehicles $S_0(q)$ for small q. The data are for $V_{\max} = 9$, $p = 0.1$ and $L = 5000$. The densities correspond to before the transition, in the transition region, and beyond the transition.

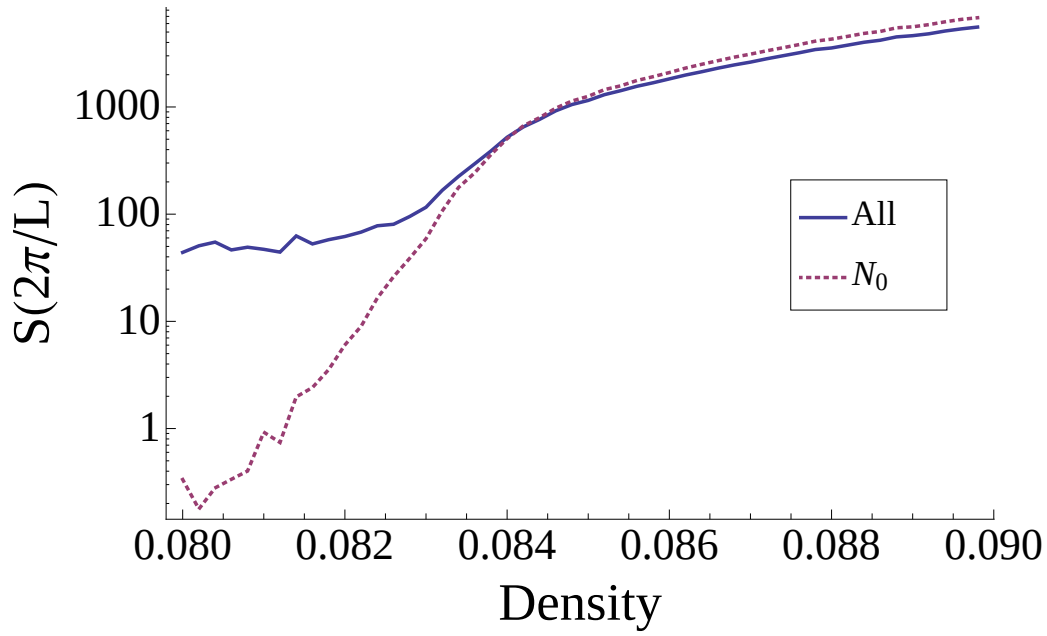

(a)

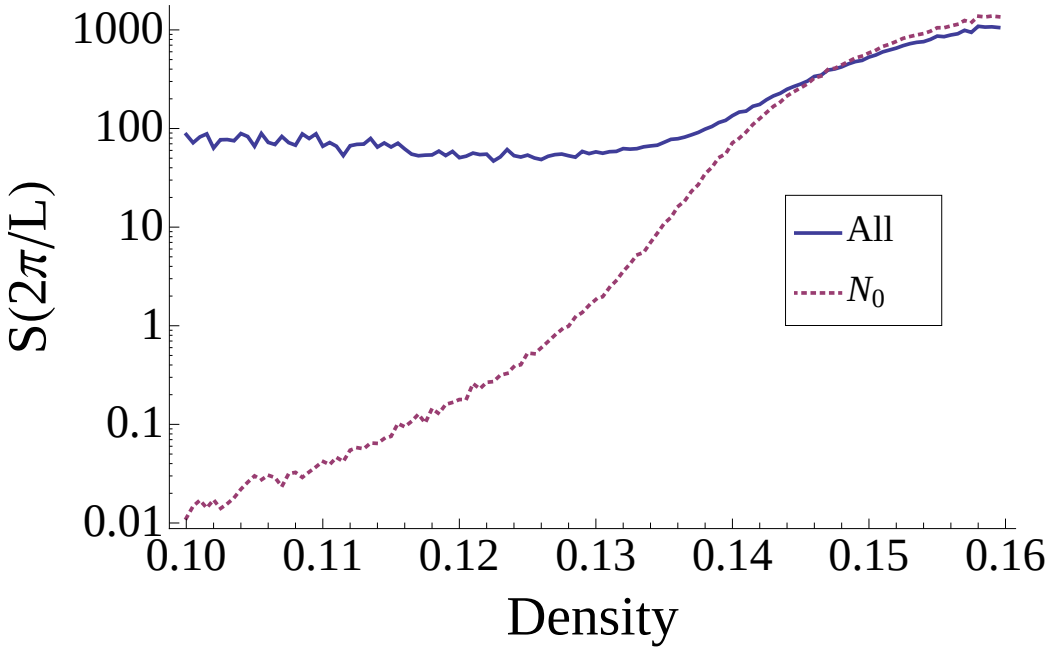

(b)

Figure 2.48: Behavior of $S(q{=}2\pi/L)$ and $S_0(q{=}2\pi/L)$ for $L = 10000$. (a) $V_{\max} = 9$ and (b) $V_{\max} = 5$, both with $p = 0.1$.

2.6.3 Jam Dynamics

To explore the difference between the low $V_{\max}$ and high $V_{\max}$ behavior, we looked at the time evolution of system at the transition area. Figure 2.49 shows how $N_0(t)$ behaves for different densities for $V_{\max} = 9$ and $V_{\max} = 5$. The densities shown are chosen so that the system is initially in the pure free-flow phase, then early in the transition region near the peak flux from Fig 2.21, then late in the transition region, and finally in the jam phase. In the free flow phase, we see isolated fluctuations into the jam phase very rarely for $V_{\max} = 9$, while these fluctuations are more frequent in the $V_{\max} = 5$ simulations. In the transition region close to the peak in the flux shown in Figure 2.21, the $V_{\max} = 9$ simulations still show isolated bursts of appearance of the jam phase, while for $V_{\max} = 5$ the number of jammed vehicles is fluctuating but always nonzero.

Since our order parameter x_0 for small $V_{\max}$ might be showing this behavior due to an inability to cleanly separate freely flowing vehicles from jammed vehicles, we also tried an order parameter that examines second neighbor correlations. Instead of merely asking that the car ahead be closer than $V_{\max}/2$, we ask that the spacing to the second car ahead be less than $V_{\max}$

$$\phi(r) = \begin{cases} 1 & r_n = r \text{ and } |r_{n+2} - r_n| < V_{\max} \\ 0 & \text{otherwise} \ , \end{cases}$$

and the total number of cars with this condition is $\Phi_0 = \sum_r \phi_(r)$.

We show in Figure 2.50 the fraction of the time the two order parameters are nonzero for $V_{\max} = 5$ and $V_{\max} = 9$. For $V_{\max} = 5$ both order parameters are always nonzero after $d = 0.115$, but that is actually a density before the peak flux in Figure 2.21 occurs for $V_{\max} = 5$, so the two order parameters become identical before the transition to jams occurs. For $V_{\max} = 9$, the two order parameters coincide and the transition from nearly zero to unity is the density range where we see finite-size effects. So improving our definition of a jammed vehicle does not change the conclusion that the nucleation of the jams for $V_{\max} \lesssim 6$ is qualitatively different than those for $V_{\max} \gtrsim 7$.

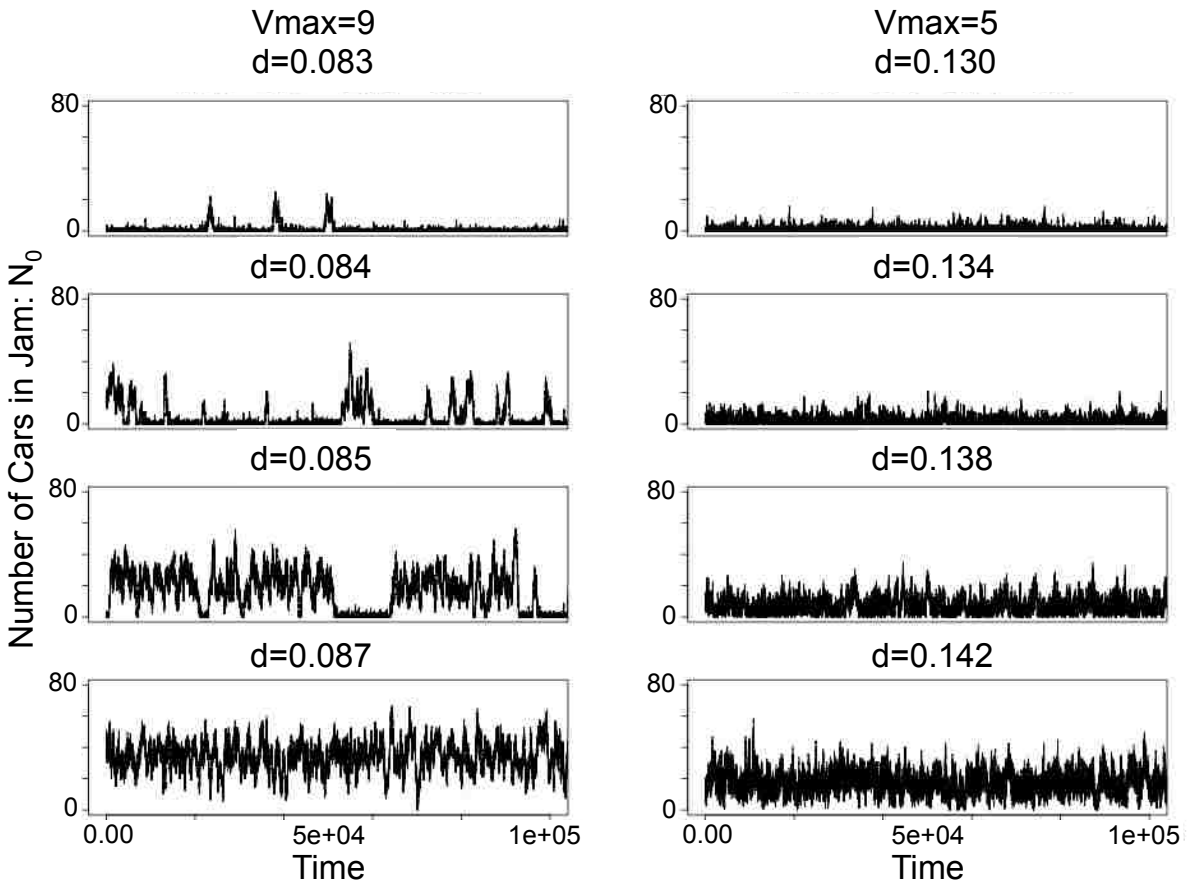

Figure 2.49: Time evolution of the number of cars in jam N_0 for a track of length 5,000 for $V_{\max} = 9$ (left) and $V_{\max} = 5$ (right) and $p = 0.1$.

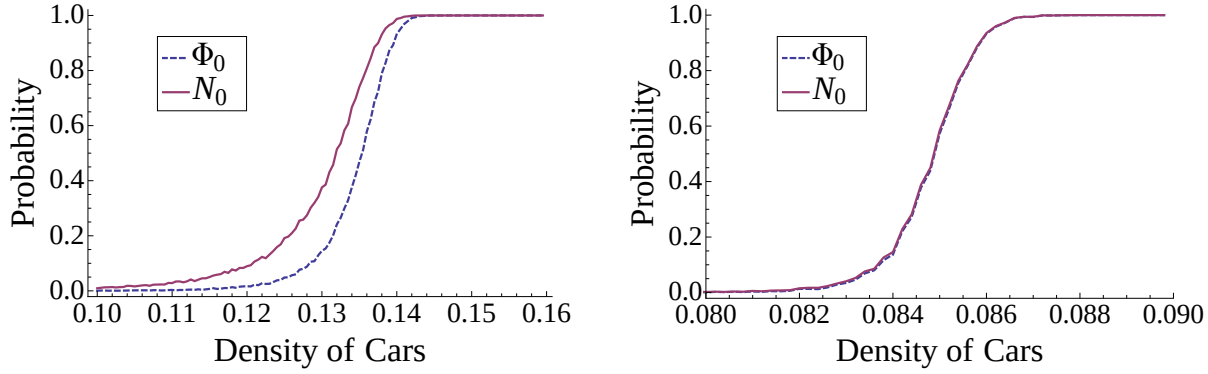

(a) (b)

Figure 2.50: Fraction of the time that the two order parameters N_0 and Φ_0 are nonzero for different densities for (a) $V_{\max} = 5$ and (b) $V_{\max} = 9$.

The difference in behavior for different $V_{\max}$ is also clearly visible in histograms of the fraction of the cars in a jam, Φ_0/N. Figure 2.51 shows the histograms for the same simulations shown in Figure 2.49. The peak at $\Phi_0/N = 0$ is the vehicles in the free-flow phase. While the distributions for the free flow regime at low density and the jammed regime are similar for both values of $V_{\max}$, they are clearly different in the transition regime. For $V_{\max} = 9$ the jam phase appears as a distinct phase in the transition region, while for $V_{\max} = 5$ this does not happen, with the distribution of jammed cars growing smoothly out of the free-flow phase.

Figure 2.52 shows how the length of the track affects themselves in the time evolution Φ_0 and in the distribution of Φ_0. The density in all of the plots is the same, but the histogram and the time evolution for the shortest track is characteristic of the free phase regime. For the intermediate track length, the behavior is that of two-phase coexistence. The longest track length data show it to be in the jam phase. Therefore we see that shorter track lengths inhibit the transition to jamming and thus we expect to see finite-size effects.

The transition region at high $V_{\max}$ can thus be thought of as a coexistence of cars condensed into jams and cars flowing freely. The appearance of a single localized jam will reduce the density of freely flowing cars elsewhere, and this effect is more significant for shorter tracks. Since the probability of creating a jammed region drops as the density of freely flowing cars goes down, the appearance of one jam inhibits the appearance of an additional one, stabilizing the dilute gas of jams.

This picture favors a fewer large jams rather many small jams. Figure 2.53 shows a histogram of the number of jams for $V_{\max} = 9$ at a density $d = 0.084$, and also the distribution of jam lengths. The distribution is not Poisson, as we would expect for independent events. Instead, we see a marked tendency for one or two large jams, with the probability of three or more jams greatly reduced. We find that the jam would be of order 50 sites in length, in agreement with the width of $S_0(q)$ for small q seen in Figure 2.47.

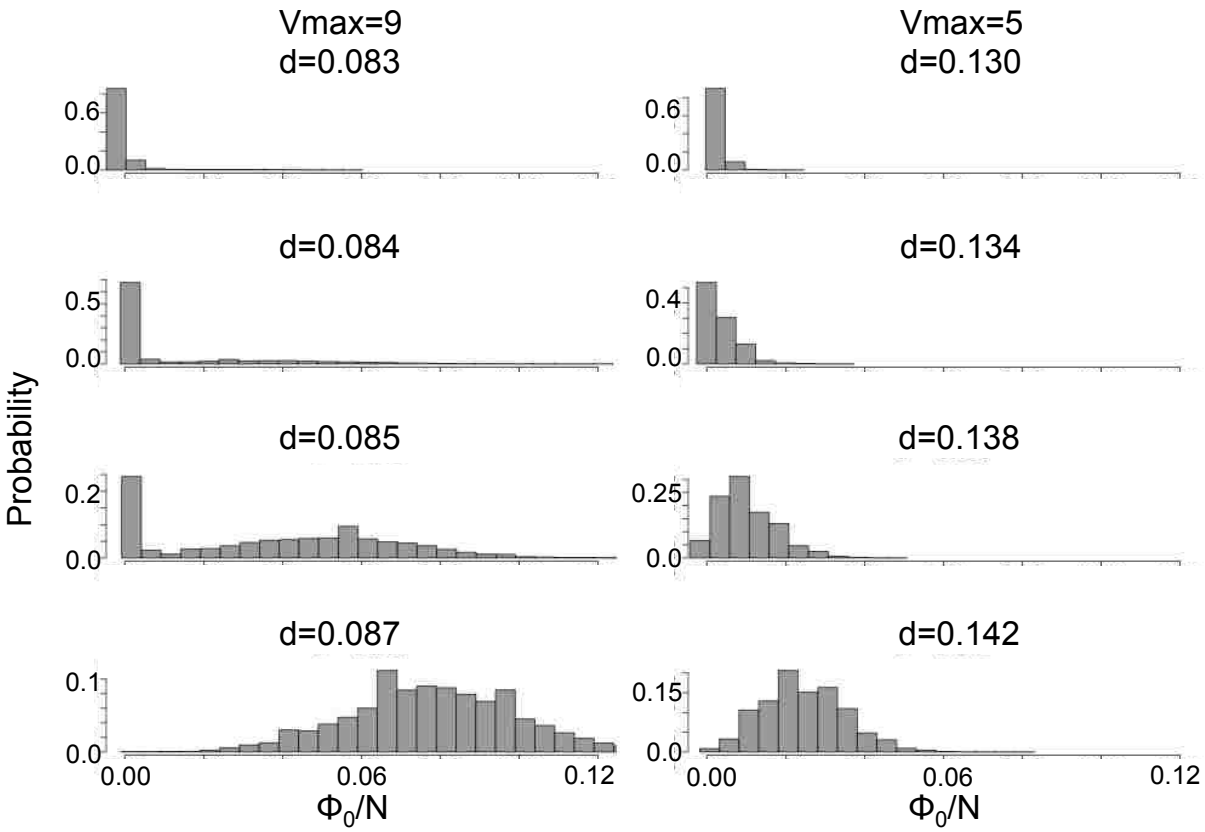

Figure 2.51: Histogram of Φ_0/N for the simulations show in Figure 2.49.

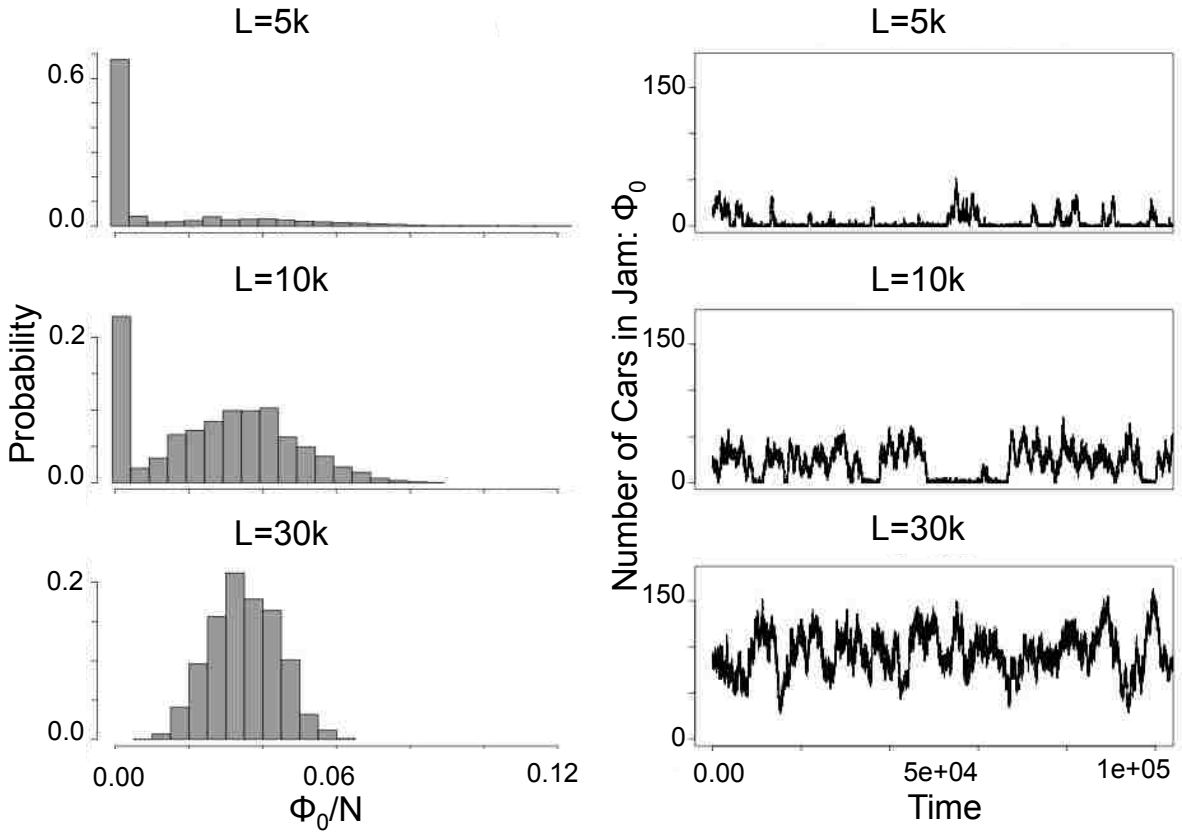

Figure 2.52: Time evolution and histogram of Φ_0/N for systems with same density $d = 0.084$ and different lengths.

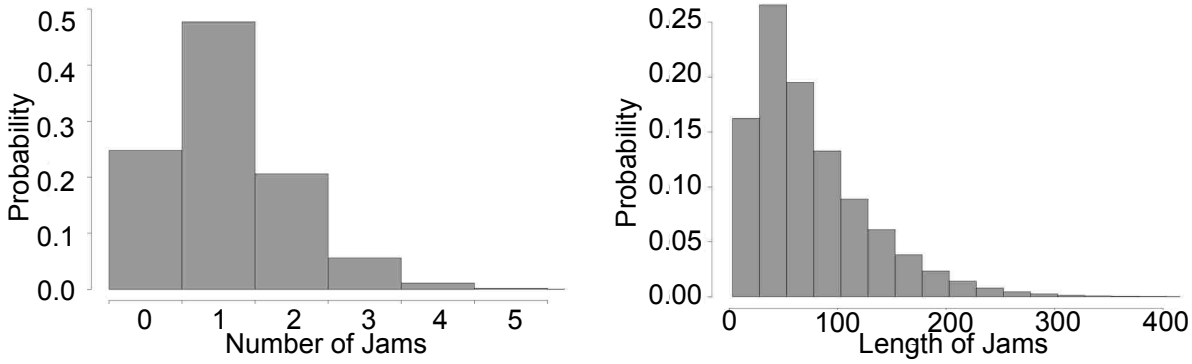

(a) (b)

Figure 2.53: Statistics for 200,000 samples in a system of size $L = 10,000$ for $V_{\max} = 9$, $p = 0.1$ and $d = 0.084$. (a) Distribution of number of jams (b) Distribution of jam lengths.

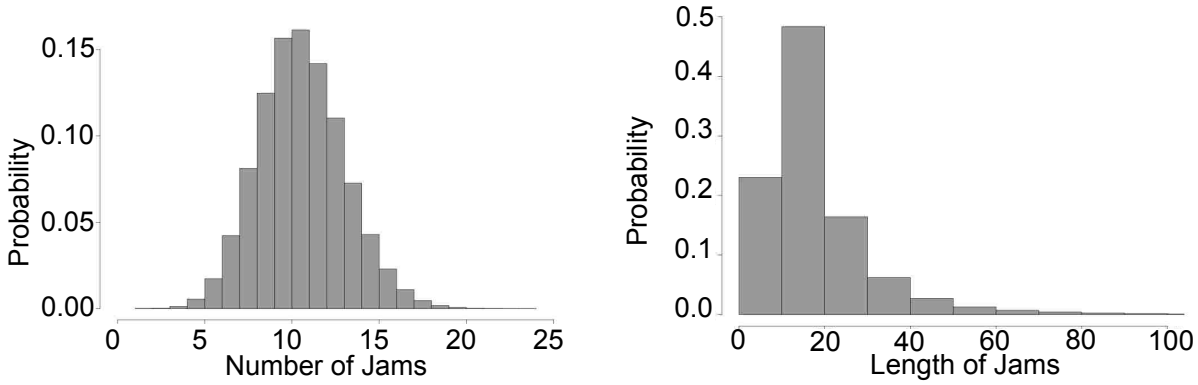

(a) (b)

Figure 2.54: Statistics for 200,000 samples in a system of size $L = 10,000$ for $V_{\max} = 5$, $p = 0.1$ and $d = 0.142$. (a) Distribution of number of jams and (b) Distribution of jam lengths.

For low $V_{\max}$, the system does not break easily into tightly packed jams and a lower density of freely flowing cars. The nucleation of one jam does not depress the density of freely flowing cars sufficiently to inhibit the formation of subsequent jams. As a result, the low $V_{\max}$ system does not have a clear transition region where isolated jams appear, and it is the isolated jams that are responsible for the finite-size effects we see at higher $V_{\max}$. This is clearly seen in the distribution of numbers of jams and jam lengths shown in Figure 2.54. The simulations were done at a density close to the peak flux for $V_{\max} = 5$. The jams are smaller and more frequent than in the $V_{\max} = 9$ data of Figure 2.53.

Once the nucleation of one jam does not significantly inhibit the formation of a second one, we have reached the heavily jammed region and the finite-size effects that appear at high $V_{\max}$ disappear. The mean velocity and flux then follow the relations shown in Figs. 2.19 and 2.21 that are insensitive to the value of $V_{\max}$.

2.6.4 Quantitative Description of the Finite-Size Effects

This picture of a few localized jams condensing out of the free flow phase allows us to make a quantitative description of the finite-size effects in the large $V_{\max}$ simulations. If we assume the jams consist of cars traveling as fast as the gap rule would allow, then their mean speed

would be

$$V_{\rm J} = \sum_{i<V_{\rm max}/2} (i-1)\, P(i)\,, \tag{2.36}$$

and the fraction of the track occupied by the jams is

$$L_{\rm J} = N \sum_{i<V_{\rm max}/2} i\, P(i)\,. \tag{2.37}$$

Since N_0 is the number of cars in a jam, then the density of free cars is changed to

$$d_{\rm eff} = \frac{N - N_0}{L - L_{\rm J}}, \tag{2.38}$$

We then expect that the mean velocity of the mixture would be

$$V_{\rm tot} = \frac{N_0}{N} V_{\rm J} + \left(1 - \frac{N_0}{N}\right) V_{\rm F}(d_{\rm eff})\,, \tag{2.39}$$

where $V_{\rm F}(d_{\rm eff})$ is the flow velocity in the free flow phase taken from the average velocity plot (Figure 2.19) at an effective density $d_{\rm eff}$ given by Eq. (2.38). We evaluate Eqs. (2.36), (2.37), and $V_{\rm F}(d_{\rm eff})$ directly from our simulations to find $V_{\rm tot}$. Figure 2.55 shows the result of this for several track lengths. The agreement with the simulations is excellent in the transition region, and underestimates the mean velocity at higher density where this simple picture of two-phase coexistence breaks down.

2.6.5 Coexistence at the Transition

We have described the behavior of the jams as the second phase appearing at the transition to explain the nature of the finite-size effects for the systems with higher values of $V_{\rm max}$. In this section, we instead focus on the free flowing phase as the existing phase. Now that we have defined two distinct phases by separating the cars in jams, lets take a look at the free flow phase to see if there is any quantitative difference between the low and high $V_{\rm max}$ limit.

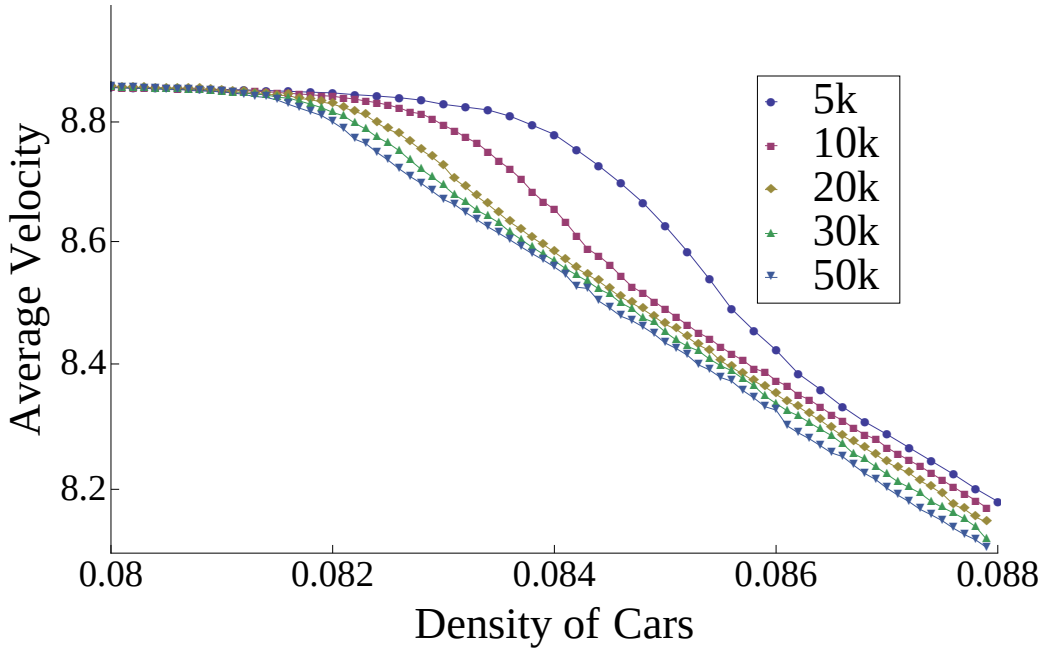

(a)

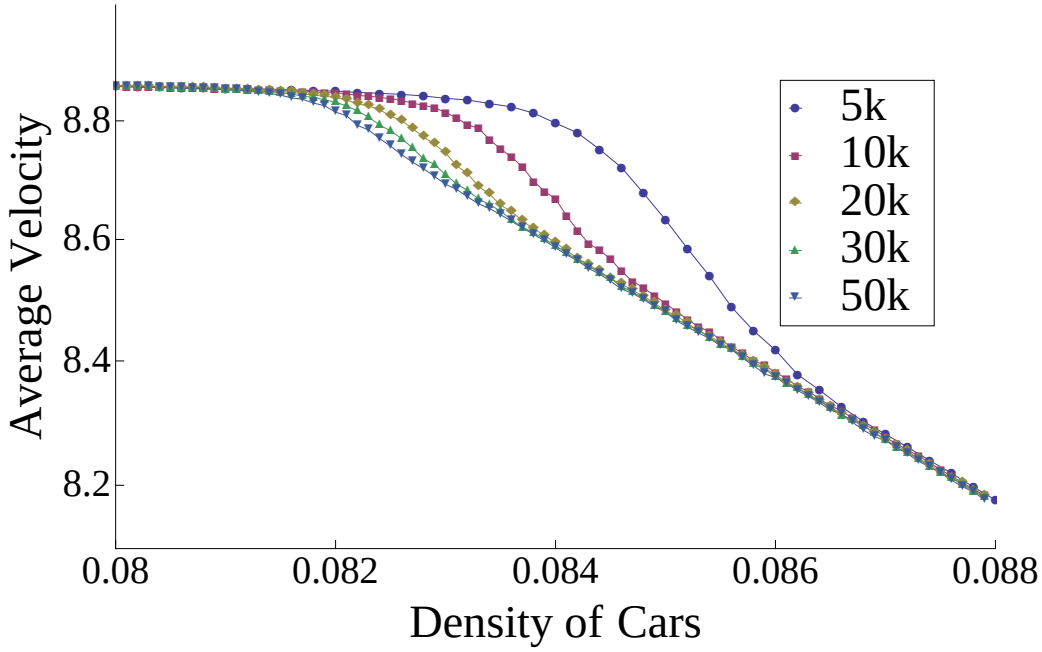

(b)

Figure 2.55: (a) Calculated and (b) simulated average velocity for different track lengths versus density of cars for $V_{\max} = 9$ and $p = 0.1$.

We define the scaled free density to be:

$$d_{\text{sf}} = d_{\text{free}}/d, \tag{2.40}$$

where d_{free} is similar to d_{eff} defined in Equation 2.38. The difference between these two quantities, however, is that d_{free} shows the instant free density, whereas d_{eff} is defined in the asymptotic limit. Division by d (the total density of the cars) makes d_{sf} a dimensionless value between 0 and 1. $d_{\text{sf}} = 1$ means that there is no jam in the track. When any jam exists, $d_{\text{sf}} < 1$. Smaller values of d_{sf} indicate that the free flow phase is farther from the transition area, therefore the average velocity of the cars who are still in the free row phase would be higher. Figure 2.56 shows the time evolution of d_{sf} for same density of cars for different track lengths and $V_{\max} = 5$ and 9. In the case of $V_{\max} = 9$, the plots show that appearance of the jams is more rare in the shorter tracks. It also shows that the changes in d_{sf} are greater for shorter tracks as explained before. For the systems with $V_{\max} = 5$, there are actually the fluctuations that grow and form the jammed phase.

To have a deeper understanding of this difference, we should look at the statistics of the time evolution of d_{sf}. The histogram of d_{sf} is shown in Figure 2.57. The value $d_{\text{sf}} = 1$ indicates the portion of time that there exist no jam in the system while the values of $d_{\text{sf}} < 1$ indicate the portion of time that there exists at least one jam in the system. Histograms are plotted for the same density values but different track lengths for low and high $V_{\max}$ values.

In low $V_{\max}$ limit, histograms show how the jam phase evolves out from the free flow phase as the track gets longer. The two phases are mixed and are not separable with the methods described above. As discussed before, this is because the jams are being created as a result of small fluctuations in velocity. This does not mean the argument about the change in density does not stand here, but the effect of that is much smaller than the fluctuations effect. Therefore, although the histograms are not exactly the same for different track lengths, in the asymptotic limit we can not capture the finite-size effects.

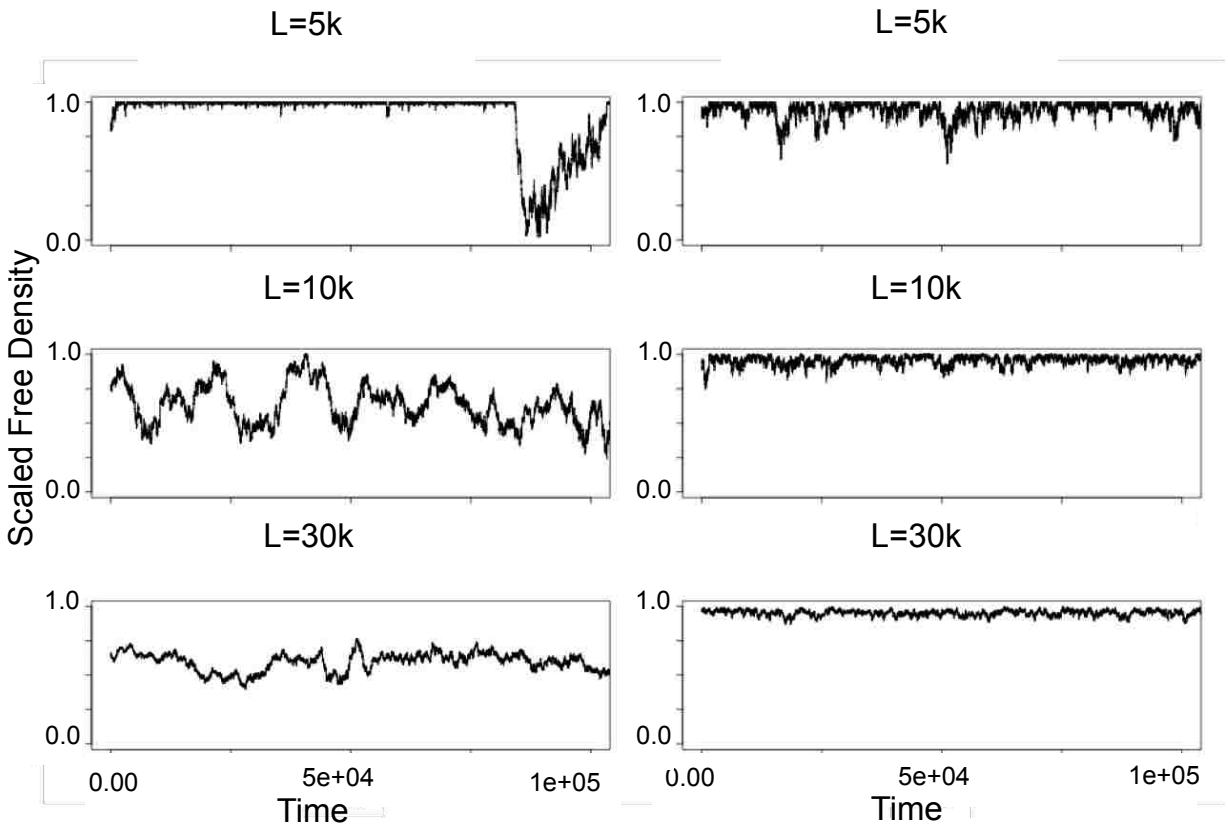

Figure 2.56: Scaled free density vs. time for $V_{\max} = 9$, $d = 0.84$ (left) and $V_{\max} = 5$, $d = 0.13$ (right) and $L = 5k, 10k$ & $30k$. The densities is chosen as the top plot is at just the beginning of the transition while the bottom one is for after the transition.

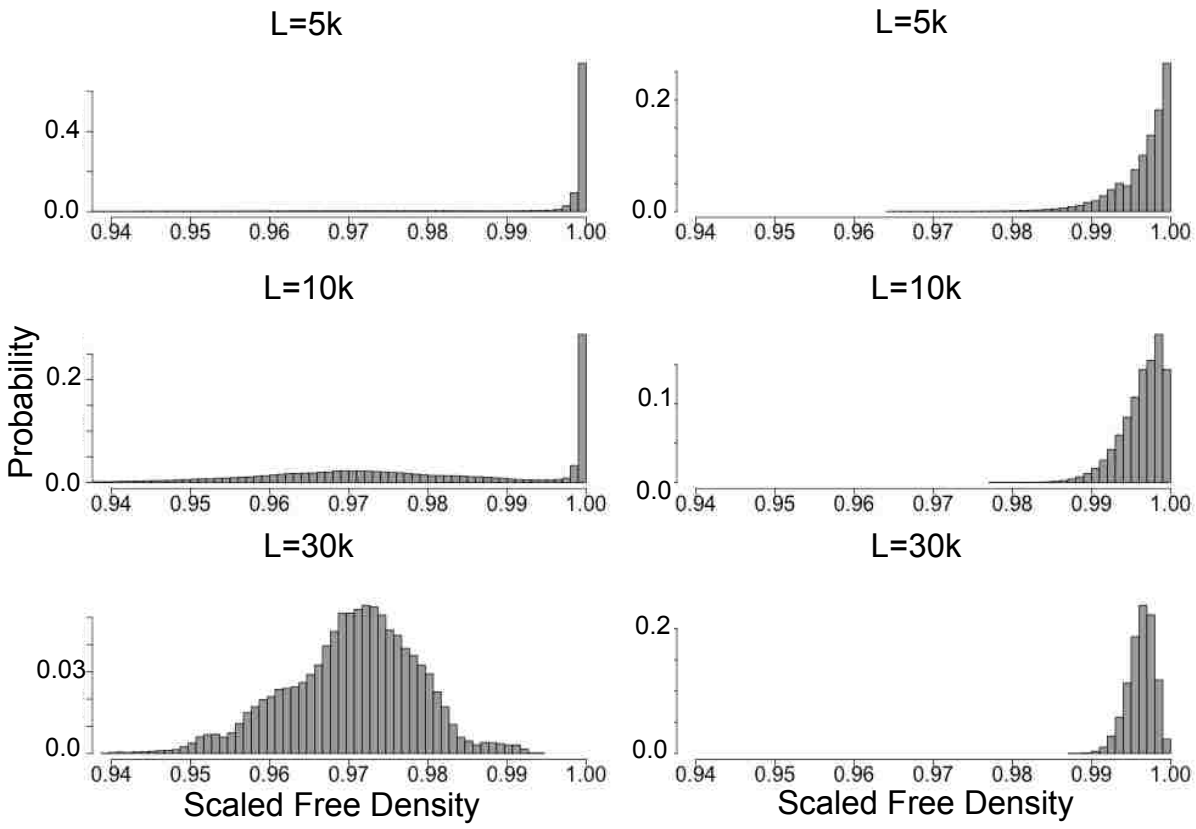

Figure 2.57: Histograms of the scaled free density in Figure 2.56. Plots show how two distinct phases coexist for $V_{\max} = 9$ (left), while the jammed phase just evolves out of the free phase for $V_{\max} = 5$ (right).

In high $V_{\max}$ limit, histograms clearly show two distinct phases coexist with each other at the transition area. While for the shortest track length the system spends most of its time at $d_{\text{sf}} = 1$ (no jam), the second phase starts to grow around some value of $d_{\text{sf}} < 1$ as the track length gets longer. The critical difference here is that for high $V_{\max}$ limit, the second phase does not evolve out of the first phase and appears and grows around a d_{sf} value different than one. This shows why we can claim that there exist two separable phases at the transition area and why all our analytical description works well to describe the behavior of the system at the transition for high $V_{\max}$ values.

2.7 Conclusion

In the dilute regime of the NS model, we have shown that the interactions of a car with the one in front of it in the NS model result, not surprisingly, is a dilute gas of vehicles with a nearest neighbor repulsive interaction of range $\approx V_{\max}$. The gap distribution can be found quantitatively from solving the kinetic equations keeping only pair interactions. Spatial correlations among cars further apart can be described quantitatively through an Ornstein-Zernicke relation.

As has been noticed before, the transition from the free flow to jammed phase in the NS model appears with the nucleation of localized jams in a background of free flow. As the density is raised to the point where jams form, we see that the nearest neighbor interactions fail to describe the density correlations. The jam formation is results in a peak in the gap distribution $P(r)$ for small r representing a set of closely spaced vehicles participating in jams. At the same time, the structure factor $S(q)$ shows a significant upturn for small q, indicating the onset of long range correlations. These new correlations are not the result of including just second or third neighbor correlations.

The present work shows that the nature of the transition exhibited by the vehicle flux and spatial correlations depends on the value of $V_{\max}$. In this regard, the value of $V_{\max}$ plays the role of the number of degrees of freedom (possible velocities) for each object, much like the role of the number of components of a spin variable in an equilibrium system.

Systems with $V_{\max} \gtrsim 6$ show a transition with an intermediate phase that exhibits significant finite-size effects. We can attribute these effects to the existence of large isolated jams that coexist with the free flow phase in this intermediate regime. These large jams act to segregate vehicles and keep the free flow phase stable. The finite-size scaling analysis shows that these long range correlations appear to be universal, with scaling exponents that depend on $V_{\max}$. We are able to quantitatively fit the overshoot seen in the vehicle flux in a finite-size system by accounting for the segregation of the vehicles into jams that reduces the average density of freely flowing cars.

For $V_{\max} \lesssim 6$ we are unable to separate the vehicles into two phases and this transition region with its finite-size effects is either absent or extremely difficult to observe. However, both high and low values of $V_{\max}$ show an upturn in the structure factor, indicating that the regions of large correlated motion, even if they cannot be cleanly denoted as jams, are responsible for the long range correlations in $S(q)$.

3. Optimal measurement-based feedback control for a single qubit: a candidate protocol[1]

3.1 Introduction

Tremendous experimental progress has been made in the last few years in the real-time measurement of mesoscopic systems. The development of parametric amplifiers with very low noise [32, 33, 34] has allowed single qubits to be observed in real-time [35, 36], culminating recently in the first realizations of continuous-time feedback control of a single mesoscopic qubit [37, 38]. Considerable experimental progress is also being made in the feedback control of microscopic systems [38, 39, 40, 41].

It is timely therefore to reflect on the state of the theory of continuous-time measurement-based control of simple quantum systems. While progress has been made in understanding the dynamics induced by continuous measurements, and its implications for feedback control [42, 43, 44, 45, 46, 47, 48], except in certain special cases [49, 50, 51] the optimal adaptive measurement for feedback control of a single qubit is still unknown. On the face of it, the space of control protocols is defined by four parameters that must be specified as a function of the three-parameter density matrix. Such a task is daunting even for numerical optimization. What allows us to solve the problem is a series of arguments, applicable when the noise and target state (the state in which we wish to keep the qubit) are invariant under z-rotations (true for the z-eigenstates and most common noise sources) that allow us to reduce the control problem, approximately in the regime of good control, so that it is determined by a single valued function with a single argument.

For thermal noise the criterion for high-fidelity ("good") control is $k \gg \max(\gamma, \gamma n_T)$. Within that regime, good control is possible even with no feedback Hamiltonian, due to the dynamical effect of the measurement [46]. We will explore primarily the regime of good control, since it is the most useful, but consider within it the full range of feedback strengths,

[1]This chapter previously appeared as: Ashkan Balouchi and Kurt Jacobs, Optimal measurement-based feedback control for a single qubit: a candidate protocol, 2014 New J. Phys. 16 093059 doi:10.1088/1367-2630/16/9/093059. It is reprinted by permission of IOP under the terms of the Creative Commons Attribution 3.0 license - see the permission letter for proper acknowledgment phrase (Appendix A).

ω. Within our class of protocols, we find that the optimal protocol depends strongly on the feedback strength. In fact, we find that there is a "threshold" at which the optimal protocol has a discontinuity.

3.2 Measurement-Base Feedback Control

We begin by reviewing briefly how continuous-measurement based feedback is described. In this kind of feedback control process we monitor an observable of the qubit, producing a continuous stream of measurement results. We will denote the measured observable by

$$\sigma_{\mathbf{m}} = \mathbf{m} \cdot \boldsymbol{\sigma}, \tag{3.1}$$

where $\mathbf{m}$ is a real three-dimensional unit vector, and $\boldsymbol{\sigma} = (\sigma_x, \sigma_y, \sigma_z)$ is the vector of Pauli matrices. From the measurement results we calculate the density matrix of the qubit, $\rho(t)$, in real-time, and at each time t we choose the Hamiltonian of the qubit, $H(t)$, and the observable we measure, $\sigma_{\mathbf{m}(t)}$, based on our knowledge of $\rho(t)$. The rule that we use to choose $H(t)$ and $\sigma_{\mathbf{m}(t)}$ as a function of the density matrix is called the *feedback protocol*. Here our goal is to use feedback to keep the qubit as close as possible to its ground state, $|0\rangle$. Specifically, we wish to maximize the steady-state probability, P, that the qubit is in the ground state. Using the Bloch vector $\mathbf{a}$, defined by

$$\rho = (I + \mathbf{a} \cdot \boldsymbol{\sigma})/2, \tag{3.2}$$

defining $a \equiv |\mathbf{a}|$, and denoting the angle between $\mathbf{a}$ and the ground-state Bloch vector, $\mathbf{a}_0 \equiv (0, 0, -1)$, by θ, this probability is $P = (1 + a\cos\theta)/2$. We will denote the error probability by $\varepsilon \equiv 1 - P$. In the regime of good control, defined by $\varepsilon \ll 1$, we have

$$\varepsilon = \Delta/2 + a\theta^2/4 + \mathcal{O}(\theta^4), \tag{3.3}$$

where we have defined $\Delta \equiv 1 - a$. In the regime of good control, the qubit spends most of its time in states for which θ and Δ are small parameters.

Under a continuous measurement of $\sigma_{\mathbf{m}}$, and a Hamiltonian H, the dynamics of the qubit are given by the stochastic master equation (SME) [52, 53],

$$\begin{aligned} d\rho &= -\frac{i}{\hbar}[H(t), \rho]dt - k[\sigma_{\mathbf{m}}, [\sigma_{\mathbf{m}}, \rho]]dt \\ &\quad + \sqrt{2k}(\sigma_{\mathbf{m}}\rho + \rho\sigma_{\mathbf{m}} - 2\langle\sigma_{\mathbf{m}}\rangle\rho)dW, \end{aligned} \tag{3.4}$$

where k, referred to as the *measurement strength*, determines the rate at which the measurement extracts information, and dW is an increment of Wiener noise [1]. The continuous stream of measurement results, $y(t)$, is given by

$$dy(t) = \langle\sigma_{\mathbf{m}}\rangle dt + dW/\sqrt{8k}. \tag{3.5}$$

We can write all single qubit Hamiltonians in the form

$$H = \hbar(\mu/2)\mathbf{n} \cdot \boldsymbol{\sigma}, \tag{3.6}$$

where $\mathbf{n}$ is a real, unit norm, three-dimensional vector. Here μ is the speed of rotation on the Bloch sphere, if the initial state is such that the path is a great circle (The angular speed of rotation in Hilbert space is $\mu/2$).

Optimal control only makes sense when there are constraints on the speed at which we can manipulate and/or measure the qubit. Here we take these constraints to be $\mu \leq \omega$, and $k \leq k_{\max}$, for some positive real numbers ω and $k_{\max}$. We allow the controller to measure in any basis, and apply a Hamiltonian that rotates in any direction.

Here we will assume our qubit is driven by thermal noise, for which the master equation is [54]

$$\dot{\rho} = \frac{\gamma}{2}(n_T + 1)\mathcal{D}(\sigma)\rho + \frac{\gamma}{2}n_T\mathcal{D}(\sigma^\dagger)\rho, \tag{3.7}$$

where

$$\mathcal{D}(c) \equiv 2c\rho c^\dagger - c^\dagger c\rho - \rho c^\dagger c. \tag{3.8}$$

Here $\sigma = (\sigma_x - i\sigma_y)/2 = |0\rangle\langle 1|$ is the lowering operator, γ is the damping rate, and n_T is determined by the temperature and the energy gap between the ground and excited states of the qubit. The excited-state population at thermal equilibrium is given by

$$P_T^{\mathrm{e}} = n_T/(1 + 2n_T). \tag{3.9}$$

Thermal noise includes decay as a special case ($n_T = 0$), and we note that the arguments we employ below apply also to dephasing and depolarizing noise. We note that all these noise sources are symmetric under rotations about the z-axis, and our measure of performance, ε, has the same invariance. Combined with the fact that we can measure any observable, and apply a Hamiltonian at any angle, this means that wherever the state moves on the Bloch sphere, we can always redefine the xz-plane (or equivalently rotate the qubit) so that it is in this plane, without affecting the control problem. We therefore require only the two parameters $\Delta = 1 - a$ and θ to describe the state of the qubit, and we can write the density matrix as

$$\rho = [I + a(\sin\theta\sigma_x - \cos\theta\sigma_z)]/2. \tag{3.10}$$

3.3 Optimal Measurement-Based Feedback Control Protocol

We now present a series of arguments that allows us to greatly simplify the control problem in the regime of good control. The first asserts that the future performance of the control protocol will never be worse if we rotate the state closer to the target (that is, reduce θ). Because the set of available controls is invariant under rotations, it is intuitively obvious that we cannot rotate the state further from the target to gain at some later time. This implies that we should always choose the feedback Hamiltonian so as to reduce θ as fast as possible, thus setting $\mu = \omega$. The resulting feedback Hamiltonian is that given in Eq.(3.11).

The second argument asserts that it is never beneficial to reduce the measurement strength below its maximal value. This stems from the fact that we can always choose to measure the qubit in the basis in which it is diagonal. Because this measurement purifies the state of the qubit without disturbing it, it cannot be detrimental to the future performance of the protocol. Since this measurement is always available, an optimal protocol can always choose $k = k_{\max}$.

The third argument concerns the basis in which we measure the qubit. Previous studies have shown that this basis has a non-trivial effect on the dynamics of both a and θ. Measuring in an basis orthogonal to the Bloch vector increase a the fastest (on average) but also causes the maximum diffusion in the direction of the Bloch vector θ. Our question is whether we can restrict our measurement bases to those that lie in the xz-plane. It is clear that if we measure in the y-direction, we will obtain the fastest increase in a while producing the smallest disturbance to θ, since the diffusion is induced in the plane containing the y-axis and the Bloch vector. However, when θ is small, while the effect of the measurement is zeroth order in θ, the difference between the effect of an x-measurement and a y-measurement is first order in θ, due to the rotational invariance about the z-axis. We can conclude that measuring in a basis outside the xz-plane will have only a small effect on the performance. Restricting our measurements to the xz-plane means that they are parametrized by a single angle α. Naturally we define α so that $\alpha = \theta$ means that the measurement axis is aligned with the Bloch vector.

The forth and final argument asserts that in the regime of good control, little performance is lost by allowing the measurement angle α to be independent of the length of the Bloch vector, a. This insight comes from examining the equations of motion for the angle θ and length a under a measurement at angle $\phi = \alpha - \theta$ to the Bloch vector. We find that the equation of motion for θ is independent of a to leading order in the small parameter Δ. Thus the value of a has little influence when choosing α for the purposes of controlling θ. While the equation of motion for a involves ϕ, its form shows that the rate at which a increases,

the key quantity affecting performance as far as a is concerned, is not increased by making ϕ depend on a. We give the details of the above analysis in the supplementary material. This conclusion is supported by the fact that for $\omega = 0$, the optimal choice of $\alpha(\theta)$ that we will obtain by numerical optimization below agrees with that obtained analytically by setting $a = 1$ (Eq.(3.15) below).

The above arguments allow us to fix the measurement strength k and the feedback rate μ, and parametrize the measurement by a single angle α. They further assert that the key question in the feedback control of a single qubit (given noise with z-symmetry) is how to choose α as a function of θ: almost all of the performance is determined by this choice. To answer this question we now turn to numerical optimization. The problem is still potentially rather complex, since α could be any function of θ. To make headway we write $\alpha = f(\theta)$ and expand the function f as a power series in θ: $\alpha = \sum_{n=0}^{\infty} c_n \theta^n$. We truncate the power series, keeping only c_0 through c_3, and run the resulting feedback protocol to determine the average steady state error, $\langle \varepsilon \rangle$. We then perform a numerical optimization over the space of the four parameters c_n to find what values of the coefficients c_n achieve the minimum $\langle \varepsilon \rangle$. For this optimization we use the BFGS gradient search method [55]. We set $k = 1$ (that is, we measure time in units of k), $\gamma = 0.01k$ and $n_T = 0.1$, so that we are in the regime of good control (we find that good control requires $k \gg \max(\gamma, n_T\gamma)$). The results of running the optimization for a range of values of the feedback strength, ω, are enlightening. The error $\langle \varepsilon \rangle$ is dominated by the first two parameters in the power series expansion, c_0 and c_1. Within the statistics of our results, in which we averaged over 128000 noise realizations, the values of c_2 and c_3 have no significant effect on the performance. In view of this we simplify the class of protocols in our search space further by keeping only c_0 and c_1: α is now a linear function of θ.

To find the best protocol for each value of ω we must explore the performance as a function of our three parameters, c_0, c_1, and ω. Using the same values for k, γ, and n_T as above we calculate $\langle \varepsilon \rangle$ for the full range of values of c_0, and for $c_1 \in [-2, 2]$, for a discrete set

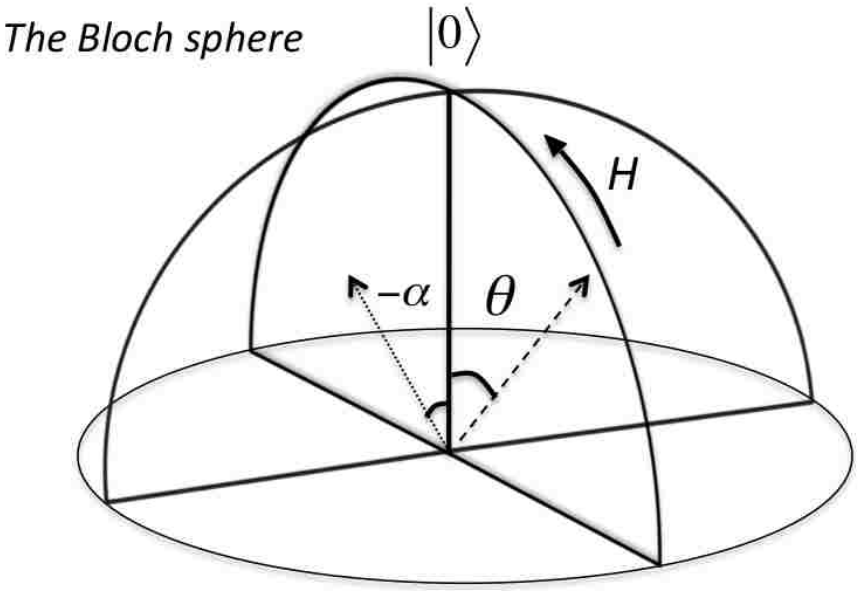

Figure 3.1: Here we depict various elements of the feedback control protocol. We have drawn the Bloch sphere with the ground state $|0\rangle$ at the top. The dashed arrow is the Bloch vector with angle θ. The grey arrow shows the direction of the measured spin at angle $-\alpha$. The curved arrow shows the direction that the feedback Hamiltonian will rotate the Bloch vector, at angular speed ω .

of values of ω. These results, given in the supplementary material, show that the minimum is always at $c_0 = 0$ for $\omega \lesssim 45k$, regardless of the value of c_1, and at $|c_0| = \pi/2$ for $\omega \gtrsim 45k$, regardless of the value of c_1. At $\omega \approx 45k$ the values $c_0 = 0$ and $|c_0| = \pi/2$ give the same performance, at least to the accuracy of our results. The fact that the optimal landscape has this structure considerably simplifies the task of finding the optimal values of c_1, and thus determining the full control protocol. All we have to do is to find the optimal values of c_1 along the two line segments defined by $(c_0 = 0, 0 < \omega < 45k)$ and $(c_0 = \pi/2, \omega > 45k)$. We find that c_1 does not have a significant effect on the performance for $\omega \gtrsim 30k$, and so for the second line segment its value is unimportant. For $c_0 = 0$ we obtain the optimal value of c_1 as a function of ω by hand, and find that the exponential function given in Eq.(3.14) fits the data points quite well, with the parameters A, B, and r given in Table 3.1 for three values of γ. In fact, the noise in, and resolution of, our data points means that they have significant fluctuations around this fitted function. Since we do not know that the optimal value of c_1 really follows the exponential function, the fluctuations of our data points about

the fitted curve are a better measure of the error in our choice of c_1 than the estimated errors in the fitted parameters A, B, and r. The mean, m, and standard deviation, σ, of these fluctuations are also given in Table 3.1. As an example of the significance of c_1, for $\gamma = 0.1$ and $\omega = 10k$, choosing the optimal value of c_1 (~ -0.7) gives a steady-state error of $\varepsilon = 3.3 \times 10^{-3}$, whereas setting $c_1 = 0$ gives $\varepsilon = 4.6 \times 10^{-3}$. A change in c_1 of 0.01 (the level of our uncertainty in the optimal value) changes ε by less than 5%. As ω increases the importance of c_1 decreases: for $\omega = 20k$, setting $c_1 = -0.7$ gives $\varepsilon = 3.0 \times 10^{-3}$, and $c_1 = 0$ gives $\varepsilon = 3.4 \times 10^{-3}$.

We can now summarize our control protocol. The feedback Hamiltonian is

$$H(t) = \mathrm{sgn}[\theta(t)]\hbar(\omega/2)\sigma_y. \tag{3.11}$$

The measured observable is $\sigma_\alpha = \sin\alpha\sigma_x - \cos\alpha\sigma_z$, with

$$\alpha = c_0 + c_1\theta(t), \tag{3.12}$$

and

$$c_0 = \begin{cases} 0 & \omega \lesssim 45k \\ \pi/2 & \omega \gtrsim 45k \end{cases}, \tag{3.13}$$

$$c_1 = -A - B[1 - e^{-r\omega/k}]. \tag{3.14}$$

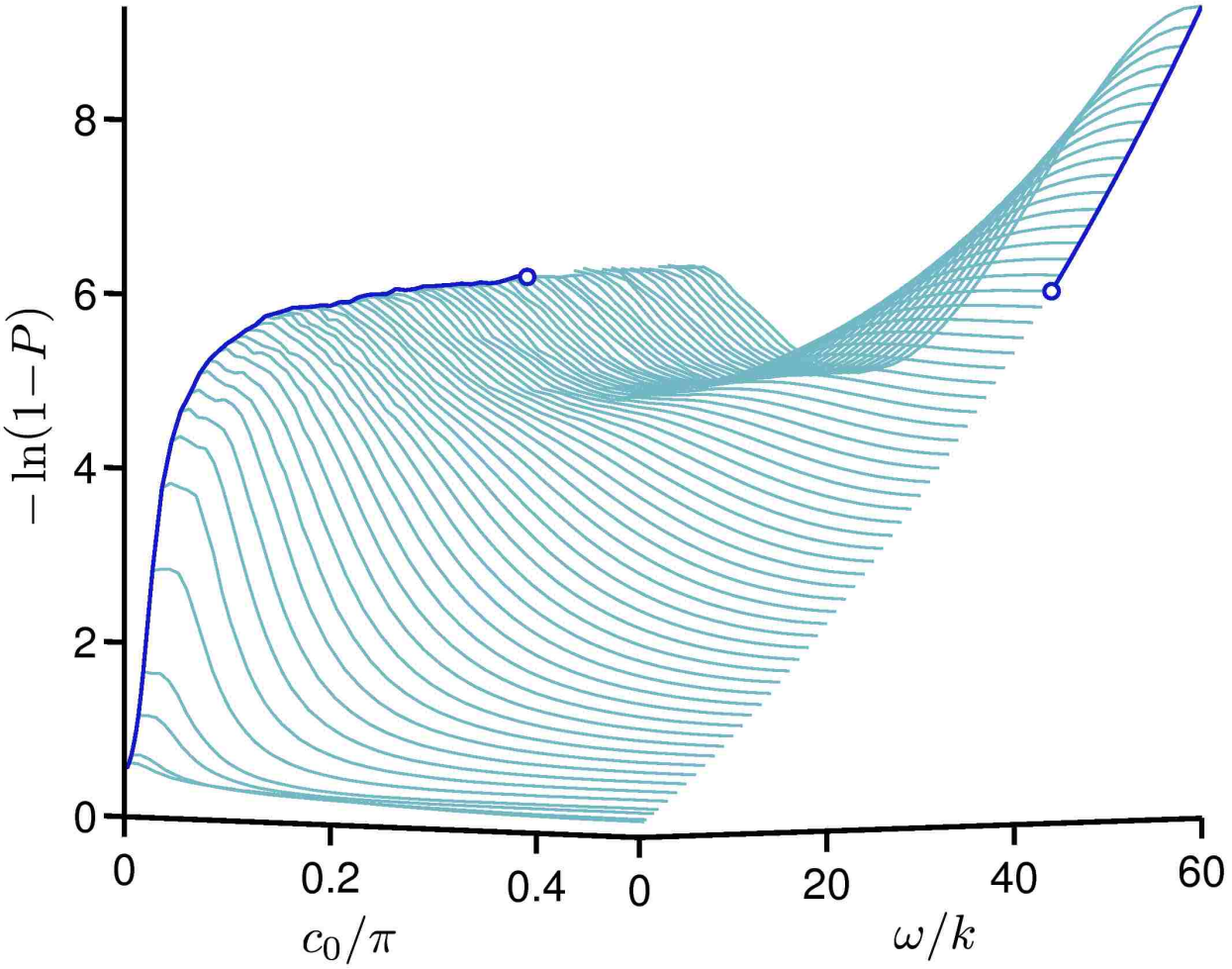

Figure 3.2: Graph of negative natural logarithm of ε (steady-state error) vs. control parameter c_0 and feedback strength (ω), with the value of c_1 given by Eq.(3.14). Our protocol is defined by the parameters c_0 and c_1, and is defined in Eqs.(3.11) through (3.14). The thick lines show i) the value of c_0 for our protocol as a function of ω, and ii) the performance of our protocol which is the result of optimizing over c_0 and c_1. This discontinuity in the protocol occurs at $\omega \approx 45k$.

3.4 The Performance of the Feedback Protocol

To show how the optimal performance, defined as the minimum steady-state error, depends on ω we now plot the performance as a function of c_0 and ω in Figure 3.2. In this plot we set the value of c_1 to that given by Eq.(3.14). This choice gives the best performance (the performance of our protocol) for $c_0 = 0$ and for $|c_0| = \pi/2$ for $\omega > 45k$ (that is, when c_0 has its optimal value), since in the latter case the value of c_1 is unimportant. So the plot gives the performance of our protocol, but does not show the best performance that can be obtained when c_0 is outside its optimal value and $\omega \lesssim 30k$.

We can understand the main features of this protocol in terms of three known dynamical effects of continuous measurement. The first is that a measurement in a basis close to that of the Bloch vector tends to "drag" the Bloch-vector in the direction of the measurement. This explains why the co-efficient c_1 is negative: this causes the measurement to drag the state towards $|0\rangle$. The second effect comes from the fact that measuring at an angle $\alpha \neq \theta$ generates diffusion for θ. The amount of diffusion is proportional to $\sin(|\theta - \alpha|)$, and a gradient in the diffusion rate pushes the state into regions of low diffusion [46]. Our protocol states that when there is no feedback Hamiltonian ($\omega = 0$) we should should set $\alpha = -\theta/2$. This means increasing the difference between α and θ, away from the target state, thus increasing the diffusion. The resulting diffusion gradient pushes the state towards $\theta = 0$.

We note that it is possible to derive the optimal value of c_1 for $\omega = 0$ from an approximate calculation. Assuming that the system stays close to the target state throughout its evolution so that we can set $\cos\theta \approx 1 - \theta^2/2$, and setting $a \approx 1$, we obtain the following equation of motion for θ^2 under the measurement and feedback:

$$\begin{aligned} d(\theta^2) &= \{4\gamma n_T - 2\omega|\theta| + [8kc_1(c_1+1) - \gamma]\theta^2\}dt \\ &\quad + \sqrt{2k}(1+c_1)\theta^2 dW. \end{aligned} \tag{3.15}$$

Table 3.1: Values for the parameters of Eq.(3.14)

γ	A	B	r	m	σ
0.1	-0.500	0.186	0.476	0.002	0.007
0.2	-0.479	0.211	0.705	-0.005	0.011
0.3	-0.478	0.217	0.529	0.001	0.008

If we set $\omega = 0$ (no feedback Hamiltonian) and take the average on both sides, then we obtain a stochastic equation for $\langle\theta^2\rangle$ that can be solved analytically [1]. Solving this equation for the steady-state shows that the minimum value of $\langle\theta^2\rangle$ occurs at $c_1 = -0.5$.

3.5 Conclusion

In the regime of strong feedback ($\omega > 45k$) our protocol tells us to measure approximately at right angles to the Bloch vector, causing the maximum diffusion in θ. This can be understood from a third property of measurement: the average rate at which the measurement purifies the state (that is, lengthens the Bloch vector), is greatest when the diffusion is greatest. When the feedback Hamiltonian is sufficiently fast ($\omega \gg k$) it can suppress the unwanted diffusion and thus take advantage of the increased purification. That this would be true for sufficiently strong feedback was already known [42, 49] — what is unexpected is that the optimal value of c_0 switches abruptly from 0 to $\pi/2$ at a given value of ω/k.

To summarize, we have obtained a feedback control protocol for a single qubit that gives a nontrivial prescription for choosing the measurement angle as a function of the direction of the Bloch vector and the feedback strength. Analytical arguments and numerical evidence suggest that this protocol is close to optimal in the regime of good control. Numerical optimization suggests that out of all protocols in which the measurement angle is chosen to be independent of the length of the Bloch vector, this protocol is close to optimal in the regime of good control. We suspect that in this regime, extending the protocol to allow the measurement angle to depend on the length of the Bloch vector would have only a minor affect on performance.

3.6 Supplement to "Optimal measurement-based feedback control for a single qubit: a candidate protocol"

Here in the first section we show why the measurement angle, α, can be chosen independently of the length of the Bloch vector, a, in the regime of good control. In the second section we present plots demonstrating that, regardless of the value of c_1, the minimum value of ϵ is always at $c_0 = 0$ for $\omega \lesssim 45k$, and at $|c_0| = \pi/2$ for $\omega \gtrsim 45k$. In the third section we show the data points and the corresponding fit to these points given by the function in Eq.(5).

3.6.1 The measurement angle and the length of the Bloch vector

Recall that our Bloch vector lies in the xz-plane. It is simplest to derive the equations of motion for the length and angle of the Bloch vector by assuming that the Bloch vector is pointing directly upwards, so that $a = a_z$ and $a_x = a_y = 0$, and make a measurement at an angle ϕ to the z-axis. Using Eq.(1), and writing ρ in terms of the Bloch vector elements, we obtain the equations of motion for a_x and a_z:

$$da_x = 2k\sin(2\phi)a_z dt + \sqrt{8k}\sin\phi\, dW \tag{3.16}$$

$$da_z = -4k\sin^2\phi a_z dt + \sqrt{8k}\cos\phi\,(1-a_z^2)dW. \tag{3.17}$$

Defining the angle θ as the angle between the Bloch vector and the z-axis, we have $\theta = \tan(a_x/a_z)$. From the above equations we can derive the equations of motion for θ and a. Given that the Bloch vector points upwards, so that $\theta = 0$, these equations are

$$d\theta = 2k\sin(2\phi)\left(3-\frac{2}{a^2}\right)dt + \sqrt{8k}\sin\phi\left(\frac{1}{a}\right)dW \tag{3.18}$$

$$da = 4k\sin^2\phi\left(a-\frac{2}{a}\right)dt + \sqrt{8k}\cos\phi(1-a^2)dW. \tag{3.19}$$

When a is close to unity, the regime of good control, we can expand these equations as a power series in $\Delta = 1 - a$. Keeping terms up to first order in Δ this gives

$$d\theta = 2k \sin(2\phi)\,(1 - 4\Delta)\,dt + \sqrt{8k}\sin\phi\,(1 + \Delta)\,dW \tag{3.20}$$

$$da = -4k \sin^2\phi\,(1 + 3\Delta)\,dt + 2\Delta\sqrt{8k}\cos\phi\,dW. \tag{3.21}$$

We see immediately that the equation of motion for θ is not dependent on Δ to leading order. The length of the Bloch vector has therefore little effect on the dynamics, and thus the control, of θ in the regime of good control.

Examining the equation of motion for a we see that the deterministic term is also independent of a to leading order, but this is not true of the stochastic term. The fact that the stochastic term is proportional to Δ is precisely the diffusion gradient induced by the measurement, and by which the measurement increases the length of the Bloch vector (makes the state more pure). The observation is that as far as this diffusion gradient is concerned, making ϕ dependent on Δ has the same action as changing the measurement strength. On physical grounds it is apparent that modulating the measurement strength, and thus reducing it below its maximal value, cannot increase the rate at which the measurement purifies the state.

To use a more direct mathematical argument, if we choose ϕ as a function of Δ so that the stochastic term is proportional to a higher power of delta, then we reduce the diffusion gradient. Numerical simulations show that if we make the stochastic term proportional to $\sqrt{\Delta}$, instead of Δ, the rate at which a increases is also reduced.

3.6.2 The maximum performance and the value of c_0

In Figure. 3.3, we display four plots that show how the maximum performance changes abruptly from $c_0 = 0$ below $\omega \approx 45k$ to $|c_0| = \pi/2$ above it. For $\omega < 30k$ there is only a single maximum in the performance as function of c_0, and this occurs at $c_0 = 0$.) Between $\omega = 30k$ and $\omega = 45k$ a second local maximum appears at $c_0 = \pm\pi/2$. At $\omega = 45k$ the two maxima are approximately equal (to within the accuracy of our simulations), and for $\omega > 45k$ the second maxima overtakes the first, and so the optimal value of c_0 switches from 0 to $\pm\pi/2$.

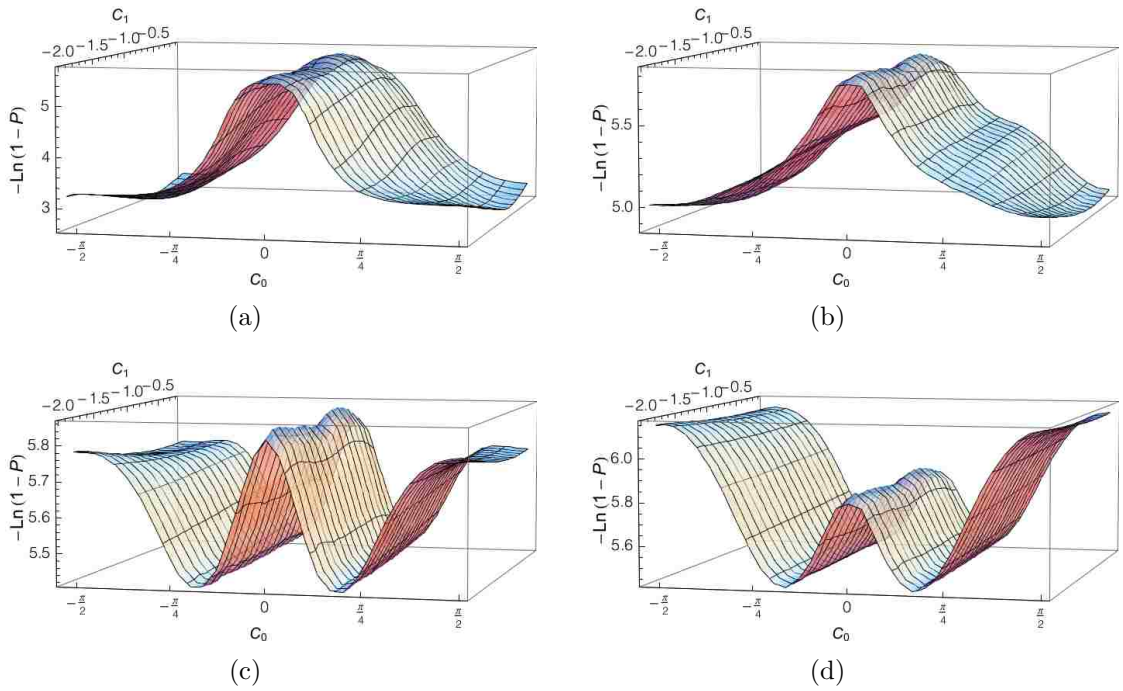

Figure 3.3: Plots of the negative natural logarithm of $\epsilon = 1 - P$ (the steady- state error) vs. control parameters c_0 and c_1 for four values of the feedback strength: (a) $\omega = 10k$; (b) $\omega = 30k$; (c) $\omega = 45k$; (d) $\omega = 50k$. The simulation is done by setting $k = 1$ (that is, we measure time in units of k), $\gamma = 0.01k$ and $n_T = 0.1$, and averaging over 128000 noise realizations.

3.6.3 Fitting the function for c_1

In Figure 3.4 we show the numerical results for the optimal value of c_1 as a function of feedback strength, for three values of the noise rate γ. This function is

$$c_1 \;=\; -A - B[1 - e^{-r\omega/k}], \tag{3.22}$$

where A, B, and r are the fitting parameters. The values of theses parameters, for the three values of γ are given in Table 3.1. For these simulations we set $k = 1$ (that is, we measure time in units of k) and $n_T = 0.1$, and we average over 128000 noise. realizations.

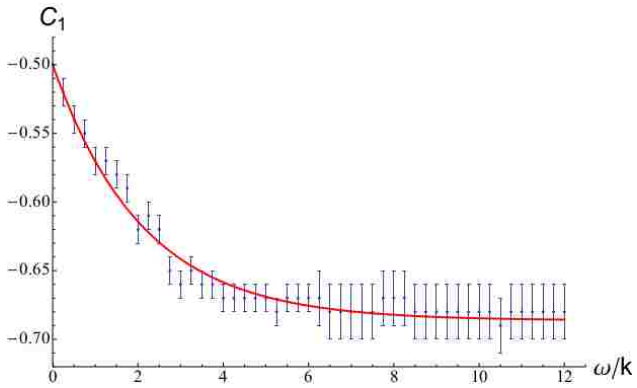

(a)

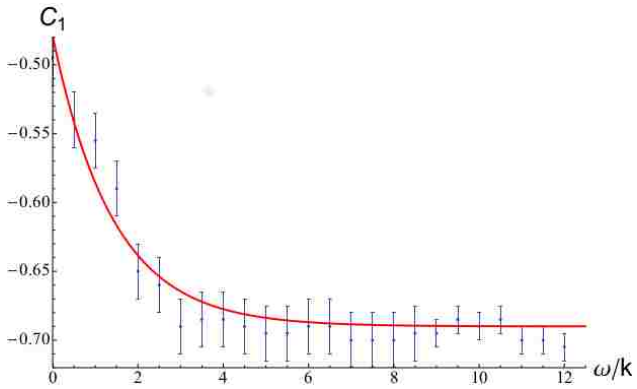

(b)

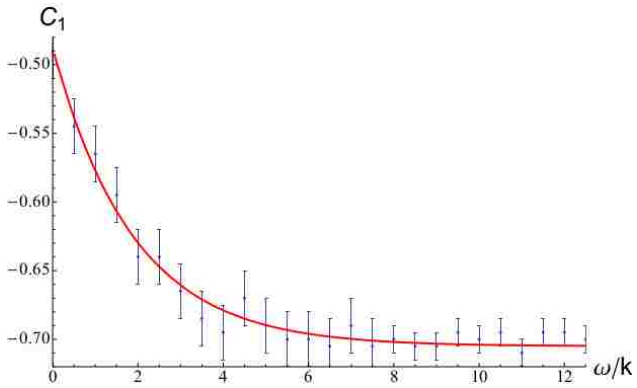

(c)

Figure 3.4: The fitted function for the optimal value of c_1 as a function of feedback strength, for three values of the noise rate γ: (a) $\gamma/k = 0.1$; (b) $\gamma/k = 0.2$; (c) $\gamma/k = 0.3$. The error-bars show our estimates of the error in the numerical value of c_1, given the accuracy with which we can determine the minimum of ε.

4. Conclusion

Nature is filled with complex stochastic dynamical systems. Studying dynamical systems is of great importance in understanding the world around us. The main outcome of studying dynamical systems is to figure out the macroscopic behavior of the system for different sets of microscopic configurations of its components. To achieve this goal, we need to use probability theory, statistical tools, and stochastic analysis.

The complexity of the dynamical systems is in general due to the large number of degrees of freedom in the system. This can be either due to the large number of system components or large number of degrees of freedom of even a single component. Dynamics of the traffic flow is an example of many body complex dynamical systems. Dynamics of a single qubit is an example of a complex system with only one component and many degrees of freedom.

In addition to understanding the underlying dynamics of the system, one might be interested in controlling the system. Control theory is designed to alter the input of the system or its dynamics in order to temper the outcome of the system toward the desired state. Feedback control is a protocol to control the system using the information of the current state of the system. Due to its definition, feedback control theory is based on real time measurements of the properties of the system.

In classical systems, e.g. in traffic flow, measurement does not change the current state of the system, therefore the information can be obtained independently and be fed to the feedback protocol. In quantum systems, e.g. in qubit problem, measurement itself may alter the current sate of the system. We need to keep track of the possible changes of the system due to measurement process as well. We can benefit the effects of the measurement on quantum mechanical systems in our feedback protocol by applying weak measurement on the system. In other words the measurement itself could be used as the altering Hamiltonian in the feedback protocol. This specific arrangement of continuous weak measurements is known as measurement-based feedback control.

In this dissertation, I have studied two choices of classic and quantum dynamical systems by implementing a variety of numerical analyses and statistical tools. I performed a study on properties of the Nagel-Schreckenberg traffic flow model as an example of a classical many body complex dynamical system. In addition, I have studied the cooling process of a single qubit using the measurement-based feedback control theory as an example of a quantum dynamical system with may degrees of freedom.

Nagel-Schreckenberg is a simple cellular automaton model. In this model, each vehicle is considered as a cell with very simple rules for its dynamics. The complexity of the system is due to the large number of vehicles in the system. The NS model mimics some of the important features of the traffic flow. I have shown that in the dilute regime of the NS model, there exists no long range correlation in the system. The interactions of the car with the one in front of it is a dilute gas of vehicles with nearest neighbor repulsive core of range $\approx V_{\max}$.

The NS model exhibits a phase transition from the free flow regime to the jammed regime. I studied this transition for different values of maximum velocity $V_{\max}$. The main tools I have used to study the phase transition in the NS model are the spatial correlations in the system: nearest neighbor correlation $P(r)$, pair correlation $G(r)$, and its Fourier transform (the structure factor) $S(q)$. I have shown that long range correlation appears and grows in the system at the transition. This long range correlation is mainly among the cars participating in the jams.

This study shows that the nature of the transition depends on the value of $V_{\max}$. In this regard, the value of $V_{\max}$ (as a number of different values of velocity the vehicle can obtain) can be considered as a measure of number of degrees of freedom. Existence of the long range correlation causes significant finite-size effects for variety of order parameters in the system for a range of $V_{\max} \gtrsim 7$. No size sensitive behavior could be observed for $V_{\max} \lesssim 7$.

I have performed finite-size scaling analysis to find the critical exponents of the NS model. I introduced a numerical optimization method to find the scaling exponents. The performance of this method has been checked for 3d Ising model. I showed that the obtained values for the critical exponents of the 3d Ising model are in great agreement with commonly accepted values.

We can attribute the finite-size effects of the NS model to the existence of an intermediate phase in the system with $V_{\max} \gtrsim 7$ at the transition. In this intermediate regime large isolated jams coexist with the free flow phase. These large jams act to segregate vehicles and keep the free flow phase stable. This effect is more observable for the tracks with shorter length, therefore the order parameters such as average velocity and average flux intend to have larger values in the shorter systems at the transition. This effect can not be observed in the systems with $V_{\max} \lesssim 7$ due to large fluctuations in the vehicle's velocity.

The main goal in controlling the traffic flow is to maximize the average flux of the vehicles. The fundamental diagrams of the average flux for a given system size show that the flux increases as the random slow down factor p decreases at any given density. They also show that for a given random slow down value, there is a certain density which maximizes the flux. The fundamental diagrams of the average flux for different system sizes, show that around the transition area, the flux has a higher value for the shorter tracks. Comparing the average flux for different values of $V_{\max}$ indicates that in certain ranges of density, there is an optimum value for the $V_{\max}$ which can maximize the flux. The most important key in controlling the transition in traffic flow is existence of the long range correlation. Long range correlation in the system indicates that global information is needed for the feedback protocol in order to control the system. In other words, in future smart car technology, just local commutation between the cars (e.g. via bluetooth) would not provide sufficient information for the control protocol and global information of all the vehicles on the road (e.g. via GPS) should be provided to the protocol.

Not only in classical but also in quantum systems we can apply the feedback control theory to obtain a desired state. Preparing quantum systems in pure states is important in quantum technologies. To prepare a pure state, entropy is needed to be extracted from the system similar to cooling to a non-degenerate ground state. Finding the maximum achievable ground state population of a single qubit for a given maximum control force and the environment noise is the goal of feedback control protocol I have studied. I have used the measurement as the controlling force in the control protocol, since measurement of the quantum system changes its state.

I showed that for a broad class of noise processes, a series of compelling arguments can be applied to greatly simplify the problem of steady-state preparation of the ground-state. Using numerical optimization, I have obtained a measurement-based feedback control protocol for cooling a single qubit that gives a nontrivial prescription for choosing the measurement angle as a function of the direction of the Bloch vector and the feedback strength. The measurement angle is independent of the length of the Bloch vector. The protocol can be described relatively simple, and contains a discontinuity as a function of feedback strength.

Ability to apply real time feedback control theory on stochastic dynamical systems is currently one of the most demanding applications. Although most of the problems in this field need particular case studies, a few tools are commonly used. In this dissertation, I have presented two examples of classic and quantum complex dynamical systems. I have performed a vast variety of analytical and numerical analyses and I have used several statistical tools for this study. Most of these tools such as Monte Carlo simulation, correlation functions, finite-size scaling, Bayesian probability, and stochastic master equation can be used in many other similar problems. It is of great importance to use these tools in a proper way to explore the underlying features of the complex dynamical systems and eventually to control these systems.

References

[1] K. Jacobs. *Stochastic Processes for Physicists: Understanding Noisy Systems*. Cambridge University Press, Cambridge, 2010.

[2] Don S. Lemons. *An introduction to stochastic process in physics*. The Johns Hopkins University Press, 2002.

[3] S. Chandrasekhar. Stochastic Problems in Physics and Astronomy. *Reviews of Modern Physics*, 15(1):1–89, January 1943.

[4] D. Helbing. Traffic and related self-driven many-particle systems. *Rev. Mod. Phys.*, 73(4):1067–1141, December 2001.

[5] Andrew C. Doherty, Hideo Mabuchi, Sze M. Tan, Jacobs K., and Salman Habib. Quantum feedback control and classical control theory. *Physical Review A*, 62(1):012105, June 2000.

[6] Xiaoting Wang, Sai Vinjanampathy, Frederick Strauch, and Kurt Jacobs. Absolute Dynamical Limit to Cooling Weakly Coupled Quantum Systems. *Physical Review Letters*, 110(15):157207, April 2013.

[7] D. Chowdhury. Statistical physics of vehicular traffic and some related systems. *Phys. Rep.*, 329(4-6):199–329, May 2000.

[8] M. J. Lighthill and G. B. Whitham. On kinematic waves: Ii. a theory of traffic flow on long crowded roads. *Proc. Roy. Soc.*, 229:317–345, 1955.

[9] I. Prigogine and R. Herman. *Kinetic Theory of Vehicular Traffic*. Elsevier, 1971.

[10] T. Nagatani. The physics of traffic jams. *Rep. Prog. Phys.*, 65(9):1331–1386, September 2002.

[11] K. Nagel and M. Schreckenberg. A cellular automaton model for freeway traffic. *J. Phys. I*, 2(12):2221–2229, December 1992.

[12] K. Nagel and M. Paczuski. Emergent traffic jams. *Phys. Rev. E*, 51(4):2909–2918, April 1995.

[13] S. Lübeck, M. Schreckenberg, and K. D. Usadel. Density fluctuations and phase separation in a traffic flow model. *Phys. Rev. E*, 57:1171, January 1998.

[14] D. Chowdhury, K. Ghosh, A. Majumdar, S. Sinha, and R. B. Stinchcombe. Particle-hopping models of vehicular traffic: Distributions of distance headways and distance between jams. *Physica A*, 246(3-4):471–486, December 1997.

[15] D. Chowdhury, A. Pasupathy, and S. Sinha. Distributions of time- and distance-headways in the nagel-schreckenberg model of vehicular traffic: effects of hindrances. *Eur. Phys. J. B*, 5(3):781–786, October 1998.

[16] L. Roters, S. Lübeck, and K. D. Usadel. Critical behavior of a traffic flow model. *Phys. Rev. E*, 59(3):2672–2676, March 1999.

[17] D. Chowdhury, J. Kertész, K. Nagel, L. Santen, and A. Schadschneider. Comment on "critical behavior of a traffic flow model". *Phys. Rev. E*, 61(3):3270–3271, March 2000.

[18] L. Roters, S. Lubeck, and K. D. Usadel. Reply to "comment on 'critical behavior of a traffic flow model"'. *Phys. Rev. E*, 61(3):3272–3274, March 2000.

[19] B. S. Kerner, S. L. Klenov, and D. E. Wolf. Cellular automata approach to three-phase traffic theory. *J. Phys. A-Math. Gen.*, 35(47):9971–10013, November 2002.

[20] L. C. Q. Vilar and A. M. C. Souza. Cellular automata models for general traffic conditions on a line-. *Physica A*, 211:84–92, 1994.

[21] D. Jost and K. Nagel. Probabilistic traffic flow breakdown in stochastic car-following models. *Transport Res. Rec.*, 1852:152–158, January 2003.

[22] D. M. Miedema, A. S. de Wijn, and P. Schall. Criterion for condensation in kinetically constrained one-dimensional transport models. *Phys. Rev. E*, 89(6):062812, June 2014.

[23] A. M. C. Souza and L. C. Q. Vilar. Traffic-flow cellular automaton: Order parameter and its conjugated field. *Phys. Rev. E*, 80(2):021105, August 2009.

[24] W. Zhang, W. Zhang, and W. Chen. Phase transition behavior in a cellular automaton model with different initial configurations. e-print arXiv:1102.5704 [nlin.CG], February 2011.

[25] W. Zhang and W. Zhang. Energy dissipation in the nagel-schreckenberg model with open boundary condition. *Eur. Phys. J. B*, 87(1):4, January 2014.

[26] A. S. de Wijn, D. M. Miedema, B. Nienhuis, and P. Schall. Criticality in dynamic arrest: Correspondence between glasses and traffic. *Phys. Rev. Lett.*, 109(22):228001, November 2012.

[27] N. Lakouari, K. Jetto, H. Ez-Zahraouy, and A. Benyoussef. Velocity correlations in the nagel-schreckenberg model. *Int. J. Mod. Phys. C*, 25(02):1350089, February 2014.

[28] M. Gerwinski and J. Krug. Analytic approach to the critical density in cellular automata for traffic flow. *Phys. Rev. E*, 60:188, 1999.

[29] A. M. Ferrenberg and D. P. Landau. Critical behavior of the three-dimensional ising model: A high-resolution monte carlo study. *Phys. Rev. B*, 44(10):5081–5091, September 1991.

[30] M. E. Fisher. The theory of equilibrium critical phenomena. *Rep. Prog. Phys.*, 30(2):615–730, July 1967.

[31] M. N. Barber. Finite-size scaling. In *Phase Transitions and Critical Phenomena*. Academic Press, London, 1983.

[32] N. Bergeal, F. Schackert, M. Metcalfe, R. Vijay, V. E. Manucharyan, L. Frunzio, D. E. Prober, R. J. Schoelkopf, S. M. Girvin, and M. H. Devoret. Phase-preserving amplification near the quantum limit with a josephson ring modulator. *Nature*, 465:64–68, 2010.

[33] M. Hatridge, R. Vijay, D. H. Slichter, John Clarke, and I. Siddiqi. Dispersive magnetometry with a quantum limited squid parametric amplifier. *Phys. Rev. B*, 83:134501, Apr 2011.

[34] N. Bergeal, F. Schackert, L. Frunzio, and M. H. Devoret. Two-mode correlation of microwave quantum noise generated by parametric down-conversion. *Phys. Rev. Lett.*, 108:123902, 2012.

[35] Yang Yu, Shi-Liang Zhu, Guozhu Sun, Xueda Wen, Ning Dong, Jian Chen, Peiheng Wu, and Siyuan Han. Quantum jumps between macroscopic quantum states of a superconducting qubit coupled to a microscopic two-level system. *Phys. Rev. Lett.*, 101:157001, 2008.

[36] R. Vijay, D. H. Slichter, and I. Siddiqi. Observation of quantum jumps in a superconducting artificial atom. *Phys. Rev. Lett.*, 106:110502, 2011.

[37] R. Vijay, C. Macklin, D. H. Slichter, S. J. Weber, K. W. Murch, R. Naik, A. N. Korotkov, and I. Siddiqi. Stabilizing rabi oscillations in a superconducting qubit using quantum feedback. *Nature*, 490:77–80, 2012.

[38] Stefan Brakhane, Wolfgang Alt, Tobias Kampschulte, Miguel Martinez-Dorantes, René Reimann, Seokchan Yoon, Artur Widera, and Dieter Meschede. Bayesian feedback control of a two-atom spin-state in an atom-cavity system. *Phys. Rev. Lett.*, 109:173601, Oct 2012.

[39] G. G. Gillett, R. B. Dalton, B. P. Lanyon, M. P. Almeida, M. Barbieri, G. J. Pryde, J. L. O'Brien, K. J. Resch, S. D. Bartlett, and A. G. White. Experimental feedback control of quantum systems using weak measurements. *Phys. Rev. Lett.*, 104:080503, Feb 2010.

[40] Markus Koch, Christian Sames, Alexander Kubanek, Matthias Apel, Maximilian Balbach, Alexei Ourjoumtsev, Pepijn W.H. Pinkse, and Gerhard Rempe. Feedback cooling of a single neutral atom. *Phys. Rev. Lett.*, 105:173003, 2010.

[41] C. Sayrin, I. Dotsenko, X. Zhou, Bruno Peaudecerf, Sébastien Gleyzes Théo Rybarczyk, Pierre Rouchon, Mazyar Mirrahimi, Hadis Amini, Michel Brune, Jean-Michel Raimond, and Serge Haroche. Real-time quantum feedback prepares and stabilizes photon number states. *Nature*, 477:73–77, 2011.

[42] K. Jacobs. How to project qubits faster using quantum feedback. *Phys. Rev. A*, 67:030301(R), 2003.

[43] J. Combes and K. Jacobs. Rapid state-reduction of quantum systems using feedback control. *Phys. Rev. Lett.*, 96:010504, 2006.

[44] Elias J. Griffith, Charles D. Hill, Jason F. Ralph, Howard M. Wiseman, and Kurt Jacobs. Rapid state purification in a superconducting charge qubit. *Phys. Rev. B*, 75:014511, 2007.

[45] S. Ashhab and Franco Nori. Control-free control: Manipulating a quantum system using only a limited set of measurements. *Phys. Rev. A*, 82:062103, 2010.

[46] K. Jacobs. Feedback control using only quantum back-action. *New Journal of Physics*, 12(4):043005, April 2010.

[47] Joshua Combes, Howard M. Wiseman, Kurt Jacobs, and Anthony J. O'Connor. Rapid purification of quantum systems by measuring in a feedback-controlled unbiased basis. *Phys. Rev. A*, 82:022307, Aug 2010.

[48] Joshua Combes and Howard M. Wiseman. Maximum information gain in weak or continuous measurements of qudits: Complementarity is not enough. *Phys. Rev. X*, 1:011012, Sep 2011.

[49] A. Shabani and K. Jacobs. Locally optimal control of quantum systems with strong feedback. *Phys. Rev. Lett.*, 101:230403, 2008.

[50] Kurt Jacobs and Alireza Shabani. Quantum feedback control: how to use verification theorems and viscosity solutions to find optimal protocols. *Contemporary Physics*, 49(6):435–448, November 2008.

[51] S. Sridharan, M. Yanagisawa, and J. Combes. Optimal rotation control for a qubit subject to continuous measurement. *arXiv:1211.5617*, 2012.

[52] Todd A. Brun. A simple model of quantum trajectories. *American Journal of Physics*, 70(7):719, 2002.

[53] Kurt Jacobs and Daniel A. Steck. A straightforward introduction to continuous quantum measurement. *Contemporary Physics*, 47(5):279–303, September 2006.

[54] Heinz-Peter Breuer and Francesco Petruccione, editors. *The Theory of Open Quantum Systems*. Oxford University Press, Oxford, 2007.

[55] J. Nocedal and S. J. Wright. *Numerical Optimization*. Springer, New York, 2006.

Appendix: Permission Request

To: permissions@iop.org

Hi

This is Ashkan Balouchi and I am the first author on the article published in NJP on 30 September 2014, titled: "Optimal measurement-based feedback control for a single quit: a candidate protocol".
(link: http://iopscience.iop.org/article/10.1088/1367-2630/16/9/093059?fromSearchPage=true).
I wanted to use this article as a part of my PhD dissertation in Louisiana State University. Normally I am required to include a copyright release (or permission letter) from the publisher to do such. I am writing to ask if such a situation is applicable for NJP (as an open access journal) and if so, could you please provide me that.
I appreciate your time very much in advance.

All the bests,
Ashkan Balouchi
4/5/2016

To: abalou1@lsu.edu

Dear Ashkan Balouchi,

Thank you for your request to reproduce IOP Publishing material. The material you have requested was published under a CC BY licence (http://creativecommons.org/licenses/by/3.0/). Therefore you may reuse the content without permission, so long as you reference it adequately and adhere to the terms of the CC BY licence.

If you have any further questions or if there is any more we can do to help, please let me know.

Kind regards,

Kathryn Shaw

4/7/2016

Copyright & Permissions Team

Gemma Alaway - Rights & Permissions Adviser

Kathryn Shaw - Editorial Assistant

Contact Details

E-mail: permissions@iop.org

For further information: http://iopscience.iop.org/page/copyright

Please note: We do not provide signed permission forms as a separate attachment. Please print this email and provide it to your institution as proof of permission.

Vita

Ashkan Balouchi was born in Tehran, Iran, in 1984. He received his B.S. in Physics from Sharif University of Technology, Tehran, Iran in May 2007. He earned his M.S. in Physics from Sharif University of Technology, Tehran, Iran in May 2010. He started his graduate studies at Louisiana State University in June 2010. He expects to graduate in May 2016.